Hydrogen production by ethanol partial oxidation over nano-iron oxide catalysts produced by chemical vapour synthesis

Von der Fakultät für Ingenieurwissenschaften,
Abteilung Maschinenbau und Verfahrenstechnik der

Universität Duisburg –Essen

Zur Erlangung des akademischen Grades

eines

Doktors der Naturwissenschaften
Dr. rer. nat.

genehmigte Dissertation

von

Wael Ahmed Abou Taleb Sayed Ahmed

aus

Daqahlia, Ägypten

Gutachter: Uni.-Prof. Dr. rer. nat. Burak Atakan
Juniorprof. Dr. Anjana Devi
Tag der mündlichen Prüfung: 13.01.2011

Zusammenfassung

Diese Arbeit präsentiert die experimentellen Ergebnisse der Synthese von nicht unterstützten und unterstützten SiC-Eisenoxid-Nanopartikeln und deren katalytische Aktivität gegenüber der partiellen Oxidation von Ethanol. Zum Vergleich wurde eine nicht unterstützte Eisenoxidphase in Richtung der partiellen Oxidation von Ethanol getestet. Die γ-Fe_2O_3 und α/γ-Fe_2O_3-Phasen-Katalysatoren wurden mit Hilfe des CVS-Verfahrens mit $Fe(CO)_5$ als Vorstufe hergestellt und stammen von einem anderen Autor. Die α-Fe_2O_3 und SiC-Nanopartikel wurden nach dem CVS-Verfahren mit Hilfe eines Heißwandreaktors bei atmosphärischem Druck hergestellt. Ferrocene und Tetramethylsilan wurden als Vorstufe für die Herstellung verwendet. Prozessparameter der Vorläufer-Verdampfungstemperatur, Vorläufer-Konzentration, Gasgemisch-Geschwindigkeit und Gasgemisch-Verdünnung wurden analysiert und optimiert, um die kleinstmögliche Partikelgröße herstellen zu können. Für die Serienproduktion des Fe_2O_3/SiC-Katalysators wurde eine neue Heißwandreaktor-konstruktion für die Herstellung der Partikel verwendet. Die Partikel wurden durch gleichzeitige thermische Zersetzung von Ferrocene und Tetramethylsilan in einem Reaktor von beiden Seiten erzeugt. Produktionsparameter für den Abstand des Einlaufrohrs innerhalb des Reaktors, d.h. die Vorläufer-Verdampfungstemperatur und der Trägergasstrom, wurden untersucht, um eine Reihe von Proben mit verschiedenen Eisenoxidanteilen zu produzieren.

Die Zusammensetzung, die physikalischen und chemischen Eigenschaften der präparierten Katalysatoren wurden durch XRD, EDX, REM, BET-Oberfläche, FTIR, XPS und dynamische Lichtstreuung (DLS) charakterisiert.

Die katalytische Aktivität gegenüber der Gasphasenoxidation von Ethanol wurde in einem Temperaturbereich von 260 bis 290°C untersucht. Die Produkt-verteilung der einzelnen Katalysatoren wurde anhand der Massenspektrometrie analysiert. Die Aktivität von Fe_2O_3-Schüttgut und SiC-Nanopartikeln wurde mit präparierten Nano-Eisenoxidphasen-Katalysatoren verglichen. Die Reaktions-parameter, d.h. die Reaktionstemperatur und das O_2/Ethanol-Verhältnis, wurden optimiert. Eine Stabilität der Katalysatoren wurde für eine Reaktionszeit von 10 Stunden gemeldet. Die Ergebnisse zeigten, dass die Reaktionsstrecke, die Produkt-verteilung und die Wasserstoff-Selektivität stark von der Eisenoxid-Phase abhängen.

Die α-Fe_2O_3-Phase zeigte eine hohe Wasserstoff-Selektivität mit der höchsten Stabilität.

Bei den α-Fe_2O_3/SiC-Trägerkatalysatoren waren Acetaldehyd, Wasser und CO_2 die Hauptprodukte. Die Produktverteilung war stark vom Eisengehalt des Katalysators abhängig. Mit steigendem Eisengehalt der Probe wurde mehr CO_2 und Wasser hergestellt. Der Katalysator mit 1.9% Eisengehalt zeigte die höchste Acetaldehyd-Ausbeute. Das ist auf den geringen Eisenoxidgehalt an den aktive Stellen zurückzuführen, die zur Dehydrierung von Ethanol zu Acetaldehyd führen. Dagegen wurden bei höherem Eisengehalt mehr aktive Stellen gebildet und somit das Acetaldehyd readsorbiert und weiter zu CO_2 oxidiert. Alle Trägerkatalysatoren zeigten eine gute Stabilität für 10 Stunden. In dieser Zeit verringerte sich der Ethanolumsatz auf 9% bei konstanter Acetaldehyd-Ausbeute.

Diese Ergebnisse liefern Hinweise darauf, dass die Reaktion über die Eisenoxid-Oberfläche und Eisenoxid-Schnittstelle erfolgt und nicht über die SiC-Partikel. Diese Ergebnisse wurden durch die Ethanol-Oxidation in reinen α-Fe_2O_3 Nanopartikeln mit unterschiedlichen Flächen unterstützt. Diese Flächen wurden in Abhängigkeit von der gemessenen Fläche für reines α-Fe_2O_3 und der errechneten Fläche für Eisenoxid in den Trägerproben ausgewählt. Die Untersuchung ergab, dass bei einer großen Katalysator-Oberfläche Wasserstoff mit hoher Selektivität hergestellt werden kann, während bei kleiner Fläche nur Acetaldehyd, Wasser und CO_2 produziert werden können.

Die Charakterisierung der verwendeten Katalysatoren zeigte eine kleine Variation in der Eisenoxid-Partikelgröße und eine große Fläche. Dies bewies, dass der SiC-Träger eine Hot-Spot Bildung vermeidet und ein Sintern der Eisenoxid-Partikel verhindert.

Abstract

This work presents the experimental results of the synthesis of unsupported and supported SiC iron oxide nanoparticles and their catalytic activity towards ethanol partial oxidation. For comparison, further unsupported iron oxide phases were investigated towards the ethanol partial oxidation. These γ-Fe_2O_3 and α/γ-Fe_2O_3 phase catalysts were prepared by the CVS method using $Fe(CO)_5$ as precursor, supplied by another author. The α-Fe_2O_3 and SiC nanoparticles were prepared by the CVS method using a home made hot wall reactor technique at atmospheric pressure. Ferrocene and tetramethylsilane were used as precursor for the production process. Process parameters of precursor evaporation temperature, precursor concentration, gas mixture velocity and gas mixture dilution were investigated and optimised to produce particle sizes in a range of 10 nm. For Fe_2O_3/SiC catalyst series production, a new hot wall reactor setup was used. The particles were produced by simultaneous thermal decomposition of ferrocene and tetramethylsilane in one reactor from both sides. The production parameters of inlet tube distance inside the reactor, precursor evaporation temperature and carrier gas flow were investigated to produce a series of samples with different iron oxide content.

The prepared catalysts composition, physical and chemical properties were characterized by XRD, EDX, SEM, BET surface area, FTIR, XPS and dynamic light scattering (DLS) techniques.

The catalytic activity for the ethanol gas-phase oxidation was investigated in a temperature range from 260°C to 290°C. The product distributions obtained over all catalysts were analysed with mass spectrometry analysis tool. The activity of bulk Fe_2O_3 and SiC nanoparticles was compared with prepared nano-iron oxide phase catalysts. The reaction parameters, such as reaction temperature and O_2/ethanol ratio were investigated. The catalysts stability was reported for a reaction time of 10 hours. The results showed that the reaction route, the product distribution and hydrogen selectivity strongly depend on the iron oxide phase. The α-Fe_2O_3 phase showed high hydrogen selectivity with the highest stability.

Over α-Fe_2O_3/SiC supported catalysts acetaldehyde, water and CO_2 were the main products. The product distributions strongly depended on the catalyst iron content. With increasing sample iron content, more CO_2 and water was produced. The catalyst with an iron content of 1.9% showed the highest acetaldehyde yield.

This is attributed to the low iron oxide content at active sites which lead to a dehydrogenation of ethanol to acetaldehyde. In contrast, at higher iron content more active sites were provided hence the acetaldehyde re-adsorbed and further oxidised to CO_2. All supported catalysts showed a good stability for 10 hours. In this time, the ethanol conversion was decreased by 9% with constant acetaldehyde yield.

These results provide evidence that the reaction occurs over the iron oxide surface and iron oxide-support interface but not over the SiC particles. These results were supported by carrying out the ethanol oxidation over pure α-Fe_2O_3 nanoparticles with different surface areas. Those surface areas were chosen depending on the surface areas measured for the pure α-Fe_2O_3 and surface area calculated for iron oxide in the supported samples. The investigation showed that with a large catalyst surface areas hydrogen with a high selectivity may be produced, whereas with a small surface area only acetaldehyde, water and CO_2 can be produced.

The characterisation of the used catalyst showed a small variation of the iron oxide particle size and large surface area. This proved that the SiC support avoids a hot spot formation and prevents iron oxide particles from being sintered.

Dedications

To my father’s soul, my mother and my wife

Acknowledgement

I am pleased to say how deep my heartfelt gratitude, respect and thanks toward my supervisor Prof. Dr. rer. nat. habil. Burak Atakan for giving me an opportunity to work in his group, for his interest, following up the work progress, truly helpful guidance, valuable suggestions, encouragement and continuous help.

I would also like to thank Dr. rer. nat. Ulf Bergmann for his cooperation and his kind support.

Deep thanks are due to Priv.-Doz. Dr. rer. nat. habil. Christian Pflitsch for his help during the course of nanoparticles preparation. Special thanks are to Dr. Ralf Theissmann for TEM measurement.

I would also like to extend my thanks for the technical support to Mr. Dipl.-Ing. Andreas Görnt and Mr. Manfred Richter

Special thanks to Mr. Smail Boukercha for SEM measurements, Mrs. Ursula Giebel for EDX measurements, Mrs. Beate Endres for BET measurements, Ms. Anna Warland for XPS measurements and Mr. Alexei Poukhovoi for FTIR measure-ements.

Thanks also to all my colleagues in the thermodynamic department for their sincere help and continuous encouragement.

I would also like to express my appreciation and thanks to the outside mission sector at the Egyptian Ministry of Higher Education for my scholarship and the financial support.

CONTENTS

Contents

LIST OF FIGURES

List of figures

LIST OF TABLES

List of tables

CHAPTER 1
INTRODUCTION

1. Introduction

Considering the ecological future of the earth is first and foremost the deciding factor when choosing the kind of energy carrier mainly being used by mankind. The main energy carriers used today are the fossil carbon fuels. However, dependence on fossil fuels has led to a serious energy crisis. Also the community face a big problem due to limitation in the fossil fuels availability. Moreover, combustion of fossil fuels produces substantial greenhouse emissions and acid rain. In response, a clean form of energy is required to meet the world's demand for energy needed to support the global economic growth while reducing impacts on air quality and the potential effects of greenhouse emissions. Fuel cells are an attractive alternative to conventional power generators and direct engines which use fossil fuels [1]. Fuel cells use pure H_2 or H_2-rich gas [2, 3] which must contain < 20 ppm carbon monoxide, because carbon monoxide poisons the anodic Pt electrode in fuel cells [4]**.** The main problems, faced when using hydrogen as a fuel, are related to storage, safety and refuelling. Furthermore, there are several technological barriers, such as a lack of an adequate infrastructure for both the production and delivery of hydrogen [5], that have to be overcome. One solution to this difficulty is the on-board hydrogen generation from a suitable renewable high-energy fuel[6].

1.1. Hydrogen production resources

Methane steam reforming offers a good process to produce hydrogen because of the already existing infrastructure, high hydrogen content and since no C-C bond is present which requires high energy to be broken, all of that reasons makes the process highly economic. However, the use of fossil fuels fails to provide solutions to remove the huge amounts of CO_2 co-produced. Additionally, it doesn't overcome the non-sustainable nature of current energy systems. In this context, production of hydrogen from renewable liquid sources with existing infrastructure as an effective solution has become an urgent need.

Among the fuels, methanol is considered to be a potential resource [7] due to its high hydrogen-to-carbon ratio which led to high hydrogen production yield and a minimised danger for coke formation deactivating the catalyst used. However, in the event of spills or leaks, methanol causes environmental problems due to its toxicity and highly flammability, Pt anodic catalyst is easy to be poisoned by CO intermediate

from methanol oxidation. Especially, methanol has a high permeability through membranes, causing loss of fuel and a drop in the fuel cell performance [8, 9]

Hydrogen production from biomass or biomass derived oxygenates through steam reforming has attracted great interest since the produced CO_2 is consumed for biomass growth and thus offering a carbon dioxide neutral energy supply[10]. Among those oxygenates, ethanol is of particular interest due to its low toxicity, relatively high hydrogen content, availability and ease of handling and low permeability through polymeric membranes [11]. Moreover, in countries like Brazil, the ethanol production and distribution infrastructure is already established [12].

1.2. Hydrogen production processes from ethanol

Hydrogen may be produced directly from ethanol by different processes such as steam reforming (SR) [13-17]**,** partial oxidation (POE) [18, 19] or oxidative steam reforming (OSR) [20-23]**.** Steam reforming converts ethanol according to the stoichiometric reaction:

$$CH_3CH_2OH + 3H_2O \longrightarrow 6H_2 + 2CO_2 \qquad \Delta H^{o}_{298} = +347 \text{ kJ mol.}^{-1}$$

However, SR is a highly endothermic reaction operated typically at high temperatures, 873–1073 K which is a serious drawback that increases the process costs [24-27].

The oxidative steam reforming process is a combination of steam reforming and partial oxidation (POE).

$$C_2H_5OH + 1.8H_2O + 0.6O_2 \longrightarrow 4.8\ H_2 + 2CO_2 \qquad \Delta H^{o}_{298} = +4.4 \text{ kJ mol.}^{-1}$$

This reaction ratio provides a nearly thermally neutral process with hydrogen concentration of 70 % in the outlet stream [28].

1.2.1. Ethanol partial oxidation (POE)

Ethanol partial oxidation has the advantage of easy handling and low cost. Ethanol partial oxidation is an exothermic reaction which doesn't need extra heating that leads to a fast start-up and response times. Moreover, the POE reactor is more compact than the steam reformer [29] because of the expected higher reaction rates.

$$C_2H_5OH + 1.5\ O_2 \longrightarrow 3\ H_2 + 2\ CO_2 \qquad \Delta H^{\circ}_{298} = -557 \text{ kJ / mol}^{-1}$$

The O_2/ethanol ratio of 1.5 is found to be the most effective for ethanol partial oxidation since it is useful to produce a carbon monoxide free hydrogen rich gas.

Normally partial oxidation reaction is coupled through the water–gas shift (WGS) reaction that helps to generate more hydrogen.

$$CO + H_2O \longrightarrow CO_2 + H_2 \qquad \Delta H^{o}_{298} = -41 \text{ kJ mol}^{-1}$$

1.2.1.1. Mechanism of ethanol partial oxidation

The efficiency of C—C bond cleavage is the key to make ethanol oxidation useful in fuel cell applications. For partial oxidation, products such as acetaldehyde and acetic acid have been observed [30, 31]. Several authors reported that mechanism of ethanol oxidation can be summarised in the scheme described in Figure (1) [32-34]. The fragmentation of ethanol to stable adsorbates has been the subject of many previous studies using both in situ fourier transform infrared spectroscopy (FTIR) and electrochemical mass spectrometry (DEMS) [35-37]. The adsorbates have been identified to be $OCH_2CH_3^*$, $COHCH_3^*$, $COCH_3$ [38] besides CO.

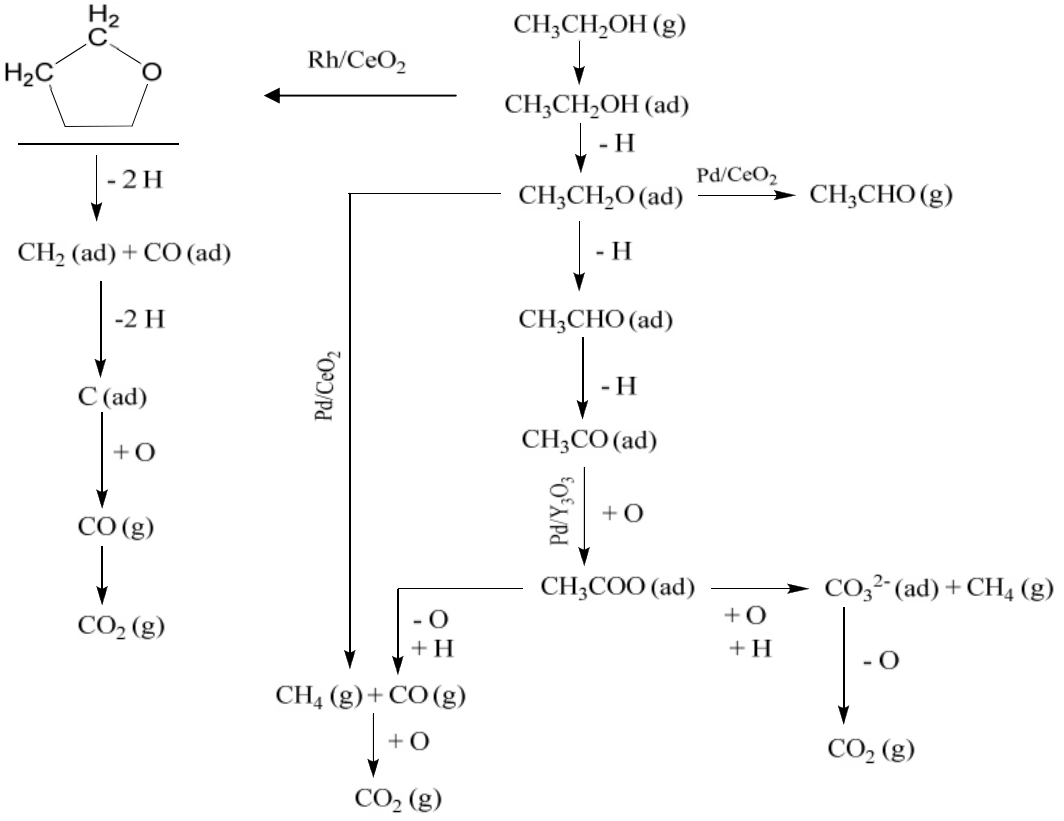

Figure 1: Reaction pathway proposed for partial oxidation of ethanol over Pd/CeO_2 and Pd/Y_2O_3 catalysts [39]

Sheng *et al.*[38] observed the formation of the five-member-ring oxametall-acycle intermediate over Rh/CeO_2 and $Rh–Pt/CeO_2$ catalysts that were formed by losing one hydrogen from the terminal methyl group in ethoxy species. Interestingly,

only CO_2 was detected as product in the oxidation of ethanol adsorbates [34]. This suggests that CO_2 is formed from strongly adsorbed intermediates on the electrode, while the products of acetaldehyde and acetic acid are formed from weakly adsorbed intermediates. The concentration of ethanol strongly influences the product distribution. Low ethanol concentrations favour the production of acetic acid and CO_2, while concentrated ethanol solutions favour acetaldehyde formation. It has been argued that the low yield of acetic acid and CO_2 for high ethanol concentrations is probably due to the limited availability of free sites for adsorbing water, which is an oxygen providing species in the oxidation process via a Langmuir–Hinshelwood mechanism. The partial oxidation of ethanol over different catalytic systems has been studied for the evaluation of its redox catalytic activity. Although a high yield of hydrogen can be achieved using noble metal based catalysts such as Pt/CeO_2, the high cost of noble metals limits its practical applications [40, 41]**.** However, using an active and cheap catalyst at relatively low temperatures is more attractive from the practical point of view. Recently, iron and iron oxide have become of high interest because it is a cheap and environmental material which could be used in alcohol oxidation [42, 43]. Most of the studies use the chemical methods for catalyst preparation, in this work a modified chemical vapour deposition (CVD) process is used to produce iron oxide and supported iron oxide nanoparticle to be tested in ethanol partial oxidation.

1.3. Chemical vapour deposition

Chemical vapour deposition may be defined as the deposition of a solid on a heated surface or preheated gas mixture over a cold substrate from a chemical reaction in the vapour phase. With CVD many atoms, molecules or a combination of those can be produced. Those may be used in a variety of applications such as semiconductors, many optical applications as, for example, the manufacture of blue light emitting diodes (LED) and also in corrosion applications. The CVD process consists of the following sequence of steps:

1- Reactant gases enter the reactor by forced flow.
2- Gases diffuse through the boundary layer.
3- Gases come into contact with the substrate's surface.
4- Deposition reactions take place on the substrate surface.
5- Gaseous by-products of the reaction diffuse away from the surface through the boundary layer.

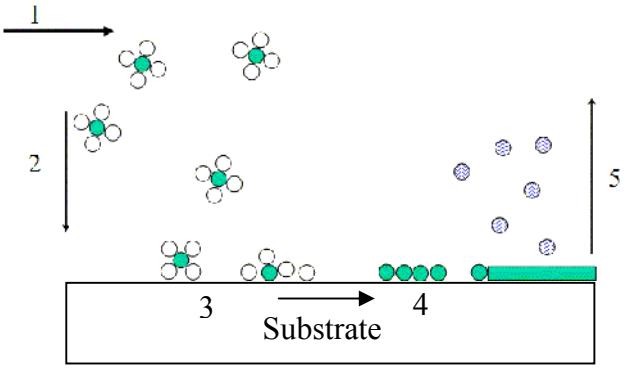

Figure 2: Schematic diagram representing the sequence of CVD steps

CVD has several important advantages such as, it is not restricted to a line-of-sight deposition allowing that even difficult three-dimensional configurations can be coated relatively easy, and it has a high deposition rate. Finally, CVD equipment does normally not require ultrahigh vacuum which is needed for other processes as, for example, the PVD method for example. CVD is generally adapted to many process variations which make it the preferred process in many applications. A disadvantage of CVD is the need of high temperature especially for sintering cases. However, the development of metallo-organic CVD partially offsets this problem.

Several versions of chemical vapour deposition processes are widely used, e.g. metallo-organic chemical vapour deposition (MOCVD), low pressure chemical vapour deposition (LPCVD), plasma enhanced chemical vapour deposition (PECVD), atomic layer chemical vapour deposition (ALCVD), ultra-high vacuum chemical vapour deposition (UVCVD), laser chemical vapour deposition (LCVD), and many others [44, 45]. Several chemical reactions can occur singly or simultaneously during the CVD process such as thermal decomposition (pyrolysis), reduction, hydrolysis, disproportionation, oxidation, carburisation, and nitridation.

The CVD reaction may also occur in the gas phase and not only at the substrate surface if the supersaturation of the reactive gases and the temperature are sufficiently high. So, gas-phase precipitation is used purposely, to produce extremely fine powders and particles. This process of producing particles inside the furnace is called chemical vapour synthesis (CVS).

Among the CVD versions, metallo-organic CVD (MOCVD) is a specialised area of CVD due to its use at lower temperature than thermal CVD since it is used in ranges of (573–1073 K) and at pressures varying from less than 1 Torr to atmospheric. Moreover, epitaxial growth could be successfully achieved. Furthermore, the equipment and chemicals used in MOCVD are often commercially available [44].

In such a process organo-metallic compounds, those composed of element atom bound to one or more carbon atoms of an organic hydrocarbon group, are used as starting materials (precursor). Precursors should be stable at room temperature and able to decompose readily at low temperature, i.e., below 773 K. Among organo-metallic compounds metal-acetylacetonates, also known as metal-pentanedionates are the most used precursor because it is stable in air, readily soluble in organic solvents and commercially available. Deposition of metal oxide by CVD becomes interesting and has yet to be investigated due to its wide applications [44].

Iron oxide is one of the most important materials that can be produced by using a CVD process starting with the iron acetylacetonate or ferrocene(with$(C_5H_5)_2Fe$ chemical formula), in O_2 at 573–773 K and 1–20 Torr [46]**.** Iron oxide has many applications due to its magnetism and catalytic activity for many reactions especially for oxidation [47].

Silicon carbide is an advanced material [48] with a wide spectrum of applications in high-performance functional or structural ceramic materials. Silicon carbide is therefore used as a hard and wear-resistant material, as a high-temperature material in heating elements, turbines, combustion chambers[44], and rocket nozzles and in electronics [49] for high-temperature, high power semi-conductors. [50] Silicon carbide is a covalent carbide which exists in many phases whereas the β-SiC phase is the one of major interest. β-SiC exhibits a high thermal conductivity, a high resistance towards oxidation, a high mechanical strength, a low specific weight, and chemical inertness, all of which making it a good candidate to be used as a catalyst support material instead of the traditional insulator supports.

β-SiC is mostly synthesised by gas phase reactions of compounds containing silicon and carbon or silica [51-53] The advantage of the reactions in the gas phase is that the production of powders with narrow particle size distribution at small mean values and high purity. Tetramethylsilane is a well-known precursor for the production of SiC films by CVD either in low-pressure [52-54] or plasma-assisted processes. Although the silicon carbide prepared at low temperature CVD is contaminated with carbon and silica, it is also considered as advantage in catalysis since it is well known that silica has a good catalytic activity to the oxidation reaction.

1.4. Scope of the present work

The objective of the present work is to compare the catalytic activity of bulk Fe_2O_3, unsupported, α,γ-Fe_2O_3, γ-Fe_2O_3 (provided by another author), α-Fe_2O_3 and series of Fe_2O_3/SiC with different iron oxide loading prepared by the CVS technique for hydrogen production via ethanol partial oxidation (POE). To learn about the interrelationship between the characteristics of the catalyst and catalyst performance in POE, the catalyst is characterised by X-ray diffraction (XRD), scanning electron microscopy (SEM) and energy dispersive X-ray spectroscopy (EDX) analysis. In order to develop an efficient catalytic system, attention has been paid to optimise the reaction parameters such as reaction temperature, O_2/C_2H_5OH ratio and the catalyst surface area on the performance of catalysts for hydrogen production. Catalyst stability was studied by carrying out the experiment for 10 hours and then follows how far the carried experiment affects the catalysts activity and selectivity towards hydrogen and by-products. The catalyst is then characterised using the previously mentioned tools to understand how the POE process affects the chemical and physical properties of the catalysts.

1.4.1. Thesis outline

The next chapter provides information about the theoretical background of the present thesis such as catalysis, mass spectrometry, reaction kinetics and adsorption phenomena. Chapter 3 includes detailed information about the previous work for catalysts used in ethanol partial oxidation. Chapter 4 describes the experimental set up used to produce the catalysts and to test its catalytic activity. The methods needed to characterise catalysts and equations for the calculation of catalysts activities and selectivity towards ethanol partial oxidation under the investigated conditions are also included. Chapter 5 discuss the results for the production of catalysts by means of the CVS process and the effect of different preparation condition on the prepared particles size. Catalysts characterisations, catalytic activity and catalysts deactivation results will be discussed in chapter 6. Finally, the main finding and optimum condition for ethanol partial oxidation will be shown in detail in conclusion.

CHAPTER 2
THEORETICAL BACKGROUND

2. Theoretical background

2.1. Catalysis definitions

Catalysis is an important key to chemical transformations. Most industrial synthesis and nearly all biological reactions need catalysts. Nowadays, catalysis is more and more introduced to the suppression of atmospheric pollution and to design new technologies to transform energy either by solar cells or through chemical conversion of hydrocarbons and alcohols to hydrogen for fuel cells. The term catalysis was first suggested by Berzelius [55] in 1935 as an explanation for his finding that some reactions become faster in presence of a very small quantity of foreign materials which was not at all related to the reactants. So the catalysis term can be defined as the process of accelerating the chemical reaction rate under the influence of foreign material. This material is normally called catalyst. The catalyst, in turn, is defined as a substance that increases the rate at which the chemical reaction reaches equilibrium without undergoing a chemical change itself. So, catalysis deals with changes on the route to equilibrium. It is about reaction kinetics, not thermodynamics that catalysts do not and cannot change the thermodynamic equilibrium. The catalyst speeds up the reaction rate through a sequence of by-paths with lower energetic transition states shown in Figure 3 [56].

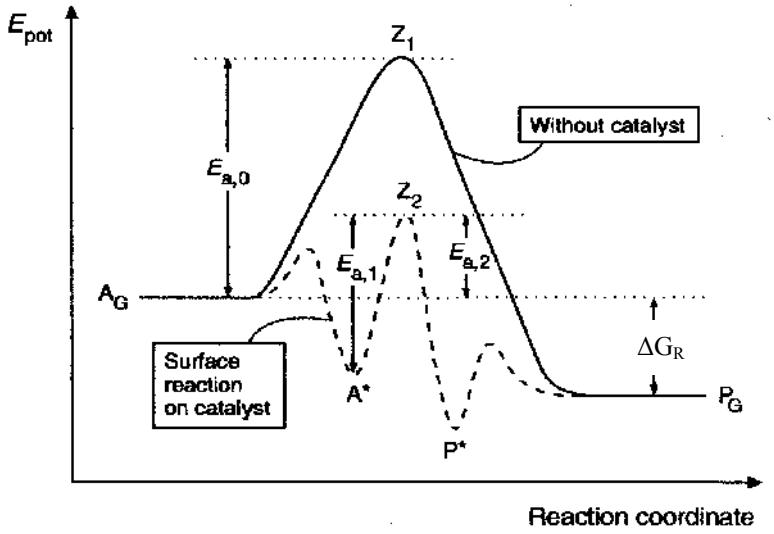

Figure 3: Course of a heterogeneously catalysed gas-phase reaction

Where $E_{a,o}$ uncatalysed reaction activation energy, $E_{a,1}$ true activation energy, $E_{a,2}$ apparent activation energy for catalysed reaction, Z_1 transition state of the gas phase reaction, Z_2 transition state of the surface reaction and ΔG_R the reaction enthalpy

Although it was formerly assumed that the catalyst remained unchanged during the reaction, it is now known that the catalyst is involved in chemical bonding with the reactants during the catalytic process. Thus catalysis is a cyclic process while the reactants are bound to one form of the catalyst, and the products are released from another one regenerating the initial state. The real catalyst, owing to competing reactions over its surface, may undergo chemical or physical changes during the catalytic process occurred over its surface such as a phase change, or metal oxide may oxidised to another oxidation state which may lower the catalyst activity (catalyst deactivation). Thus catalysts must be regenerated or eventually be replaced.

The catalyst and reactants may be present in the same phase or in different phases. Most industrial catalysts are liquids or solids, whereby the latter react only via their surface. Therefore catalysis is classified into homogeneous and heterogeneous processes [57]. In the first type the catalyst and the reactants have the same phase either gaseous or liquid. A typical example for homogeneous catalysis is the acetic acid esterification with ethanol in presence of sulphuric acid, while in the second type the catalyst and reactants are present in different phases. Normally in heterogeneous catalysis the catalyst is in the solid phase while the reactants are present in the liquid or the gas phase. In fact, the solid/gas combination is so common that some books and journals refer to it as classic heterogeneous catalysis or even simply as catalysis [58].

2.2. Heterogeneous catalysis steps

In a typical heterogeneous catalytic reaction in the gas phase, normally the following steps takes place [56]:

1- Diffusion of reactants from the boundary layer to the catalyst surface or into pores (in case of porous catalysts like zeolites)
2- Adsorption of reactants on the catalyst surface
3- Chemical reaction on the catalyst surface
4- Desorption of the products from the catalysts surface
5- Diffusion of the products from the surface
6- Diffusion of the products through the boundary layer or into the gas phase

In the heterogeneous catalysis, the adsorption of the reactants and products on the catalyst surface is of central importance. The adsorption may be due to physical adsorption (physisorption) or chemical adsorption (chemisorption) [59]. In physio-sorption, the reactants adsorb as a result of van der Waals forces, and the

accompanying heat of adsorption is comparable in magnitude to the heat of evaporation of the adsorbate. In chemisorption, chemical bonds are formed between the catalyst and the starting material [56]. The resulting surface molecules are often much more reactive than the free adsorbate molecules, and the heats of adsorption are comparable in magnitude to the heat of chemical reactions. Both types of adsorption are exothermic; raising the temperature generally decreases the equilibrium quantity of adsorbate. Physisorption is fast, and the equilibrium coverage is rapidly reached even at low temperature.

2.3. Adsorption isotherms

The chemisorption process generally requires high activation energies. It generally leads only to a monolayer, whereas in physisorption multilayers can be formed. In the adsorption process the free and adsorbed gases are in dynamic equilibrium. The dependence of the surface fractional coverage on the pressure at a specific temperature is called the adsorption isotherm. In the following the fundamental laws of adsorption shall be considered that provide the basis for the rate expressions of heterogeneously catalysed reactions.

Adsorption equilibria were early described empirically by Freundlich's equation describing general practical cases of adsorption.

$$C_A = ap_A^n \qquad (1)$$

Where C_A is the adsorbed gas concentration, p_A is the adsorbed gas partial pressure under equilibrium conditions, (a) is an empirical constant and (n) is a fraction between 0 and 1. Later on, it was found experimentally that the amount of gas adsorbed by solid increases with increasing total pressure; P. Langmuir expressed the concentration of the adsorbed gas as a function of the partial pressure and made his isotherm.

2.3.1. Langmuir isotherm

P. Langmuir assumed the following to formulate his isotherm and to simplify the adsorption process:

1- The catalyst surface is energetically homogeneous, so that the adsorption enthalpy is independent on the degree of surface coverage (θ_A).
2- The ability of a particle to bind is independent on whether or not the adjacent site is occupied.

For the dynamic equilibrium between the reactant gas (A) and the catalyst surface (M)

$$A(g) + M(\text{surfaca}) \longrightarrow AM$$

The rate of surface coverage change due to adsorption process will be

$$d\theta/dt = k_a pN(1-\theta) \qquad (2)$$

Where N is the total number of sites and N(1-θ) is the number of vacant sites, k_a is the rate constant and p is the reactant pressure. On the other hand the change in fractional surface coverage due to desorption will be

$$d\theta/dt = k_d N\theta \qquad (3)$$

where k_d is the desorption rate constant and Nθ is the number of covered sites. At equilibrium the two rates are equal and solving for θ give the Langmuir isotherm.

$$\theta = \frac{Kp}{(1+Kp)} \quad \text{where} \quad K = k_a/k_d \qquad (4)$$

In the case of the reactants are not only adsorbed but also dissociating, the adsorption rate will be proportional to the reactant pressure and the probability of both dissociated atoms to find sites those two factors expressed by $p\{N(1-\theta)\}^2$. The rate of desorption is proportional to the frequency of encounters of atoms on the surface which is expressed by $\{N\theta\}^2$, at equilibrium

$$\theta = (Kp)^{1/2}/\{1+(Kp)^{1/2}\} \qquad (5)$$

According to Langmuir's assumptions, the surface coverage increases with increasing the reactant pressure and only reaches unity at high pressure at which the reactant molecules formed monolayer over the surface and all sites will be occupied. The rate constant will change with temperature so that the rate dependence on temperature can be used to determine the enthalpy of adsorption at fixed surface coverage as

$$(\partial \ln K/\partial T)_\theta = \Delta_{ad}H/RT^2 \qquad (6)$$

2.3.2. Brunauer, Emmet and Teller isotherm

The theory behind the Langmuir isotherm has the disadvantage that it ignores the possibility of further adsorbing molecules over the initially adsorbed layer. If this happens, the isotherm will not become constant at a specific saturated value at high pressure but it will continuously rise. Brunauer, Emmet and Teller introduced the BET isotherm which takes into account the multilayer adsorption process [60]. They

assumed that the catalyst surface may be covered with several layers. The rate constant for adsorption and desorption of each layer will be k_a, k_d, $k_a^{\backslash}$, $k_b^{\backslash}$ …….etc., and the number of sites corresponding to zero, mono, bi and n-layer coverage will be N_o, N_1 and N_n respectively or N_i in general.

At equilibrium and for any layer the rate of adsorption and desorption will be:

$$k_a^{\backslash} N_{i-1} = k_d^{\backslash} N_i \qquad \text{where } i = 2,3,\ldots.. \tag{7}$$

This may be expressed in term of N_o as follows:

$$\begin{aligned} N_i &= (k_a^{\backslash}/k_d^{\backslash}) p N_{i-1} = (k_a^{\backslash}/k_d^{\backslash})^2 p^2 N_{i-2} = ... \\ &= (k_a^{\backslash}/k_d^{\backslash})_{i-1} (k_a/k_d) p^i N_o \end{aligned} \tag{8}$$

Now write $k_a^{\backslash}/k_d^{\backslash} = x$ and $k_a/k_d = cx$ so,

$$N_i = c(xp)^i N_o \tag{9}$$

Now calculate the total volume V of the adsorbed materials where V is proportional to the number of adsorbed materials and so,

$$V \alpha N_1 + 2N_2 + 3N_3 + ... = \sum_{i=1}^{\infty} iN_i \tag{10}$$

If there were complete monolayer coverage the volume adsorbed would be V_{mon}

$$V_{mon} \alpha N_o + N_1 + N_2 + ... = \sum_{i=1}^{\infty} N_i \tag{11}$$

Because each site in the actual sample then contributes one particle to the total volume, one obtains from equations 9, 10 and 11

$$V/V_{mon} = \{\sum_{i=1}^{\infty} iN_i\} \Big/ \{\sum_{i=1}^{\infty} N_i\} = cN_o\{\sum_{i=1}^{\infty} i(xp)^i\}/N_o + cN_o \sum_{i=1}^{\infty} (xp)^i\} \tag{12}$$

$$V/V_{mon} = pcx/(1-xp)(1-xp+cxp) \tag{13}$$

The final step is to equate 1/x to the vapour pressure P* of the bulk liquid adsorbed. If all surface sites N are deeply and uniformly buried so at equilibrium the pressure will be P*, and x in equation (12) will be 1/ P*. If this value introduced to equation (13), then the BET isotherm will be obtained and the equation will be as follows:

$$V/V_{mon} = cz/(1-z)\{1-(1-c)z\} \quad \text{where } Z = p/p^* \tag{14}$$

This usually rearranged to

$$z/(1-z)V = 1/cV_{mon} + (c-1)z/cV_{mon} \tag{15}$$

If $z/(1-z)V$ is drew against z, it results in a straight line with a slope equal to $(c-1)z/cV_{mon}$; the intercept will equal cV_{mon} so that c and V_{mon} could be obtained. This isotherm is later used to calculate the surface area the catalysts.

2.4. Mechanisms of heterogeneously catalyzed gas-phase reactions

In literature, up to a hundred different mechanisms and their rate equations are described. Knowledge of the mechanism of a heterogeneously catalysed reaction is a prerequisite for obtaining functional relationships between the reaction rate and the variables on which it depends. There are two famous mechanisms which are often discussed for such reactions. Normally, bimolecular gas-phase reactions occur in heterogeneous catalysis.

2.4.1. Langmuir–Hinshelwood mechanism

The early studies of heterogeneous catalysis mechanism were performed by Langmuir and Hinshelwood. To develop their calculations, they assumed the following [56] :

1- Both reaction partners are adsorbed without dissociation at different free sites on the catalyst surface.
2- The neighbouring chemisorbed molecules react over the catalyst surface to give the product without leaving the surface.
3- The product is then desorbed and diffused through the boundary layer.

The reaction sequence is thus:

$$A(g) \rightleftharpoons A^* \quad , B(G) \rightleftharpoons B^* \quad \text{And} \quad A^* + B^* \rightleftharpoons C^*$$

then $C^* \rightleftharpoons C(g)$ * adsorbed molecules

Assuming that the surface reaction between the two adsorbed molecules step is the rate determining step and on the basis of the relationship for mixed adsorption, the following rate equation can be formulated:

$$r = \frac{dp_c}{dt} = k\theta_A\theta_B = \frac{kK_Ap_AK_Bp_B}{(1+K_Ap_A+K_Bp_B)^2} \qquad (16)$$

This equation can be written in other forms depending on the degree of reactants adsorption as:

1- If the reactants are both weakly adsorbed, then K_A and K_B « 1 and the rate equation become: $r = k' p_A p_B$, where $k' = kK_A K_B$. In this case the reactions are in the first order in both reactants and in the second order overall.

2- If A is weakly and B is strongly adsorbed, K_A « 1 « K_B and the rate equation becomes $r = k'' \frac{p_A}{p_B}$, where $k'' = k \frac{K_A}{K_B}$

The reaction rate can be considered as a function of the partial pressure by assuming that the partial pressure p_A of the one component A has changed while the partial pressure of the other component is constant p_B.

1- At low partial pressure of component A, the degree of coverage θ_A is low, and all chemisorbed molecules can react with component B. In such a case when the term $K_A p_A$ becomes negligible, the rate equation becomes:

$$r \approx kK_A p_A \frac{K_B p_B}{(1+K_B p_B)} \approx k' p_A \qquad (17)$$

2- The reaction rate increases to a maximum where the surface is covered to an equal extent with A and B (i. e. $\theta_A = \theta_B$).

3- With increasing partial pressure of component A, the surface becomes increasingly occupied by A, and the probability of reaction with chemisorbed B decreases. Thus it could be said that the surface is blocked by A. Moreover, the term $(1+K_B p_B)$ in equation 16 becomes negligible compared to $K_A p_A$, and the rate of reaction can be calculated from:

$$r \approx K'' \frac{1}{K_A p_A} \approx \frac{1}{p_A} \qquad (18)$$

2.4.2. Eley–Rideal mechanism

This mechanism describes the chemisorption of only one reactant (A) on the catalyst surface. Then it reacts in this activated state with starting material B from the gas phase to give the chemisorbed product C. Finally, the product is desorbed from the catalyst surface. The reaction sequence is thus:

$$A(g) \rightleftharpoons A^* \quad \text{then} \quad A^* + B(g) \rightleftharpoons C^* \quad \text{finally} \quad C^* \rightleftharpoons C(g)$$

In this case only the degree of coverage of gas A is decisive for the reaction kinetics; on the basis of the Langmuir isotherm (Eq. 5-7), the following rate equation can be formulated:

$$r = k\theta_A p_B = k\frac{K_A p_A}{1+K_A p_A} p_B \qquad (19)$$

If the reaction rate was observed as a function of the partial pressure of component A at a constant p_B, it is seen that it follows the isotherm for p_A and eventually reaches a constant final value.

2.5. Catalysis for hydrogen production

The applied catalysis term includes the application of catalyst in many industrial applications such as oxidation, hydrogenation and C-C linkage processes. Some of these reflect the great attention paid to the protection of natural environment and new fuel production. One of the most important and interesting environmental issues are the greenhouse gas emissions and atmospheric pollution reduction [59]. Most of those gases came from the combustion of fossil fuels. Recently, the growing awareness of the society for those issues increased the demand to develop new and cleaner energy. The fuel cell is a good alternative to the conventional energy processes using fossil fuels. The fuel cell uses hydrogen as a fuel. Hydrogen is characterised by a high reactivity so that it cannot be found commonly in its pure form but rather in water or some organic materials. Pure hydrogen is one of the strongest chemical fuels in combustion processes, i.e. since methane has a high heating value of 55.5 [61], hydrogen has a 2.6 times larger heating value than methane [58]. Hydrogen is also a clean fuel since it produces only water by combustion. Another advantage of hydrogen is that it can be produced from a wide variety of renewable (like water and biomass) or fossil (coal, oil and natural gas) energy sources. Bioethanol produced by the fermentation of biomass is considered as an attractive feedstock for the sustainable production of hydrogen [2, 3, 13]. Steam reforming (SR), partial oxidation (POE) and oxidative steam reforming (OSR) are effective ways for producing hydrogen from bioethanol. Designing a suitable catalyst for the POE process is one of the technical barriers to overcome for the enhancement of process economics [62]. Several researchers [16, 29, 30] claimed that nanoscale Pt/CeO_2 is one of the best catalysts used for ethanol partial oxidation but the high cost of noble metal limits its practical

applications. Instead, it is more practical to achieve a cheap and effective catalyst for more economic benefits.

2.6. Structure and phases of iron oxide catalysts

Iron oxides are cheap materials used as catalysts for many catalytic industrial processes such as ammonia synthesis, water shift reaction for hydrogen production [63], the Fischer-Tropsch reaction and the oxidation of alcohols [64]. The common iron oxides used in catalysis for industrial processes are hematite (α-Fe_2O_3) and magnetite (Fe_3O_4). Due to their semi-conducting properties, they are both suitable for oxidation/reduction reactions. The electronic structure of the transition metals with the aid of the d-band is strongly affected in its catalytic properties by the occupational density of the electrons in this band. This is shown by the general trend of the rate of adsorption along the transition metal rows. The essential characteristic for semiconductors is the separation between the valance band of orbitals; the conduction band is less than 5 eV. Hematite is an n-type semiconductor. The conduction band is composed of empty Fe^{3+} d-orbital; the valance band consists of full $2t_{2g}$ Fe 3d ligand field orbital with some admixture from the oxygen anti-bonding 2p orbital as shown in Figure 4. Hence the conductivity is due to the involved electrons.

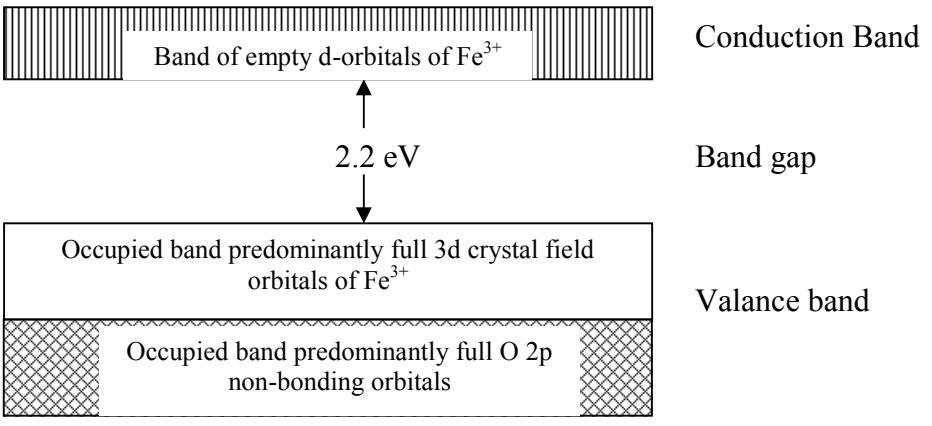

Figure 4: Band structure of hematite [65]

To promote the electrons movement across the band gap, energy greater than that of band gap is needed. If the band gap is small, the energy needed can be provided thermally. This is the case for hematite since its band gap is 2.2 eV [66].

Hematite and magnetite may also be used as acid/base catalysts owing to their amphoteric properties [66]. Those oxides can be used as finely dispersed powders or

as porous solids with a high surface area to volume ratio. Hematite is the oldest known iron oxide mineral. It is an extremely stable alpha phase [66] iron oxide and is often the end member produced during other iron oxide phase's transformation. Haematite is an isostructure with corundum. It lies in a hexagonal unit cell. The structure of haematite can be described as an array of oxygen ions stacked along the [001] anions. The Fe^{III} ions filled the two thirds of the sites which are arranged regularly with two filled sites followed by a vacant one in the same plane so that it forms a sixfold ring as shown in Figure 5.

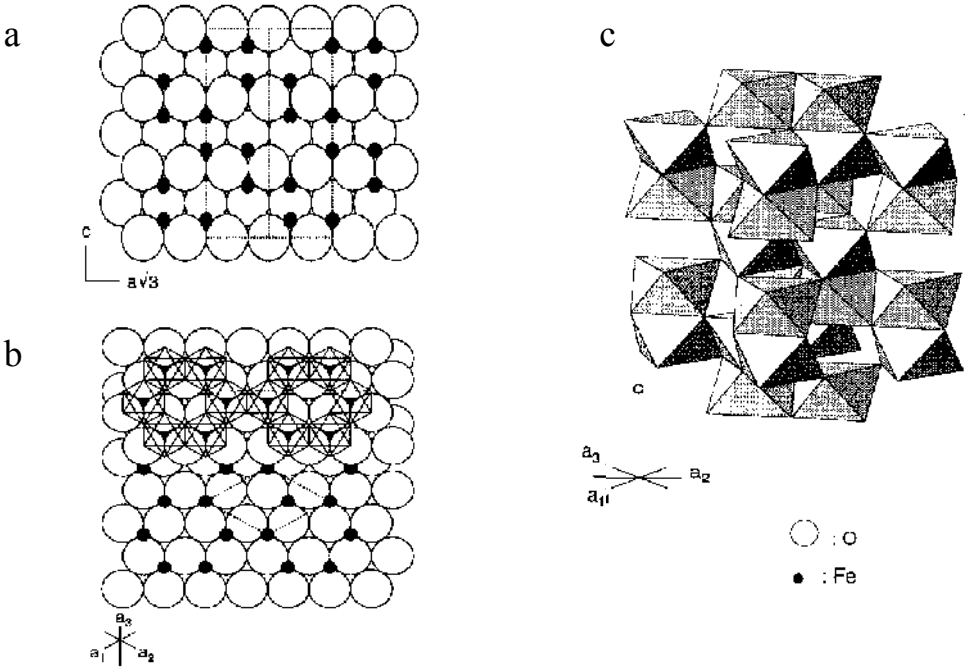

Figure 5: Structure of hematite [67]

a) Hexagonal close packing of oxygen atoms with cations distributed in the octahedral interstices

b) View down the c-axis showing the distribution of Fe ions over the given oxygen layer and the hexagonal arrangement of octahydra, and

c) Arrangement of octahydra.

The surface area of haematite depends on the production process and calcination temperature. The calcination temperature influences the haematite surface area. Normally, the haematite produced at 800-900°C has areas below 5 m^2/g due to the sintering of the hematite particles obtained by dehydroxylation of FeOOH or ferrihydrates at temperatures lower than 500-600°C are mesoporous with a surface area of up to 1000 m^2/g [66].

Maghemite is the gamma phase of iron oxide. It is a metastable phase isostructural to magnetite but with cation deficient sites. It differs from magnetite in that most of the Fe is in a trivalent state. The cation vacancies compensate the oxidation of the Fe^{II} in magnetite. Maghemite has a cubic unit cell. Each cell contains 32 O ions, 21.3 Fe^{III} and 2.3 vacancies. The cations are distributed randomly over the 8 tetrahedral or 16 octahedral sites whereas the vacancies are confined to the tetrahedral sites.

Iron oxide may also be produced by oxidising diluted gaseous iron-containing precursors such as iron pentacarbonyl or ferrocene in a heated oxygen environment in the gas phase. This method can produce a nano iron oxide in the haematite phase with a particle size in the range of 3 nm [66].

The iron oxide based catalysts are expected to survive for years and to achieve this; iron oxide is usually dispersed on supporting materials such as silica or alumina which enhances its resistance to thermal deactivation and also increases the surface area.

2.7. Influence of support on catalytic activity

Supported metal catalysts are used in many commercially important industrial processes such as pollution control and pharmaceutical production. Supports are usually not only used to increase the metal dispersion but also to reduce the catalyst price especially if noble metals are used. The use of supports provides a higher surface area, increases the catalyst regeneration ability as well as the catalytic activity and selectivity. In order to maximise the catalytic activity, it is of interest to synthesise small metal or metal oxide crystals in a range of 1-10 nm and then disperse them onto a thermally stable and high surface area support. The efficiency of metal utilisation is commonly defined as dispersion. Metal dispersion and the crystallite size are inversely proportional. That is to say nanoparticles with 1 nm diameter have a dispersion of 100%; in such a case every metal atom on the support is available for the catalytic reaction, while particles with 10 nm have a dispersion of only 10% while 90% of the metal surface is unavailable for the reaction [58].

The choice of a suitable support depends on numerous physical and chemical aspects such as the fixation and stabilisation of active sites, the formation of highly dispersed metal and the provision of a large surface area. The choice may also be restricted by the reaction conditions. Thus the support must be stable under process

conditions and should not interact with starting materials. In supported metal catalysts, the support may form metal-support interactions due to various physical and chemical effects. Those effects vary between electronic effects, adhesive force, formation of reduced support species over the metal surface or new phases formation. The electronic effects are varying from electron transfer to chemical bond formation. The electronic effects and their causes result from the n- or p-type semiconductor properties of the support material. These interactions have the advantage of enhancing the chemisorption capability and the catalyst activity, restricting the mobility of the disperse phase and delaying its sintering. In the last few years, the concept of strong metal–support interaction (SMSI) has gained considerable importance [68]. This interaction can enhance the chemisorption capability and effectiveness of a catalyst, as well as restrict the mobility of the disperse phase and delay its sintering.

2.8. Factors influencing the catalyst choice

The choice of a catalyst for a specific process actually depends on three important properties, i.e. the catalytic activity, selectivity and its stability.

2.8.1. Catalyst activity

Activity is a measure of how fast one or more reactions proceed in the presence of a catalyst. Activity can be defined in terms of the turnover number (TON) and the turnover frequency (TOF) to compare the catalysts activity. The TON is the number of cycles that a catalyst can run through before it deactivates, i.e. the number of reactant molecules that one molecule of catalyst can convert into product molecules per catalyst active site. The TOF is simply the TON/time, i.e. the number of molecules that one molecule of catalyst can convert into products within a time unit [57]. In practice, readily determined measures of activity are often sufficient. For comparative measurements, e.g. catalyst screening, the determination of process parameters and deactivation studies, the conversion can be used as a definition for activity. The conversion (X_A) is the ratio of the amount of a reactant A that has reacted to the amount that was introduced into the reactor [56]. For a batch reactor:

$$X_A = \frac{n_A^o - n_A}{n_A^o} \quad \text{in mol/mol or \%} \qquad (20)$$

Catalyst activity can also be measured in a different way, e.g. by studying the reaction kinetics and compare the rate of reaction at temperatures and concentration ranges that will be applied for the reactor. Studying the kinetics will not only provide information about the reaction rate but will also give hints for two things [57] :

1- How fast the reaction reaches the equilibrium
2- Studying the reaction rate leads to an understanding of the reaction mechanism by analysing the elementary steps of the chemical reaction.

The rate of a reaction can be measured by the rate of concentration change of a specific species ν_i that is for the reaction $A + B \longrightarrow C$ the rate is calculated as follows [69]:

$$R_i = d[C]/dt = d[A]/dt = d[B]/dt \qquad (21)$$

For the catalytic reactions it is better to calculate the rate constant relative to the reaction volume or the mass of catalyst. The reaction rate at some stages of reaction is found to be proportional to the reactant concentrations [A], [B]…etc raised to a power as in equation 16:

$$d[A]/dt = k[A]^a[B]^b \qquad (22)$$

Where k is the rate coefficient which is depending on the temperature but not on the concentration, a and b are the order of the reaction according to the concentration of A and B, respectively. The overall reaction order is simply the summation of the order of all reactants. The algebraic equation determines the rate; the rate constant is called the rate law. The reaction can be classified according to the reactants order to first and second or zero order reactions. For first order reactions the rate depends on the concentration of the reactant and the rate law for this reaction reads as follows:

$$[A]_t = [A]_o e^{-kt} \qquad (23)$$

While for the second order reaction, the rate law will be

$$[A]_t = [A]_o / 1 + kt[A]_o \qquad (24)$$

for most of the reactions, the rate constant is found to be temperature dependent. The temperature dependence of the reaction rate is given by the Arrhenius equation.

$$\ln K = \ln A - E_a / RT \qquad (25)$$

Where k is the rate constant, A is the pre-exponential factor and E_a is the activation energy. The Arrhenius equation can also be simply written as:

$$k = Ae^{-E_a / RT} \qquad (26)$$

For many reactions it is found that a plot of ln k versus 1/T will give a straight line. The slope of this straight line is equal to $-E_a/R$ hence the activation energy of the reaction can be calculated. As equations 26 and 21 show, there are three related possibilities for expressing catalyst activity, i.e. the reaction rate, the rate constant k and the activation energy E_a.

2.8.2. Catalyst selectivity

Selectivity is the ability of the catalyst to direct the conversion of the reactant to a desired product along a specific pathway [59]. This means that different products will be obtained over different catalysts. For example syngas (CO and H_2) can be converted to different products such as methane, methanol, ethylene, glycol and others as seen below:

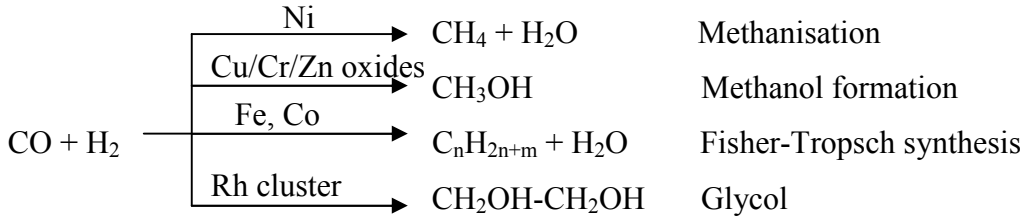

2.8.3. Catalyst stability

The total catalyst lifetime is a crucial factor for the industrial process economics. So the chemical, thermal and mechanical catalyst stability must be studied to determine its lifetime [56]. The catalyst stability could be affected by many factors such as decomposition or coking (carbon deposition over its surface). The catalyst deactivation can be followed by measuring the catalyst activity and/or selectivity as a function of time. Today, the rationing of raw materials and energy is of great importance so that for many reasons the target quantities should be given as selectivity > stability > activity order of priority.

2.9. Methods of reaction tracking

As it becomes clear from the previous discussion for reaction rate determination, the basic data needed for the rate constant calculation are the time-dependent concentrations of reactants and products. To follow the reaction changes there are many methods used to monitor the concentrations. The choice of a method depends on the reactants type and how fast its reaction is. Generally these methods vary from total pressure change measurement to highly sophisticated precise methods [69].

The simplest method of following a reaction is to measure the pressure change during the reaction. This method is used when at least one component exists in the gas phase and its consumption or production will cause a pressure difference. A disadvantage of this method is that it is not specific since all gases all gases present will contribute to the pressure

The second possible method is spectroscopy. This method is recommended when one component has a high characteristic absorption. For example, the bromine concentration can be monitored by using the visible light absorption in HBr formation reaction.

The electrochemical method offers another solution to follow the reactions in which change in the type or number of ions occur. This can be followed by monitoring the pH value or the conductivity measurement. A typical example of this is the electro-oxidation of ethanol.

Other important methods include gas chromatography, polarimetry, magnetic resonance and mass spectrometry is occasionally applied.

2.10. Principles of mass spectrometry

Mass spectrometry is a completely different analytical method from the other molecular spectroscopic analysis techniques, e.g. infrared, ultraviolet and nuclear magnetic resonance, theoretically and experimentally. Thus, in all these spectroscopic methods a form of electromagnetic radiation is absorbed and leads to the formation of excited molecules which will eventually return to their ground state level, and the process will be repeated. In mass spectrometry, however, the molecules are ionised and the ions are then detected [70]. The ionisation can be achieved in many ways but in most cases it involves the application of energy greater than the ionisation energy. Commonly, this is done by directing a beam of electrons at the vaporized sample. The ionising electrons may have energies in the range of 20 to 75eV where, but the energy is generally set at 70 eV [71] since this value is so far above that required to ionise the molecule. Some of the excess energy supplied may be transferred to the ions formed in this way. These formed ions with high energy may partition this energy in many ways. The most important of those possibilities is the formation of electronically excited ions. Those ions are usually unstable and dissociate, that is commonly referred to as fragmentation. As a result of fragmentation process, positively charged fragment ions are produced. It is not necessarily that all molecular

ions decompose into fragment ions. Some compounds such as the aromatic compounds may produce relatively stable positively charged ions because of resonance stabilisation; a molecular-ion peak will be recorded with high intensity. On the other hand, compounds such as aliphatic alcohols, which do not produce such stable fragments decompose almost completely into fragment ions hence their spectrum will show only a small molecular ion peak. In a mass spectrometer, ions moved from one location to another such as the m/z analyser and detector. Due to this, in order to produce individual ions free from other forms of matter and to ensure that ions can effectively travel without interference. mass spectrometer must be evacuated to a high vacuum ranging from 10^{-4} down to10^{-7} Pascal [71]

2.10.1. Quadrupole mass analyser

In mass spectrometry, various types of analysers are used to separate and detect the formed ions. The mass analyser is used to separate and detect the ions according to their m/z, and relies on their behaviour in the presence of electric or magnetic fields. In the present study a quadrupole mass analyser was used.

In a quadrupole mass analyser, as schematically shown in figure 6, an electric field in combination with radio frequency electromagnetic fields are used as a mass filter. The quadrupole analyser mechanically consists of four parallel rods with a hyperbolic cross section. This configuration allows the generation of a hyperbolic electric field according to the quadrupole theory [72, 73], the opposite surfaces are then electrically connected.

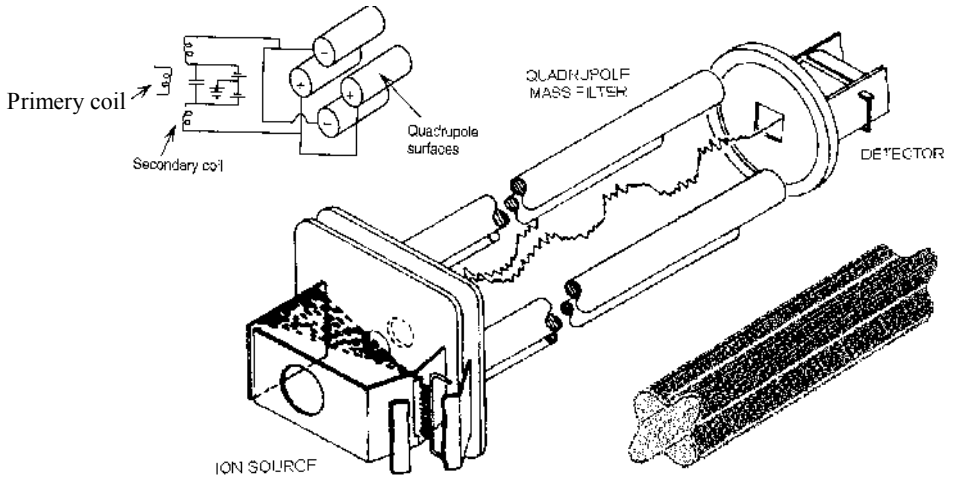

Figure 6: Schematic diagram of a quadrupole filter [71]

The mass filter is shown at the lower while the figure at the upper left illustrates the electrical means of superposing RF and DC potentials on the quadrupole surface.

They are connected to the DC and radio frequency power sources. The ions thus extracted are then accelerated into a central space inside the quadrupole electric field towards the detector where their spectrum is recorded. When analysing a mass spectrum, the most intense ion should be assigned first. Metastable ions should be used, if available, to determine fragmentation routes, as this often helps distinguish alternative structures [74].

2.10.2. Mass spectra for ethanol oxidation

For the mass spectra of methanol and ethanol, the basic peak of both is 31 m/z corresponding to $CH_2{=}OH^+$ which is formed by the loss of CH_3 from ethanol or higher alcohols which shown as a peak at 15 m/z. These processes of α-bond cleavages are competitive. Ethanol also shows beaks at 45, 46 assigned to the $C_2H_5OH^+$ molecular ion and $CH_2CH_2OH^+$ α-hydrogen cleavage fragment respectively. For ethanol and higher alcohols the loss of alkyl groups are far preferable to the loss of a hydrogen radical produced by methanol. This was explained by Stevenson in the 1950s. According to him, the molecular ion is highly energetic and tries to lose its energy so fast. Moreover, the alkyl group has many bonds which can be at higher vibrational states and it thus absorbs the excess energy from the molecular ion and leaves it. Hydrogen atoms, on the other hand, can only depart with kinetic energy.

Acetaldehyde is on of the primary product for ethanol oxidation. Generally, for aliphatic aldehydes the molecular ion CH_3CHO^+ is usually observable but frequently weak. The loss of α-H atom is a characteristic feature for aldehydes. Commonly, the basic beak of aldehydes is 29 m/z corresponding to CHO^+ fragment arias from the loss of CH_3 from the aldehyde. A second feature for the aldehydes is a β-cleavage. This cleavage represented by a beak at 43 m/z corresponding to CH_2CHO^+ end group.

Methane, as an ethanol oxidation by-product, gives an intensive peak at 16 m/z corresponding to the molecular ion and at 15 m/z assigned for CH_3 fragment. Also a peak at 2 and 14 m/z are observable due to the CH_2 fragment and H_2 molecule formation. Ethylene is another by-product of ethanol oxidation that gives a basic peak

at 28 m/z which represents the molecular ion $C_2H_4^+$. As oxidation end products CO and CO_2 also detected at 28 and 44 m/z respectively. Hydrogen also is one of the important products from ethanol oxidation that is recorded at 2 m/z.

2.11. Catalyst deactivation

The catalyst deactivation is a term that describes the decline of the catalyst activity after some time of reaction. Some catalysts are deactivated after a few minutes and others can survive for many years. The deactivation process, also known as aging, occurs due to many reasons like catalyst poisoning of one of the products, thermal processes and sintering of the catalyst, and finally deactivation may occur as a result of coking.

2.11.1. Catalyst poisoning

In this process, the poisoning material is chemisorbed at the catalyst on the catalyst surface so that the number of active sites needed for the reactant adsorption is reduced. Typical examples of catalyst poisons are H_2S, NH_3 and CO in many processes [59]. Poisons can be weak or strong. Weak poisons adsorb reversibly so that the catalyst activity can be secured. In case of strong poisons, the poisons chemisorbed irreversibly over the catalyst surface in competition with reactants leading to decline in the catalyst activity. For example, CO produced in methanol or ethanol oxidation poisons the Pt catalyst used in fuel cells. Reaction products that diffuse only slowly away from the catalyst surface thus disturbing the course of the reaction are referred to as inhibitors [56]. In some cases it is desirable to poison the catalyst partially to lower the catalyst activity or to influence the selectivity. The addition of ppm quantities of H_2S in catalytic reforming with nickel catalysts is an example of such a concept. That is because nickel has a higher hydrogenolysis activity, which leads to the formation of gases and coke. In addition to sulphur poisons, the most active hydrogenolysis centralises and thus influences the selectivity towards the desired isomerisation reactions.

2.11.2. Thermal processes and sintering

Deactivation due to thermal processes includes the change of catalyst chemical composition [56]. When the catalyst is subjected to high temperature, one or more metastable phases are formed from the active components or the support materials.

Phase changes can limit the catalyst activity or lead to catalyst–substrate interactions. Transformation of the TiO_2 anatase phase to rutile during the course of reaction is an example of the thermal deactivation process.

In the sintering process the catalyst loses the active surface area resulting in a decreased catalyst activity [59]. The loss of surface area is the result of the clustering of highly dispersed individual metal atoms. New crystallites can even be produced by sintering due to the process of particles migration and subsequent coalescence. The sintering process in an oxidation environment results in a volatilisation of oxides and a deposition of more stable metals at the crystallite centre. However, the result of sintering in inert media is that the particle growth is inversely related to the cohesive force strength in the metal crystallite.

2.11.3. Coking deactivation process

The blocking of the catalyst active sites and/or pores due to deposition of some polymeric components, especially coke, are a widely observed cause for the deactivation. Those polymeric components are usually formed from the side reactions taking place during the main course of reaction. At high temperatures (above 200 ^oC) these polymers are dehydrogenated to carbon, a process known as coking. Especially, catalysts with acidic or hydrogenating/dehydrogenating properties cause coking. With dehydrogenation catalysts, coke is formed according to the mechanism in which a dehydrogenation step is followed by hydrogenolysis what leads to the formation of carbon fragments C_x . The latter are highly reactive and are bound in a carbide-like fashion or are present as pseudo-graphite. In the presence of acidic support materials, the C fragments migrate from the dehydrogenation centres of the metal to the support, where they are cleaved analogously to acidic catalysts [56].

CHAPTER 3
REVIEW OF THE PREVIOUS WORK

3. Review of the previous work

Bio-ethanol is a renewable energy source that can be easily produced from many biomass sources, including waste materials of the agricultural and forestry industries. Ethanol is widely available, safe to handle and easy to store and transport. Furthermore, a bioethanol-to-hydrogen system has the major advantage of being nearly CO_2 neutral since the carbon dioxide in the process is consumed for biomass growth, offering a nearly closed carbon loop. The increased attention paid to ethanol has resulted in a number of studies on hydrogen production from ethanol via steam reforming or catalytic partial oxidation [75-77]. Based on a thermodynamic analysis, the feasibility of the process [78-80] was established and several catalysts have been proposed that show sufficient activity and stability to be considered for practical applications [13, 81, 82].

In previous studies on the ethanol partial oxidation, most interest has been focused on active metals, such as noble and non-noble metals, and supports with the purpose to find suitable operating conditions that provide a high H_2 yield and a stable catalyst [83]. Most of these investigations were carried out at temperatures ranging from 300°C to 800°C [20, 39, 84, 85]. The present study, however, investigates the catalytic activity of a cheap metal oxide which is the iron oxide in a low temperature range from 240°C to 290°C. The objective is to optimise the conditions of the ethanol oxidation process in order to produce a high hydrogen yield and selectivity. The study also investigates the stability of the different iron oxide catalysts and the effect of a catalyst change on the H_2 production.

3.1. Effect of first row transition metals on the catalytic activity in the ethanol partial oxidation process

One of the earlier investigated catalyst series for the ethanol partial oxidation process is the unsupported and supported metal from the first row of transition elements such as Ni, Co and bimetals such as Ni-Fe catalyst systems.

Cavallaro [86] investigated Co-based catalysts for the hydrogen production over different supports. The catalysts were only suitable for the ethanol partial oxidation process at a higher loading level of the active phase (i.e. 20 wt. %). The influence of the supports on the hydrogen production was investigated. Cavallaro claimed that the supports behave differently as functions of their nature. According to [86] the

Co/MgO catalysts have been found more stable than Co/Al_2O_3 (low coke formation) but required higher contact times. All supported Co catalysts severely suffer from oxidation of the active phase whereas the catalyst deactivated after only 200 minutes on stream**.**

Although a series of the first row transition elements and noble metals have been investigated as the active catalytic component for ethanol partial oxidation [39, 40, 84, 86], most of the earlier studies have used Ni supported catalysts, due to the significant scope of knowledge gained from industrial steam reforming processes as discussed in the following:

Liguras *et al.* [20] studied catalytic partial oxidation of ethanol over structured Ni/La_2O_3 supported on cordierite monoliths, ceramic foams made from mullite and zirconia-alumina as well as γ-Al_2O_3 pellets catalysts prepared by three different methods: adsorption from solutions, the sol–gel method and wash-coating. The catalysts exhibit a very high activity towards hydrogen production with a very high ethanol conversion at 500^oC while the complete conversion was effected at temperatures above 550^oC. A selectivity of 90% and more than 97% was shown at $500^{\circ}C$ and/or $650^{\circ}C$ with methane as a main by-product; this selectivity decreased substantially with increasing temperature. With increasing the space velocity in a range from 3620 to 9055 h^{-1}, the ethanol conversion was complete; a very slight increase in hydrogen selectivity was shown, a small decrease towards the main by-product was accomplished and the CO_2 selectivity decreased slightly accompanied by a small increase in selectivity towards CO. The Ni/La_2O_3/monolith catalyst remained on stream for 70 h albeit with significant coke formation (1,2 g/l) which was considered as a process drawback.

The effect of the support on the Ni catalysts performance on steam reforming of ethanol was reported by Fatsikostas and Verykios [87]**.** The results showed that Ni/La_2O_3 catalyst presents a higher activity and selectivity towards H_2 than Ni/Al_2O_3, Ni/YSZ and Ni/MgO catalysts. The high stability of this catalyst was assigned to scavenging of coke deposition on the Ni surface by lanthanum oxycarbonate species which exist on top of the Ni particles during the reaction.

A limitation of these studies has been the use of catalysts in powder form. Handling and pressure drop problems make such a form unsuitable for practical applications. In particular, in applications where a very high reliability and low pressure drops are required, e.g. automobiles, the catalysts must be deposited on

structural supports which have an excellent structural stability and can operate in harsh environments including vibrations, thermal cycling and thousands of start-ups and shut-downs. Furthermore, the coke formation over the catalyst surface is a severe problem faced with when applying Ni- and Co-based catalysts. One solution to that is to introduce another metal that has the ability to enhance the Ni catalyst stability. The combination of two metals may result in beneficial synergistic effects. Partial oxidation of ethanol (POE) has also recently been reported on Ni–Fe catalysts as a method for H_2 production .

3.2. Effect of supported bimetallic systems on the catalytic activity

Iron has been used as an active component for the water–gas shift reaction (WGSR). It can effectively relieve carbon deposition and, above all, increase the selectivity for carbon dioxide. As a result, iron can increase the yield of hydrogen and decrease the carbon monoxide selectivity, which is crucial for the hydrogen-rich reformat gases as fuels for fuel cells. Additionally, iron is close to nickel in the group VIIIB of the periodic table, and has similar ion radii and electronic properties offering a possibility to improve nickel-based catalysts.

Wang *et al.* examine a series of the Fe-Ni catalysts at 473-573 K with the feed molar ratios of O_2/ethanol from 0-2 for ethanol partial oxidation. All catalysts showed a good performance. Among the catalysts, $Ni_{50}Fe_{50}$ has the highest ethanol conversion of 86, 91%, a selectivity of 50.66% on optimum conditions of 573 K and O_2/ethanol of 1.5, the highest hydrogen selectivity being obtained at O_2/ethanol = 1.0 and the lowest CO selectivity being obtained at a ratio of 2.0[63].

Hsu *et al.* found that iron enhances the Ni-based catalytic activity and hydrogen selectivity at low temperatures in auto-thermal reforming (ATR) of ethanol. Over the 10 wt% Fe loading Ni catalyst, a conversion of ethanol of 98.43% and selectivity for hydrogen of 108.71% can be achieved at 600^{o}C. Iron-promoted nickel-based catalyst not only promote the dehydrogenation of ethanol in ATR, but also increase the activity for acetaldehyde transformation through steam reforming, partial oxidation, and water–gas shift reaction process. The Ni-Fe catalysts selectivity towards hydrogen is higher than that for iron-free samples by 47.44% on hydrogen selectivity [88].

The further development of new efficient catalyst systems that exhibit an improved long-term stability and selectivity towards hydrogen production are highly desired. Based on the influence of the nature of both the metal and support on the

catalytic characteristics of supported metals, the choice of these elements is a key factor in developing supported catalysts which fulfil the above requirements. Several transition metals, such as Pt, Rh, Pd and Ru, are found to be active for ethanol partial oxidation [12, 62, 89] and will be discussed next.

3.3. Catalytic activity of noble metals towards ethanol oxidation

Salge *et al.* [40] studied the partial oxidation of ethanol over noble metals (Rh, Ru, Pd and Pt) and metal plus ceria-coated alumina foams at 973 K and C/O = 0.7. Rh–Ce was more stable than noble metals alone. Concerning H_2 selectivity, Rh–Ce presented the highest H_2 production (80%). Among noble metals, Pt and Pd showed the lower formation of H_2 (<50%). The by-products obtained were CH_4, C_2H_4 and acetaldehyde for all catalysts. However, Pt, Pd and Rh exhibited a higher selectivity to CH_4 and C_2H_4 than Rh–Ce. The better performance of Rh–Ce was assigned to redox properties of Ce.

A comparative study between steam reforming, partial oxidation, and oxidative steam reforming of ethanol was done by Cai *et al.* [84] over an Ir/CeO_2 catalyst. The catalytic activity was compared using turnover frequencies (TOFs) under different conditions. The catalytic activity towards the different process followed the order of POE>OSR>SR, demonstrating that the presence of oxygen greatly promoted the surface reaction of ethanol. This is explained by the lattice oxygen of ceria initially participated in the activation of ethanol through the Ce^{4+}/Ce^{3+} redox cycle and the oxygen in the feed immediately supplemented to the oxygen vacancies, which improved the reaction rate. For POX with an ethanol/O_2 molar ratio of 1:0.6, CO_2 was the dominant product at lower temperatures indicating the enhanced oxidation of ethanol.

The role of the noble metal in the enhancement of the oxygen storage capacity is explained such that part of the added metal forms small oxide clusters within the ceria fluorite structure, acting as a privileged pathway for oxygen diffusion and storing [90 , 91].

Mattos *et al.* studied the effect of the metal nature on the performance of ceria-supported catalysts for ethanol partial oxidation at 573 K and O_2/ethanol molar ratio of 0.5 [62]. The results revealed that the Pt/CeO_2 catalyst produced the higher initial activity (>80%) and the product distribution was strongly affected by the nature of the

metal. Acetaldehyde was practically the only product formed on the Co/CeO_2 catalyst while methane was also produced on Pt/CeO_2 and Pd/CeO_2 catalysts.

Silva *et al.* [92] investigated the effect of metal nature on the performance of Y_2O_3 supported catalysts for partial oxidation of ethanol over Ru/Y_2O_3 and Pd/Y_2O_3 catalysts in a wide range of temperatures (473-1073K) with O_2/ethanol = 2. Over Y_2O_3 support, up to 773 K, a complete ethanol conversion was achieved with high selectivity to water and acetaldehyde. Above 773 K, a maximum H_2 selectivity of 14% at 1073K was shown, CO formation favoured up to 873 K, for CO_2 and CH_4 only small amounts (4–6%) were observed. For Ru/Y_2O_3 and Pd/Y_2O_3 catalysts, the complete ethanol conversion was achieved at 873 K. In contrast with Y_2O_3 support, significant amounts of H_2 were produced at temperatures higher than 673 K. Ru/Y_2O_3 catalysts were more selective towards H_2 (maximum 59% at 1073 K.) than Pd/Y_2O_3 in the studied temperature range. Pd/Y_2O_3 has a higher selectivity to CO of 40% at temperatures between 473 and 773 K. However, a 15% CO selectivity was obtained over Ru/Y_2O_3. Both catalysts were quite stable for 20 h time-on-stream with no significant carbon deposition on the catalyst surface.

From the above studies it is concluded that, among the noble metals, the Pt supported catalyst exhibits the best thermal stability and a relatively high C–C bond breaking [22], and WGS [85] activities of Pt make it a suitable active phase for ethanol reforming reactions. Recently, Mattos and Noronha reported that the support plays an important role on the product distribution obtained on POX over Al_2O_3, ZrO_2, CeO_2 and $CeZrO_2$ supported Pt catalysts [93], so further investigations for the role of support in Pt catalyst activity were reported [15, 16, 22, 29].

3.4. Effect of support on the catalytic activity of noble metals

Liguras *et al.* [89] tested a series of Ru supported cordierite monoliths, ceramic foams and γ-Al_2O_3 pellets catalysts for the production of hydrogen by catalytic partial oxidation of ethanol. Ru/cordierite monolithic-γ-Al_2O_3 exhibited an excellent catalytic performance with excellent selectivity to hydrogen (>90%) for a wide variety of process conditions including an excellent long-term stability and low amounts of coke deposition. Comparing all catalytic systems, they are all able to completely convert ethanol with a high selectivity towards the desired products. The Ru supported ceramic foam catalyst provided a comparatively better performance probably due to the smaller pore size and higher tortuosity of this support.

The effect of ceria content (1–20 wt%) on the properties and catalytic performance of Pt/CeO_2-Al_2O_3 catalyst was studied by A. Santos [94]**.** Results showed that the catalytic activity and stability of Pt/CeO_2–Al_2O_3 catalysts strongly depend on the CeO_2 content. The catalysts with high CeO_2 loading (>12 wt.%) showed a higher catalytic activity and stability in the reaction of partial oxidation of methane. Therefore the support identity is crucial to obtain catalysts resistant to carbon deposition. The high catalytic activity and stability of the catalysts is attributed to the combination of different properties:

(i) The presence of a CeO_2 fluorite structure leads to a higher oxygen storage capacity (OSC) and reducibility.

(ii) The high Pt dispersion increases the Pt/CeO_2 interface area.

The partial oxidation of ethanol over Pd/CeO_2 and Pd/Y_2O_3 catalyst was investigated by Costa *et al.* [39]**.** The results revealed that the complete ethanol conversion was achieved at 873 K for Pd/Y_2O_3 and 973 K for Pd/CeO_2. Pd/CeO_2 exhibited a higher activity than Pd/Y_2O_3 at temperatures > 673 K to H_2, CO_2 and acetaldehyde, whereas the CO formation was favoured on Pd/Y_2O_3 catalyst. In addition, an increase of temperature results in a decrease of acetaldehyde and water formation. Over Pd/CeO_2 catalyst, the highest hydrogen selectivity was reached at 1073 K while the selectivity towards CH_4 showed a maximum value at 873 K and slightly decreased above 1000 K. The low activity of Pd/Y_2O_3 catalyst was explained by the low reducibility of Y_2O_3 which led to a lower fraction of active sites.

Bi *et al.* [95] Studied the catalytic activity of 1.2% Pt loaded on Al_2O_3 (1.2% Pt/Al_2O_3) and (1.9% Pt/ZrO_2). Samples were prepared by incipient wetness impregnation and/or the sol–gel method to examine ethanol partial oxidation over the temperature range of 373-473 K. The results showed that the performance of supported platinum catalysts depended on the reaction temperature and the catalyst used. In other words, Pt/ZrO_2 catalyst showed a high hydrogen selectivity (S_{H_2} > 95%) with a negligible S_{CO} on mild oxidation condition of O_2/ethanol > 0.75 and at a temperature of < 400 K. However, hydrogen selectivity was significantly deteriorated at a high O_2/ethanol ratio and/or at high reaction temperatures, while the Pt/Al_2O_3 catalyst showed a high S_{H_2} (>90%) and also a high S_{CO}. According to these results, the author claimed that the POE under mild condition may be developed as an efficient process to produce hydrogen from ethanol. The variations of S_{CO} over Pt/ ZrO_2 and Pt/Al_2O_3 at 373 K were explained by the reducibility of ZrO_2 which can provide the

lattice oxygen that has a high activity for oxidation of CO to CO_2, while in the case of non-reducible Al_2O_3 oxygen molecules have to be adsorbed on the Pt surface which has less effectiveness than providing lattice oxygen for CO oxidation. CeO_2 has been used either as an effective promoter or support due to its characteristic oxygen storage capacity (OSC) allowing to store and release oxygen and leading to the presence of highly active oxygen. This makes the catalyst more active in many carbon formation-related reactions of hydrocarbons, such as steam reforming, dry reforming and oxidation. The specific role of CeO_2 involves the storage and release of oxygen for the oxidation of CO and hydrocarbons. Additionally, CeO_2 also improves the dispersion of the active phase [6, 18, 21]. Previous studies have shown that the addition of ZrO_2 to CeO_2 improves the redox properties, oxygen storage capacity and thermal stability; it also promotes water-gas shift, steam reforming and CO oxidation reactions in the SR and OSR of ethanol [8,18,21,22]. CeO_2–ZrO_2 composites also exist, but they have disadvantages, such as cost and a low surface area which might render these composites impractical in terms of stability and expense [83].

Although a high yield of hydrogen can be achieved using noble metal based catalysts such as Pt/CeO_2, the high cost of noble metals limits its practical applications**.** However, using an active and cheep catalyst at relatively low temperature is more attractive from the practical point of view as discussed in the next part.

3.5. Iron oxide activity for oxidation reaction

Since the end of last century, iron catalysis has become a “hot topic” due to the obvious advantages such as availability and price. Traditionally, iron is normally used as Lewis acid in homogeneous catalysis, for example the oxidation of phenols, or as catalyst or support in heterogeneous catalysis [96-99]. Among almost all iron complexes, iron oxides have often been considered to be catalytically inactive under mild reaction conditions. However, some iron oxides can be used as magnetically separable support [100-103]**.**

Chang *et al.* [104] compared the catalytic activity of bulk Fe_2O_3, Au/Fe_2O_3, Ru/Fe_2O_3 and Au–Ru/Fe_2O_3 catalysts prepared by the deposition–precipitation method for hydrogen production by the partial oxidation of methanol (POM). The bulk Fe_2O_3 showed only a very low methanol conversion and produced a negligible amount of hydrogen and carbon monoxide along with 14% of methane. The bimetallic Au–Ru/Fe_2O_3 catalyst exhibited 100% methanol conversion against 84.0 and 80.0%

over Au/Fe_2O_3 and/or Ru/Fe_2O_3. A high hydrogen selectivity of 82.0% was found over $Au–Ru/Fe_2O_3$ catalyst. Methane was not detected in all supported catalysts. The CO selectivity was represented in order of Fe_2O_3< Au/Fe_2O_3< Ru/Fe_2O_3 > $Au–Ru/Fe_2O_3$. The significantly higher activity of the supported iron oxide compared to the bulk iron oxide is due to some specific interaction between the metal and iron oxide support. In this catalyst, the Au–Ru weakens the Fe–O bond thus increasing the lattice oxygen mobility to a higher extent than in Au/Fe_2O_3 and Ru/Fe_2O_3 catalysts.

Shi *et al.* [64] showed that nano-iron oxide is an active and selective catalyst for aromatic alcohol and olefin oxidation to the corresponding aldehydes. In his work, a comparative study between bulk and nano scale γ- and α-Fe_2O_3 with different particle size was done. The result showed that bulk γ-Fe_2O_3 and α-Fe_2O_3 are poorly active with a conversion of around 5%; further, low catalyst turnover numbers (TONs) were obtained. Higher catalyst activity represented by conversion of 33% with a 97% selectivity was achieved at 75^{o}C when nano-γ-Fe_2O_3 with a particle size in the range from 20 nm to 50 nm was applied while the activity increased to 86% with smaller particle size of 3–5 nm. When increasing the catalyst amount, the conversion increased simultaneously but the selectivity and TONs decreased. Accordingly, a suggestion was made that the main reason for the improved activity of nano-iron oxide probably originates from the nanolisation of the bulk-iron oxide. Theoretically, it may be assumed that, with a decrease of the particle size down to a “molecular” level, the nano-catalyst behave as a homogeneous system in which the catalytic activity is not controlled by the surface area of the catalyst but governed by the concentration. In general, nanolisation of heterogeneous catalysts offer higher surface areas leading to more low-coordination sites and surface vacancies. These are responsible for the higher catalyst activity [105-107]. Depending on the previous study on iron oxide catalysts, the catalytic activity for unsupported iron oxide with different phases and supported catalysts was studied in this work on the ethanol partial oxidation to produce hydrogen.

CHAPTER 4
EXPERIMENTAL

4. Experimental

In this chapter detailed experimental procedures used to produce iron oxide, SiC and Fe_2O_3/SiC nanoparticles will be discussed. Also the procedures used to test their catalytic activity towards ethanol partial oxidation were reported. The catalytic activity for bulk α-Fe_2O_3 was compared with the prepared γ-Fe_2O_3, α,γ-Fe_2O_3 and α-Fe_2O_3 nanoparticles phases as well as five samples α-Fe_2O_3/SiC nanoparticles. The γ and α, γ-Fe_2O_3 nanoparticles samples were prepared by means of the MOCVS method provided by Orthner and Roth [108]. A similar method was also used in the present work to produce α-Fe_2O_3 and Fe_2O_3/SiC samples but with a home-made set up. The analytical methods used to identify the particles morphology, chemical composition and particle size techniques are also discussed. The needed equations to calculate the gases velocities used to prepare the particles and the catalytic activity, yield and selectivity are provided at the end of the part on catalytic activity measurements.

4.1. Sample preparation

The particles of α -Fe_2O_3 and a series of α -Fe_2O_3/SiO_2 nanoparticles used in this work are prepared by the MOCVS process. In this process a hot wall reactor, schematically shown in Figure 4, is used to precipitate the samples.

4.1.1. Setup of the hot wall reactor

The setup of a hot wall reactor is schematically shown in Figure 7. It consists of a ceramic tube reaction chamber, purchased from the Körner & Stein Company, with a 28 mm inner diameter and 1000 mm length. The reactor tube is made of mullite which is an Al_2O_3 ore. The reaction chamber is placed inside a two opened side tube furnace supplied by HTM Reetz GmbH, type LK 1250-45-500-3, 50 Hz. The furnace is a horizontal, electrically controlled heated tube with 600 mm length and 30 mm width and designed for a maximum temperature of 1150^{o}C. The precursor used as starting material to deposit the nanoparticles was loaded in a glass bubbler with two KF 16 flanges at its end to be connected to the chamber through stainless steel tubes with a 6 mm outer diameter. In order to provide the temperature for ferrocene precursor sublimation, the precursor containing bubbler is heated by an electrically heated temperature controlled silicon oil bath. For tetramethylsilane (TMS), the evaporator is cooled down to -10^{o}C in a similar acetone bath. The inlet used to

introduce the precursor vapour pressure was a simple stainless steel tube with a 6 mm outer diameter which was inserted inside the chamber through a KF 50 flange. The supply line of the ferrocene vapour was heated by resistive wire heaters wrapped around the tube in order to prevent the source vapour from condensation.

The exhaust was released through an exhaust line connected to the chamber tube from the ferrocene inlet side through a three ways tube (item 15 in the schematic diagram). To produce a pure single material, such as iron oxide, only one precursor is used on one end and an exhaust tube is directly connected to the other end of the reaction chamber.

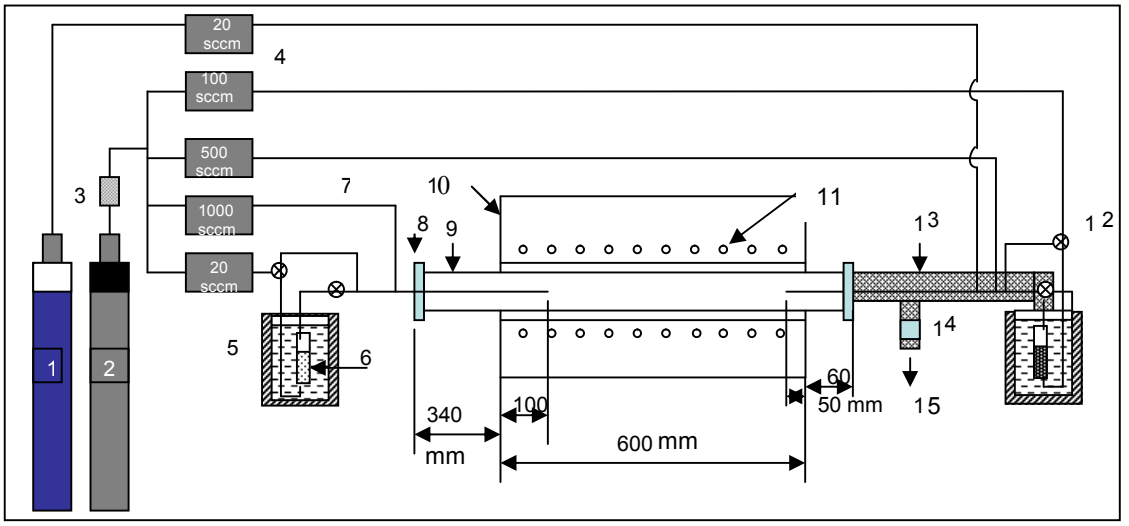

Figure 7: Schematic diagram of the HWR reactor used for sample preparation

1) O_2 cylinder, 2) N_2 cylinder, 3) dehydrator molecular sieves, 4) mass flow controller, 5) temperature electrically controlled acetone bath, 6) glass bubbler, 7) 6 mm stainless steel tubes, 8) KF 50 flange, 9) ceramic tube, 10) electrically control furnace, 11) heating coil, 12) 3-way valve, 13) wire heater, 14) cellulose filter 15) exhaust line

4.1.2. Precursors

For the MOCVS process, ferrocene $Fe(C_5H_5)_2$ with a purity of > 98%, purchased from Fluke, and tetramethylsilane $(CH_3)_4Si$, supplied by Merck, symbolised as TMS, were used as precursors to precipitate iron oxide and/or silicon carbide nanoparticles. In some experiments both were used together to produce α-Fe_2O_3/SiC.

For silicon carbide preparation tetramethylsilane (TMS) was chosen as a precursor because it is known to form crystalline SiC films in CVD processes [109], tetramethylsilane is a colourless liquid, highly volatile, easy-to-handle, non-explosive, slightly toxic and has a low hydration ability. It has a low water solubility and no chlorine ligands [110] which are difficult to remove from the final product. It

has the advantage of easy storage and transportation more than other silicon precursors such as silane. TMS has a very high vapour pressure of 1013 mbar and enthalpy of sublimation -231.8 kJ/ mol due to its low boiling point of 26°C [111, 112]. All those reasons make the TMS the most promising precursor for the SiC production by CVS.

Ferrocene is a yellow/ orange coloured powder which is commercially available, inexpensive, easy to handle, stable under atmospheric conditions and also a nontoxic material. There were reported some sublimation enthalpies for it at different temperatures. For example, from the NIST web book sublimation enthalpy found to be 72.5 kJ/mol at 292-300 K and 70.3 kJ/mol at 294-302 K) [111] and 72.659 kJ/mol at 295-325 K was also reported by Siddiqi [113, 114]; ferrocene had a low vapour pressure of 0.0133 mbar at 30°C [115]. In order to supply the ferrocene vapour to the CVS chamber, an elevated temperature is required to vaporise it with a sufficiently high vapour pressure to produce the particles. Since ferrocene is a thermally stable material, a relatively high pyrolysis temperature of more than 500°C is needed.

4.1.3. Reaction procedure

In a typical experiment, the furnace is first gradually heated up to the desired reaction temperature by a rate of 10^{o}C/ min. Then 1.5 g of ferrocene as a precursor for iron oxide is filled to a glass bubbler which is later immersed in an oil bath and heated gradually up to evaporation temperature. According to the data mentioned above, ferrocene has a vapour pressure of 0.0133 at 30°C mbar and 72.5 kJ/mol as enthalpy of sublimation, the vapour pressure at 100°C was estimated by the Clausius-Clapeyron equation to be 2.95 mbar. The line to the furnace was then heated up to 30^{o}C above sublimation temperature to prevent precursor condensation. A high purity nitrogen gas (99%, Messer), that passed through antioxidant and dehydrator molecular sieves, was used as carrier gas for the ferrocene vapour. Then the gas mixture of precursor and nitrogen was diluted with another nitrogen flow of 500 sccm. The oxygen flow needed to oxidise the iron was then supplied to the line at a flow rate of 5 sccm. In some experiments this oxygen flow was changed to see the effect of oxygen mol fraction on the prepared iron oxide phase. The mixture was then fed to the furnace through a 6 mm inlet tube which was inserted over 50 mm length inside the furnace. For silicon carbide, TMS was filled in a glass bubbler and frozen into liquid nitrogen prior to the experiment in order to avoid humidity that might be found in the

bubbler during the filling procedure. Then the bubbler was immersed in an acetone bath to cool it down to -10°C to lower its vapour pressure. At -10°C, the vapour pressure of TMS was calculated to be 250 mbar. A flow of nitrogen was also used as carrier gas through the TMS bubbler. It was diluted again with a nitrogen flow of 179 sccm, and the mixture was fed to the furnace. All precursor flows were mixed in the furnace to produce the corresponding particles. All the gas flows were actively controlled during the experiments by means of mass flow controllers (MKS). The exhaust gases were then exited to the exhaust line at the other end of the furnace. To prepare the supported iron oxide particles, both bubblers were used simultaneously.

4.1.4. Studied parameters

To produce the silicon carbide, supported and unsupported iron oxide nanoparticles, the following parameters were investigated: temperature, precursor mole fraction, diluent mole fraction, gas mixture velocity and residence time. Silicon carbide deposition was studied at temperatures ranging from 800°C to 1100°C. The effect of TMS precursor concentration in terms of mole fraction was studied in a range from $2.22 \cdot 10^{-3}$ to $66.6 \cdot 10^{-3}$ in order to produce the lowest possible particle size in a range of 10 nm. This was done by varying the nitrogen flow through the bubbler. Another way to analyse the precursor mole fraction effect on the particle size was by changing the diluent flow, hence by further decreasing the TMS mole fraction in a range from $2.22 \cdot 10^{-3}$ to $1.0 \cdot 10^{-3}$. The precursor mole fraction was calculated by taking into account its partial pressure relative to the atmospheric pressure and using the gas mixture flow assuming a saturation of the carrier gas with a precursor vapour pressure as shown in equation 1:

$$X_i = \frac{F_b \cdot \left(P / P_{atm} \right)}{F_t} \qquad (1)$$

Where X_i is the precursor mole fraction, F_b is the carrier gas flow through the bubbler, P is the precursor vapour pressure at the used temperature, P_{atm} is the atmospheric pressure and F_t is the total flow of the whole gas mixture.

The effect of gas velocity and residence time on the particle size and particle yield was also investigated. The velocity (V) was calculated from the known total flow rate ($\dot{v}$), the reactor volume and the material density using the continuity equation as following:

$\dot{m} = \rho \cdot A \cdot V$ in units of kg/s = (kg/m^3) (m^2) (m/s) (2)

Since $\dot{v} = V \cdot A$ [(m/s) (m^2) = m^3 / s] so, (3)

Velocity can be calculated as:

$V = \dot{v} / A$ (m / s) and (4)

Residence time (t_r) = $V / \dot{v}$ [m^3· s / m^3 = s] (5)

For iron oxide deposition, a temperature of 800°C was used due to the fact that below this temperature only a thin film of iron oxide can be produced [116]. The ferrocene mole fraction was varied in the range from $5.67 \cdot 10^{-5}$ to $1.98 \cdot 10^{-4}$. The effect of the different oxygen flows was also investigated within a range from 5 to 40 sccm what corresponds to 0.9% up to 7.6% of the total gas mixture flow. For the production of Fe_2O_3/SiC, the ferrocene mole fraction was studied within the range from $1.46 \cdot 10^{-5}$ to $1.1 \cdot 10^{-3}$ while the TMS was kept constant at $1.0 \cdot 10^{-3}$.

4.2. Catalytic partial oxidation of ethanol

4.2.1. Setup for testing the catalytic activity

Investigation of the ethanol partial oxidation over different catalysts was carried out in a closed loop recycle microbatch reactor. The system, schematically shown in Figure 8, was made of stainless steel. For catalytic activity investigations, the catalyst prepared was loaded into the reactor and sandwiched by two layers of glass wool. Ethanol was filled in a standard 10 ml measuring flask which was used as ethanol reservoir. This flask was glowed to a 6 mm tube and connected to the setup to supply ethanol vapour to the reactor.

A pressure gauge (MKS, model 626AX13MDE) was used to control and measure the ethanol vapour pressure, the oxygen and helium partial pressures which are later fed to the reservoir through two different inlet ways. The gas mixture was then fed through a 6 mm, stainless steel line to the reactor. The reactor was composed of a quartz tube with a length of 230 mm, an inner diameter of 6 mm and an outer diameter of 8 mm. The reactor was open from both ends. The reactor was embedded between two aluminium plates with a circular opening in the middle with an inner diameter of 8.1 mm to insure a uniform temperature distribution. To obtain the required reaction temperature, an electrically controlled resistive heater plate was used. The plate temperature was then adjusted by an electrically controlled temperature controller (± 0.2 °C) while the plate temperature was measured using a K

type thermocouple with a diameter of 1.2 mm. Another K type thermocouple was put in the middle of the catalyst sample used in order to monitor the actual catalyst temperature. The reactor was later connected to a four-way Swagelok stainless steel connector. The first inlet was used to conduct the thermocouple inside the reactor. For the other two ways, one side connected the reactor to a pressure gauge (Leybold vacuum, CTR91) for total pressure measurement inside the reactor while the third way was connected to a mass flow controller (MKS).

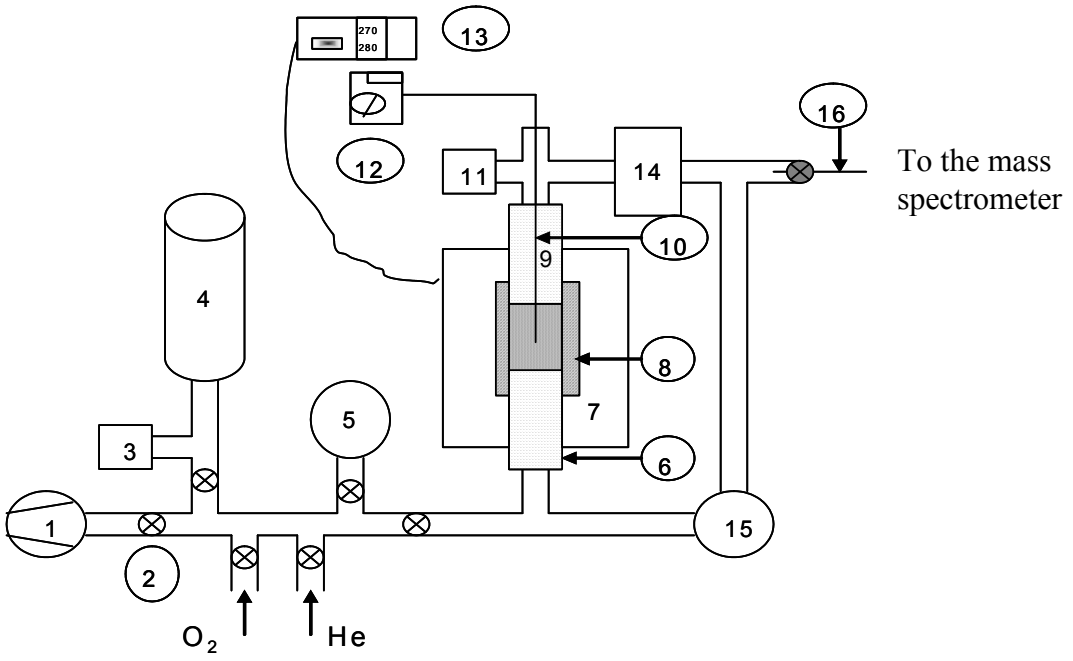

Figure 8: Schematic diagram of the micro-batch reactor used for catalytic activity measurements

1) Vacuum pump, 2) 2-way valve, 3) pressure gauge, 4) stainless steel gas reservoir, 5) ethanol reservoir, 6) glass reactor, 7) heating plate, 8) aluminium cube, 9) glass wool, 10) K-type thermocouple, 11) pressure gauge, 12) voltmeter, 13) heat controller, 14) mass flow meter, 15) circulating pump and 16) capillary tube

The mass flow controller had a capacity of 500 sccm min^{-1} and was controlled by means of a 4-way controller supplied by MKS GmbH to adjust and monitor both the gas flow and the pressure. The mass flow controller was adjusted at its maximum to provide a sufficiently fast flow in the reactor. It was then connected to two different connections, the first one was connected to a computer-interfaced QMS 200 type quadruple mass spectrometer (Pfeiffer) through a 13cm long capillary tube (1.6 mm) to follow the reaction components, and the other way was connected to a metal bellows pump (KNF, N022AN.9.18) for continuous gas circulation.

4.2.2. Catalytic activity measurement procedures

For a typical catalytic run, the mass spectrometer was evacuated down to $4.7 \cdot 10^{-7}$ mbar before gas inlet using a pump provided by Pfeiffer GmbH, model TMH07P. A certain quantity of catalysts corresponding to a desired surface area was placed in the middle of the reactor and held by glass wool. The total setup was evacuated to 0.1 mbar and the valve was closed upstream of the pump. Then the catalyst was resistively heated stepwise from room temperature up to the desired reaction temperature which was measured by a K-type thermocouple found in the centre of the reactor bed (0.5 mm thick and 1m long, supplied by KS GmbH) and continuously regulated using an electric precision temperature controller. Later 60 mbar of absolute ethanol vapour (max. 0.2% water, supplied by KMF) were fed into a stainless steel gas cylinder at ambient temperature by opening the two-way valve next to the flask and the valve upstream of the gas cylinder so that the gas could flow due to the pressure difference between the valves. Then ethanol was mixed at the desired oxygen pressure **(**purity of 99.99%, Messer**)** in that order and circulated for 2–3 min to ensure adequate mixing. The helium gas was later added to the mixture until a total pressure of 600 mbar was reached. The whole system was evacuated to 0.1 mbar after each gas inlet and also after all gas mixing.

The reactant mixture was then supplied to the reactor containing the catalyst by opening the gas cylinder valve and the manifold valve located directly upstream of the reactor until an internal partial pressure of ~ 600 mbar was reached; then both valves were closed. After closing the manifold valve, the bellow pump was switched on to circulate the gas mixture. At the same time, the needle valve for the mass spectrometer was opened to monitor the gas mixture by continuous leaking of the gas mixture into the mass spectrometer. The data of the gas mixture during the reaction time were recorded by using the "Quadrstar" programme on the computer. First the background composition was measured prior to each run. The catalytic run was then carried out for one hour. At the end of the catalytic run the flow of ethanol and oxygen gas mixture was stopped, the valve to the mass spectrometer was closed and the catalyst was gradually cooled down to room temperature.

In order to follow the reacting species, experiments were carried out to adjust the mass spectrometer operating conditions to identify the clearest and most stable peaks. These experiments were carried out by injecting pure helium, oxygen or

ethanol. Then the spectrometer ionisation energy was verified in a range from 50 to 110 eV and the corresponding peaks, noise and peak intensities were measured. If the ionisation energy was low, the noise was also lower and so were the peak intensities. Low noise with good peak intensity was determined at 70 eV so that it was taken as a set point for the ionisation energy. The spectrometer chamber was heated up to a source temperature of 50^{o}C. The spectrometer resolving power, the difference in m/z values of ions that can be separated from one another (Δm) divided by the specific m/z value (M) i.e. R= M/Δm, was adjusted at 1000 MS.

Further experiments were carried out to follow the reacting species by measuring a full spectrum of pure compounds which may be present during the reaction. This full spectrum was detected from a mixture of pure compounds with helium in specific concentrations. The highest peak intensity determined in the spectrum for each material was taken as a characteristic peak for this component, i.e. the peak at 31u was used to detect ethanol. The mass spectrometer signal intensities were also calibrated in order to obtain absolute values for the partial pressures of each component in the reaction loop. This was done by mixing a specific pure substance with helium at different partial pressures, and the characteristic peak intensity is then recorded. Later, a liner relationship between partial pressure and peak intensity was described.

4.2.3. Reaction parameters

The effect of several parameters on the catalytic activity towards hydrogen production and the product distribution were studied in order to optimise the reaction conditions. The temperature was the first parameter to be studied. Investigations were done in a temperature range from 260°C to 280^{o}C at a fixed O_2/ethanol ratio and particular catalyst surface area. The temperature range was chosen depending on an earlier study by Wang *et al* [63] and Bi *et al* [95] who reported fruitful results for hydrogen production by partial oxidation of ethanol over Pt/ZrO_2 and unsupported Fe-Ni catalysts in the same temperature range. The O_2/ethanol ratio in the range from 0.5 to 2 was varied at 270^{o}C and over a fixed catalyst surface area. The last investigated parameter was the partial oxidation of ethanol as a function of the catalyst surface area under optimum conditions. A comparison between the catalysts was also performed under optimum conditions to show the effect of different iron oxide phases on the hydrogen production. Those optimum conditions found for the unsupported

catalysts were also applied to the supported iron oxide catalysts to study the effect of iron oxide loading on the products distribution. Attention was paid to the effect of the reaction parameter on carbon monoxide production specifically due to the importance of finding an optimum condition for hydrogen rich gas production because the undesirable carbon monoxide oxidises the Pt-catalyst in the fuel cell.

4.2.4. Catalytic activity and selectivity measurement

Major components found in the reaction products were H_2, H_2O, CO, CO_2 and unconverted ethanol. Acetaldehyde (CH_3CHO) was also detected as a by-product. Catalytic activity was evaluated in terms of ethanol conversion. The ethanol conversion ($X_{ethanol}$), the yield (Y_i) and selectivity (S_i) for hydrogen, carbon monoxide and acetaldehyde in the POE reactions [83, 117] were calculated in this study according to the following equations:

$$X_{ethanol}(\%) = \frac{P_{ethanol-in} - P_{ethanol-out}}{P_{ethanol-in}} \quad (6)$$

The reaction products yields are defined as the ratios of any product partial pressure to the consumed moles of ethanol, accounting for stoichiometry as follows:

$$Y_{H_2} = \frac{P_{H_2\text{-out}}}{P_{ethanol\ -in} - P_{ethanol\ -out}}, \quad Y_{CO} = \frac{P_{CO-out}}{P_{ethanol-in} - P_{ethanol-out}} \quad (7, 8)$$

$$Y_{CH_3CHO} = \frac{P_{CH_3CHO\ -out}}{P_{ethanol\ -in} - P_{ethanol\ -out}} \quad (9)$$

The catalysts selectivity towards hydrogen production was calculated as the amount of produced hydrogen in relation to the produced water and hydrogen. The CO selectivity was also calculated as a function of the produced carbon monoxide and carbon dioxide as explained in the following:

$$S_{H_2} = \frac{P_{H_2-out}}{P_{H_2-out} + P_{H_2O-out}}, \quad S_{CO} = \frac{P_{CO\ -out}}{P_{CO\ -out} + P_{CO_2-out}} \quad (10, 11)$$

4.3. Methods for catalyst analysis

After a partial oxidation reaction of 10 hours, the fresh and spent catalysts were characterised using X-ray powder diffraction (XRD) and transmission electron microscopy (TEM) and N_2 adsorption isotherm to determine the BET-surface area (S_{BET}). For particle size calculation and particle size distribution, a scanning electron microscopy (SEM) and dynamic light scattering methods as well as BET were used.

4.3.1. X-ray diffraction (XRD)

The X-ray powder diffraction (XRD) was used to identify the catalyst structure before and after the POX reaction using a Bruker apparatus, model D8. Data for XRD patterns of all catalysts as well as the supports were collected over 12 hours using Cu K_α radiation with a wavelength of 1.5418 Å. For each sample, Bragg angles (2θ geometry) between 20^o and 100^o were scanned. For data interpretation, the EVA software and the database of JCPDS were used.

4.3.2. Scanning electron microscopy (SEM) and energy dispersive X-ray spectroscopy (EDX)

The scanning electron microscope (SEM) tool was used to show the surface morphology and calculate the particle size for the SEM photo. For this purpose, the apparatus Quanta 400 supplied by Philips was used. It was working with continuous acceleration voltage of 200 V to 30 kV. The SEM apparatus which was also equipped with EDX analysis system Genesis 4000 and fully computer-controlled FESEM was used for the chemical composition analysis.

4.3.3. Transmission electron microscopy (TEM)

Transmission electron microscopy (TEM) studies were performed for some samples in co-operation with CENIDE to prove the morphology of prepared samples and also the deposition of iron oxide particles over the SiC support. TEM was carried out on a Philips with GEMINI objective lens that has an acceleration voltage from 30 to 100 kV, equipped with an EDX analysis system operated at 160 kV. The EDX analysis was used to prove the presence of iron oxide and SiC particles on the tested samples. To obtain suitable samples for TEM characterisation, the powders were dispersed in distilled water by dissolving 0.003 g in 10 ml water and then the

suspension was subjected to ultrasonication. The samples were mounted on a micro-grid carbon polymer supported on a copper grid, then a few droplets of the suspension were dripped on it and the whole was dried afterwards.

4.3.4. BET surface area

The BET surface area was measured by physical adsorption of N_2 at 77 K using a NOVA-100 analyser instrument supplied by Quantachrome Corporation. Prior to each measurement, the catalyst was degassed at 423 K for 12 h to remove the adsorbed impurities. BET specific areas were calculated from these isotherms using the BET method [60] and taking a value of 0.162 nm^2 for the cross-section of the physically adsorbed N_2 molecule.

4.3.5. Dynamic light scattering (DLS)

Dynamic light scattering was used as analytical method to determine the prepared particle size [118]. The Brownian motion of the particles was measured by illuminating the particles with a laser beam and detecting the intensity fluctuations in the scattered light. As the particles move around in a solution, the constructive and destructive phase addition of the scattered light will cause the bright and dark areas so that the intensity appears to fluctuate. The rate of intensity fluctuation was then used to calculate the size of the particles. This was done by measuring the correlation between an initial signal at a time t; after a very short time interval ($t+\delta t$) the two signals will be strongly correlated and vice versa after a long time correlation. It is known that large particles move slowly, while smaller particles move accordingly fast. So if large particles are measured, the intensity will also fluctuate slowly and it will be vice versa for the small particles. After measuring of the correlation function this information could be used to calculate the size distribution by application of commercial software algorithms to extract the decay rates for a number of size classes and calculate the size distribution. To measure the prepared particle size using a Zetasizer Nano instrument supplied by Malvern Instruments Ltd., samples were prepared by dissolving a 3 mg sample in 10 ml polyethylene glycol methyl ether and subjected to ultrasonication for 5 minutes to make a stable suspension. The sample was then given in a cell and loaded into the cell area on the top of the instrument. The cell was then subjected to a laser beam to measure the luminescence. The particle size

distribution curve was then taken by the apparatus software. The measurement was repeated 5 times for each sample to insure the reproducibility.

4.3.6. Fourier transform infrared (FTIR)

The FTIR analysis tool was used in order to identify the functional groups and how the atoms were bonded together in the Fe_2O_3/SiC series samples [119]. This was done by the detection of vibrational and streaching bands for iron oxide and SiC. The FTIR spectrum was recorded using Equinox 55 equipment supplied by Bruker co. The analysis was done at atmospheric pressure. Before measuring, 3 mg of the nanoparticle sample were pressed with 0.3 g KBr supplied by Riedel-deHaen company to 10 tone. Then the KBr +sample disc was held vertically and subjected to the IR beam through a hole. The transmittance mode was used to measure the sample.

4.3.7. X-ray photoelectron spectroscopy (XPS)

The XPS analysis was used to study the electronic structure of the supported catalyst surfaces [120, 121]. The photoelectron spectra were recorded using a VG Escalab 200R electron spectrometer equipped with a Al Kα X-ray source (hν= 1486.6 eV) and hemispherical electron analyser operated at pass energy of 44 eV. For analysing, the sample particles (0.03g) were dissolved in 10 ml ethanol and then the sample was put into an ion-pumped analysis chamber which was vacuumed to 1x10-9 mbar during measurement. The C_1'S peak at 284.6 eV was used as a standard for peak position measurement.

CHAPTER 5
CATALYST PREPARATION

5. Catalysts preparation

In this work the CVS method was used to prepare both iron oxide and SiC nanoparticles from ferrocene and TMS precursor. For this purpose, the CVS parameters of the precursor partial concentration, gas mixture velocity and residence time inside the reactor and diluent gas concentration were studied.

5.1. Silicon carbide preparation

Recently, nanoparticles attracted much attention for applied research. The development of production processes to produce it in a high quality in large quantities is the major challenge for the industrial application of nanoparticles. Silicon carbide (SiC) is an outstanding candidate for high-temperature, high-frequency and high-power electronic applications due to its good physical properties such as extreme hardness, high mechanical strength at high pressure, good heat conductivity, chemical resistance and a wide-band gap semi-conducting feature [122]. Ultrafine β-SiC particles are mostly synthesised by chemical vapour deposition (CVD) from compounds containing silicon and carbon [123-126]. Tetramethylsilane is a well known precursor for the production of SiC by CVD [127, 128]. The investigation of SiC for catalytic applications as support is scarce. Leroi et al. [129] investigated SiC as a support for Ni catalyst system for methane oxidation. He found that the support prevented the formation of coke due to the hot spot. In this study SiC was used as a support for the mentioned advantages. In this part the effect of SiC production conditions on its particle size will be discussed.

5.1.1. Influence of deposition temperature on SiC particle size

Several authors [128, 130, 131] reported that SiC starts to deposit at 800^{o}C from a tetramethylsilane precursor. At this temperature only amorphous particles could be produced. In this work the production of SiC from TMS pyrolysis in a decomposition temperature range from 800°C to 1150^{o}C was studied while the other experimental conditions of TMS, i.e. evaporation temperature, nitrogen flow through the bubbler and diluent flow were kept constant at -10^{o}C, 30 and/or 150 sccm. The particle size was measured from SEM images by taking 100 particles and measuring their diameter to determine the particle size distribution. The particle size for such samples was chosen according to the highest count. Figure 9 shows a sample of SEM images of

particles prepared at 800°C and 1150°C. The SEM images were taken at a similar magnification of 100,000 times and image area of 1 μm. As the figure shows the particles become smaller with increasing temperature.

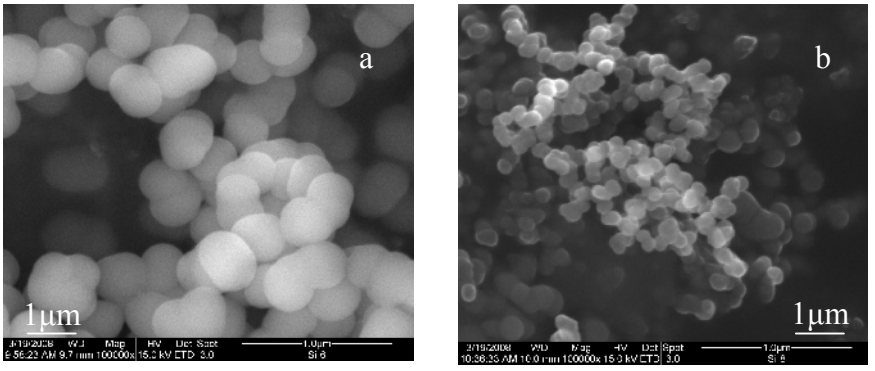

Figure 9: SEM images for the SiC particles prepared at a) 800°C and b) 1150°C

Figure 10 illustrates the effect of the deposition temperature on the prepared SiC particle size. As shown in the figure, the particle size decreases from microscale to nanoscale particles with increasing reaction temperature along the studied temperature range

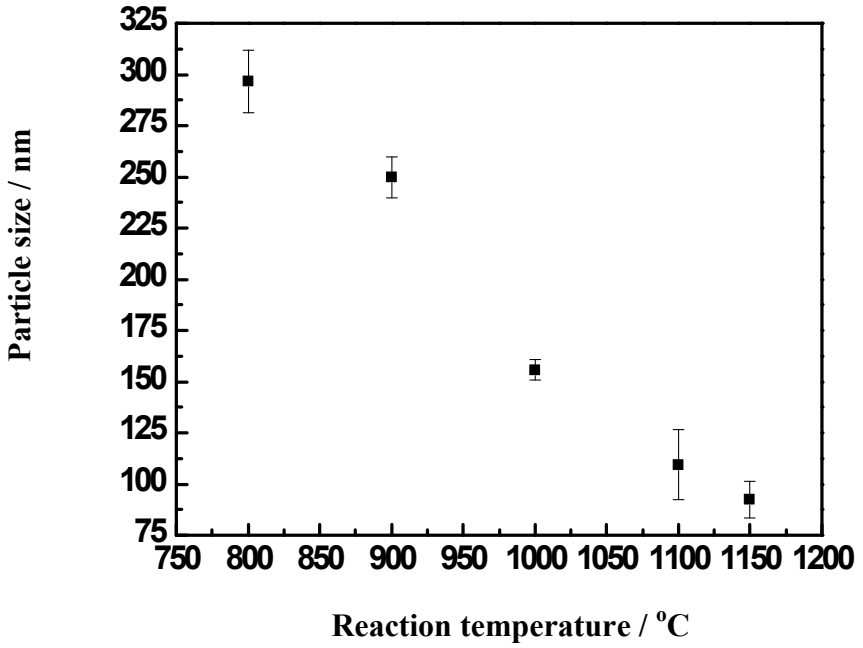

Figure 10: Effect of the temperature on the prepared SiC particle size using TMS precursor at a temperature = -10°C carrier gas flow = 30 sccm, accelerating gas flow = 150 sccm

These observations fit well those results obtained by Wu and Ready [132] and Okabe *et al.* [133]. They reported the same effect for the SiC production at similar reaction conditions. As an explanation for this behaviour it is believed [52, 134] that

using a precursor with a high C:Si ratio, such as TMS for HWCVD, at temperatures lower than 1400^{o}C and atmospheric pressure leads to a polycarbosilane structure with microstructure films, while using monomethylsilane at lower substrate temperatures form an SiC film with a network through the Si atoms. This is due to incomplete precursor dissociation whereas pyrolysis reaction goes through a methyl radical formation pathway. To produce further smaller SiC particle sizes in a range of 10 nm, the TMS concentration was changed. For such a target, the reduction of the carrier gas flow through the bubbler was investigated.

5.1.2. Influence of precursor concentration

In this experiment the effect of precursor concentration on the particle size was studied by changing the N_2 carrier gas flow through the bubbler in a range from 30 to 1.0 standard cubic centimetre per minute (sccm), what led to a change of the precursor mole fraction from $66.6 \cdot 10^{-3}$ to $2.22 \cdot 10^{-3}$, respectively. The experimental conditions are shown in Table 1. The furnace temperature was kept constant at 1100^{o}C for safety reasons since the furnace maximum temperature is 1150^{o}C

Table 1: Experimental conditions of the SiC production with low particle size by changing the carrier gas flow.

Parameters	value
Precursor evaporation temperature	-10^{o}C
Reaction temperature	1100^{o}C
Carrier gas flow	30 - 1 sccm
Precursor mole fraction	$66.6 \cdot 10^{-3}$ - $2.22 \cdot 10^{-3}$
Total gas flow	180 sccm

The particles size measured here also form SEM images in the course of procedures described above (see page 46). Figure 11 shows SEM images for the prepared SiC at a flow of 30 or 1 sccm, respectively.

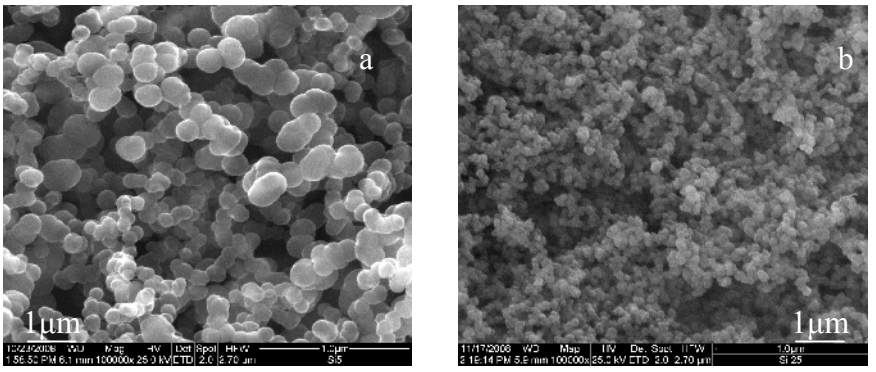

Figure 11: SEM images for the prepared SiC particles at a) $66.6 \cdot 10^{-3}$ and b) $2.22 \cdot 10^{-3}$ precursor mole fractions

The effect of TMS mole fraction variation on the produced particle size is illustrated in Figure 12. The figure indicates that the particle size decreased from 125 to 39 nm for the corresponding concentration range. Further experiments were carried out to investigate the effect of a lower flow up to below 1.0 sccm, but no particles were produced for such conditions. This may be explained by the very low precursor amount in the furnace which may also be deposited on the furnace walls.

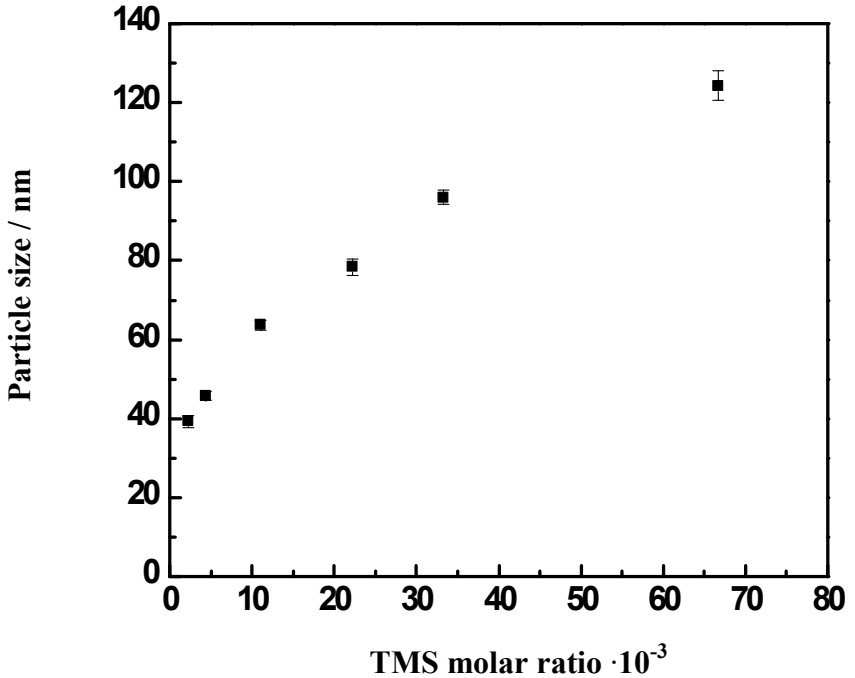

Figure 12: Effect of TMS precursor concentration on the prepared SiC particle size at precursor temperature = -10°C, reaction temperature = 1100°C, total flow = 180 sccm

The tendency of producing smaller particle sizes by decreasing the carrier gas flow was also reported by Wu and Ready [132] and Okabe *et al.* [133]**.** Klein *et al.* [128] studied the formation of SiC from TMS under vacuum conditions, and he

reported the same tendency at low TMS partial pressure and high total gas pressure of 3 kPa. The tendency of producing a smaller particle size at a low carrier gas flow through the bubbler was attributed to that at low partial pressure, a low number and low density grains are formed and therefore a low probability of agglomeration occur. While at higher partial pressures there is a competition between sintering that forms large particles and polymerisation to finally form grains. Also at high partial pressure, the residence time is long enough for the grains fusion inside the particles to form larger grains, thus decreasing the degree of agglomeration at the cost of larger grain sizes. From the above explanations it is obvious that residence time is a quite effective parameter in the chemical vapour synthesis process. So this factor was further studied in the next experiment.

5.1.3. Influence of residence time and gas mixture velocity

In this experimental series both the N_2 carrier gas through the bubbler and the diluent flows were changed together in order to study the residence time and gas mixture velocity inside the reactor.

Table 2: Experimental conditions of the SiC production at a lower particle size by changing the gas mixture velocity and residence time

Parameters	Value
Precursor evaporation temperature	-10^{o}C
Reaction temperature	1100^{o}C
Carrier gas flow	2.78 - 8.34 sccm
TMS mole fraction	$11.11 \cdot 10^{-3}$
Total gas flow	100 – 300 sccm
Gas mixture velocity (m/s)	$2.7 \cdot 10^{-3}$ - $8.13 \cdot 10^{-3}$
Gas mixture residence time (s)	123 - 369

This TMS molar ratio corresponds to the condition of the carrier gas flow through the bubbler of 5 sccm and the total flow of 180. This flow condition was chosen because it was found to produce a sufficient yield in a shorter experimental time that the produced sample can easily be weighed. The particle size for this experimental set was calculated using the same procedures, as shown before. Figure 13 shows the SEM image samples for the SiC particles produced at different gas mixture velocities.

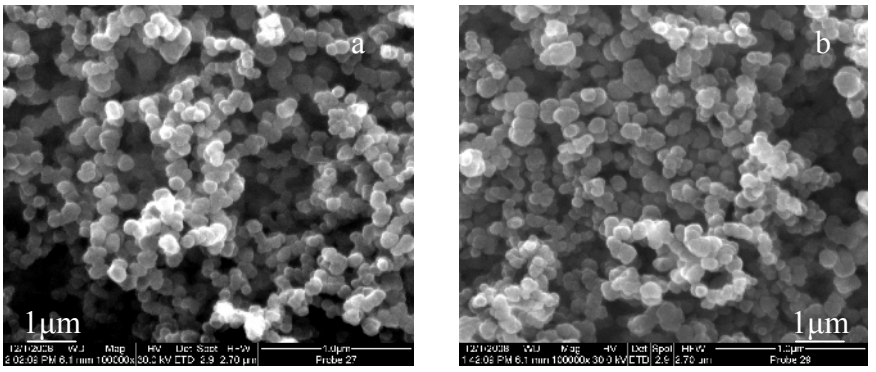

Figure 13: SEM images for the SiC particles produced at a) 8.13 m/s and b) 2.7 m/s gas mixture velocities

Figure 14 shows the particle size and the total weight of the produced particles as a function of gas mixture residence time inside the reactor. It is clear from the curve that the particle size decreases from 70 to 55 nm with increasing residence time. At the same time, the produced sample weight decreased significantly from 0.168 to 0.007 g with increasing the residence time range under investigation. This can also be expressed in terms of gas mixture velocity. Figure 15 shows the change of the gas mixture velocities versus the particle size and sample weight. Here both the particle size and the weight increase with increasing velocity from $2.7 \cdot 10^{-3}$ to $8.13 \cdot 10^{-3}$ m/s. Those observations may be explained by the competitive particles precipitation on the reactor walls at longer residence time and, accordingly, at lower velocities. The particles precipitation inside the reactor was proved by a high increase in the sample weight at a lower residence time. This higher sample weight produced at lower velocities or smaller residence time is due to the fact that the flow pushes the produced particles to the filter and hence much more particles are collected in the filter resulting in a high weight.

The observed increase of the particle size with increasing velocity may be attributed to the fact that the high velocity of the gasses moves the formed particles to the filter where they are accumulated on the filter surface while the particles collected later are in turn accumulated on those accumulated before what leads to an agglomeration. Similar results and explanations were reported by other authors [128, 135, 136] for the investigation of the effect of residence time on the particle size and quantity for alumina and silica by changing the reactor diameter.

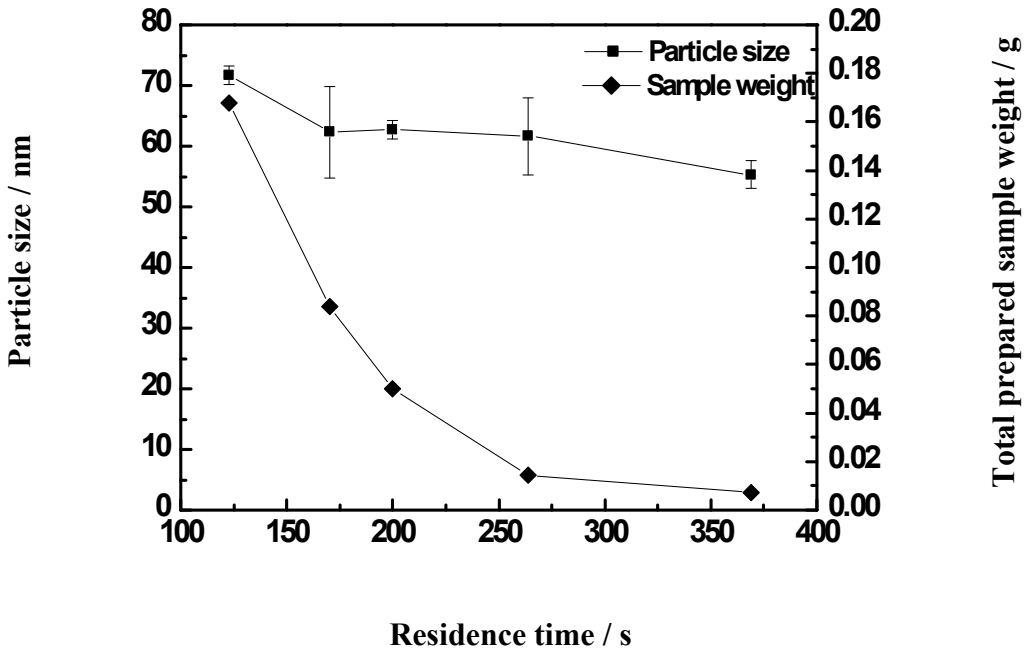

Figure 14: Effect of the gas mixture residence time in the reactor on the prepared quantity of SiC and its particle size at TMS molar ratio = 11,11·10 $^{-3}$, reaction temperature = 1100^{o}C, precursor temperature = -10 ^{o}C, reaction time = 4 hrs

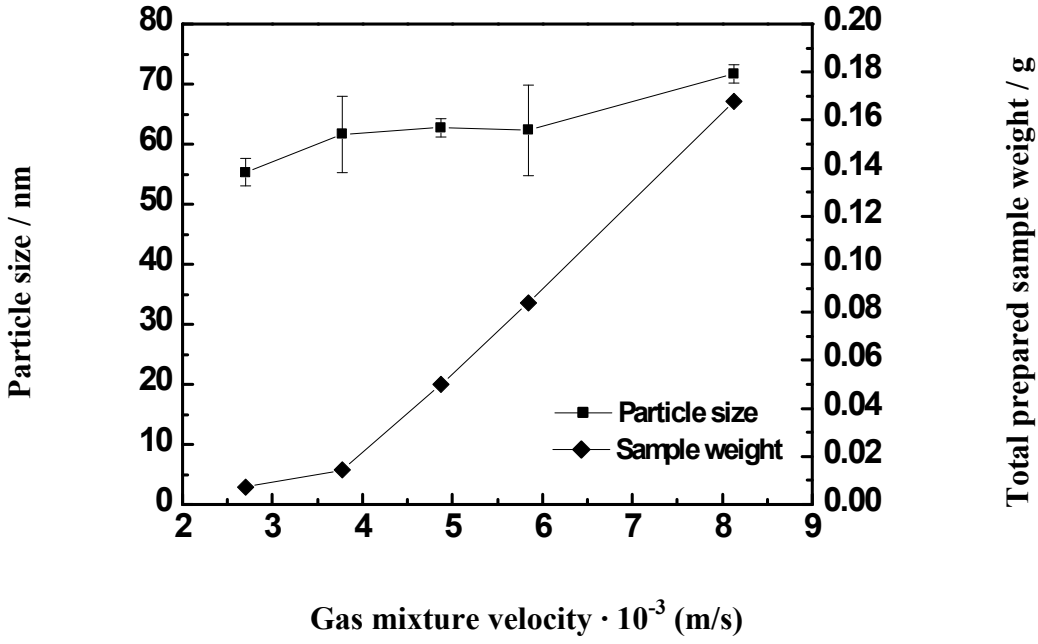

Figure 15: Effect of the gas mixture velocity on the prepared quantity of SiC and its particle size on the condition of TMS molar ratio = 11, 11·10 $^{-3}$, reaction temperature = 1100^{o}C, Precursor temperature = -10^{o}C, reaction time = 4 hrs

5.1.4. Effect of diluent concentration on the particle size

In this experiment the TMS evaporation temperature was kept at -10^{o}C while the total flow changed from 180 to 400 sccm by varying the N_2 diluent flow in a range from 179 to 399 sccm. The experimental conditions are shown in Table 3.

Table 3: Experimental conditions of the SiC production at a lower particle size by varying the gas mixture total flow.

Parameters	Value
Precursor evaporation temperature	-10^{o}C
Reaction temperature	1100^{o}C
Carrier gas flow	1 sccm
Precursor mole fraction	$1.0 \cdot 10^{-3}$- $2.22 \cdot 10^{-3}$
Total gas flow	180 – 400 sccm

In this experiment, the TMS molar ratio changed from $2.22 \cdot 10^{-3}$ to $1.0 \cdot 10^{-3}$ corresponding to a total flow of 180-400 sccm respectively. The particle size for the collected sample was measured from the SEM images as shown earlier. Figure 16 shows SEM sample images for SiC nanoparticles prepared with different precursor concentrations by varying the total flow of the gas mixture.

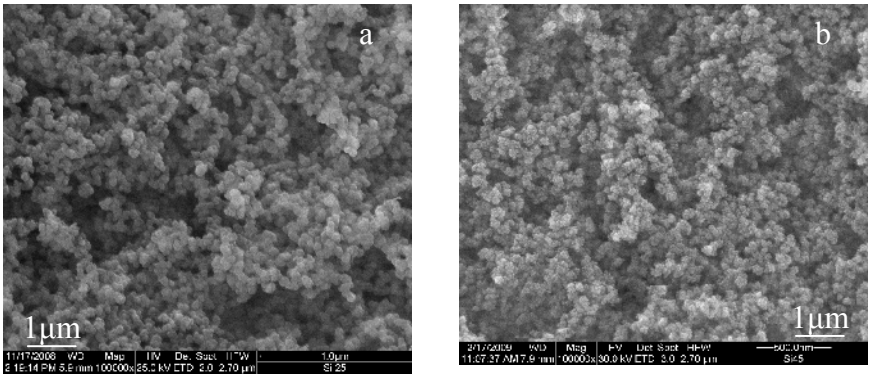

Figure 16: SEM images of the SiC particles prepared at a) $2.22 \cdot 10^{-3}$ and b) $1.0 \cdot 10^{-3}$ precursor molar ratio

Figure 17 shows the change in particle size with further diluting the TMS precursor by increasing the diluent concentration. The particle size decreased strongly in a range from 39 to 5 nm by increasing the diluent gas molar ratio, which the TMS precursor mole fraction decreased within the investigated range. This can be explained as follows: When increasing the diluent gas flow, a low concentration of SiC monomers will be provided to the reactor that prevents the agglomeration of

produced particles. Similar observations were also reported by some other authors [128, 132, 133]. They studied the deposition of SiC from TMS precursor and found the same effect for particle size variation by changing the flow through the bubbler and the total gas mixture flow. From the previous parameter investigations, it could be concluded that the optimum condition for the production of SiC particles at atmospheric pressure was found when the TMS precursor was used at evaporation temperature of -10°C, reaction temperature of 1100°C, N_2 carrier flow through the bubbler of 1.0 sccm and the gas mixture was diluted with 399 sccm N_2 gas as diluent. Under those conditions, SiC with a particle size of 5 nm can be produced. SiC nanoparticles of even smaller sizes can be produced by increasing the gas mixture total flow.

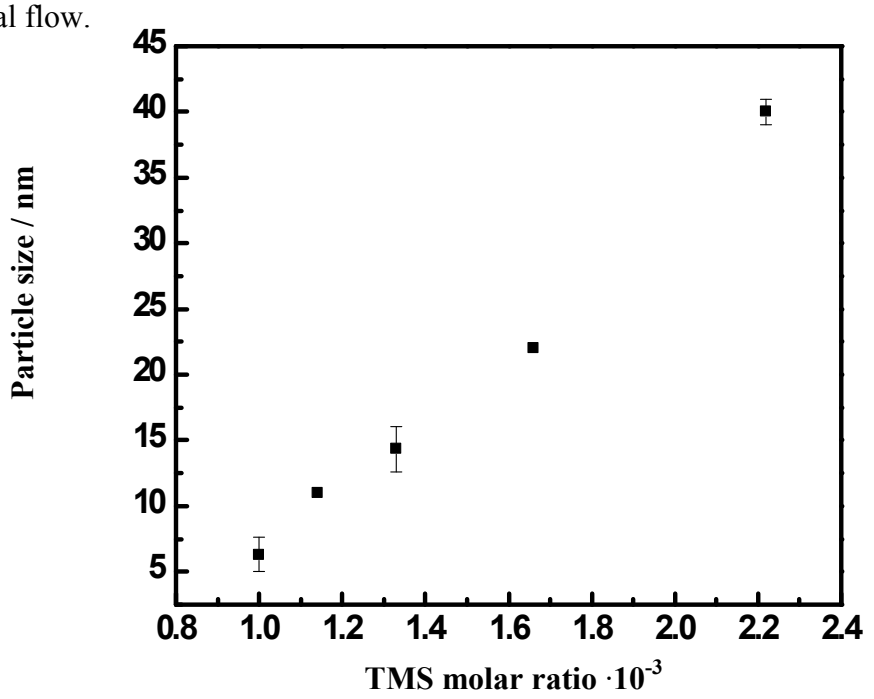

Figure 17: Effect of TMS concentration change by changing the buffer gas flow on the prepared quantity of SiC and its particle size at reaction temperature = 1100°C, N_2 carrier gas flow = 1.0, Precursor temperature = -10°C and reaction time = 4 hrs

5.2. Iron oxide preparation

Due to their hardness, catalytic activity, surface resistivity and their magnetic properties [136], iron oxides attract great interest for various applications in industry, e.g. catalysts, gas sensors, pigments and many others. Recently, extensive researches dealt with the synthesis of involving iron oxide nanoparticles and nanocomposites. It was found that nanosized particles have different properties than bulk materials [137, 138]. The catalyst synthesis method can affect the catalyst properties, including morphology and crystallinity of the produced particles [139, 140]. Currently, there are

several methods employed for iron oxide deposition, including chemical vapour deposition (CVD), sputtering, arc-plasma spray deposition, and various wet chemistry methods such as sol–gel deposition [141-144]. However, there are also disadvantages of these methods that limit their ability to precisely control morphology and chemical composition. The CVD process is considered to be the most common technique for iron oxide thin film deposition [120]. Recently, ferrocene and oxygen have been used successfully to deposit iron oxide films onto Si (100) and anodic aluminum. Deposition at temperatures below 500°C led to the formation of a mixture of hematite and an unidentified phase [140]. In this work ferrocene was used as precursor for chemical vapour deposition of iron oxide at a temperature of 800^{o}C to produce α-Fe_2O_3 nanoparticles. Parameters of precursor evaporation temperature, concentration and oxygen concentration were studied to produce a well defined α-Fe_2O_3 phase with lowest possible particle size.

5.2.1. Effect of precursor evaporation temperature

These experiments were carried out by using ferrocene as a precursor for iron oxide deposition with an N_2 carrier gas flow of 20 sccm, an N_2 diluent flow of 500 sccm and an O_2 flow of 5 sccm at a reaction temperature of 800^{o}C for six hours. The ferrocene evaporation temperature was changed within a range from 70 to 140^{o}C. A low oxygen concentration was used to avoid an Fe_3O_4 formation while it is desired to produce Fe_2O_3 to compare its catalytic activity with the other iron oxide samples as will be discussed later on. The diluent flow was chosen depending on the previous experiments for SiC since 400 sccm were found to be sufficient to produce 5 nm particles so only a slightly higher flow was tested here. Of course, the increase of precursor evaporation temperature will increase its sublimation. This will vary accordingly the precursor partial pressure and hence the precursor mole fraction as well. So it is of interest to calculate the ferrocene partial pressures in the investigated temperature range to calculate its mole fraction. The ferrocene partial pressures in the investigated temperature range were calculated from the Clausius-Clapeyron equation by taking into account the enthalpy of sublimation and the temperature difference. The partial pressure range for ferrocene was found to be $1.46 \cdot 10^{-5}$-$1.1 \cdot 10^{-3}$. The particle size was calculated from the SEM images, as described before. Figure 18 shows the SEM sample images for the prepared iron oxide particles at different precursor evaporation temperatures.

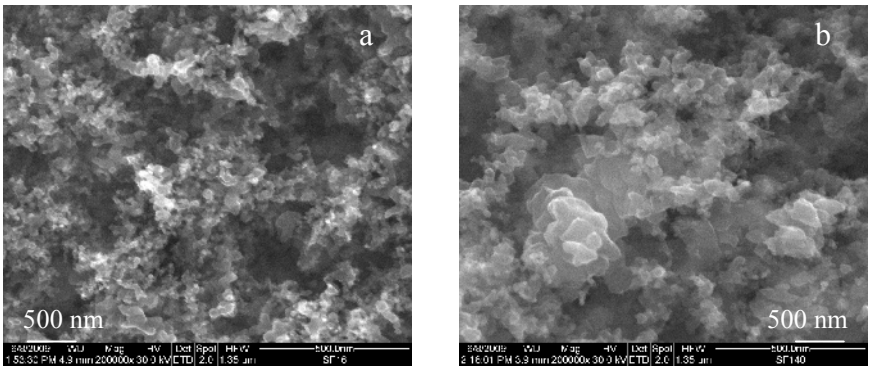

Figure 18: SEM images for the Fe_2O_3 particles prepared at a) 70°C and b) 140°C precursor evaporation temperatures

Figure 19 illustrates the effect of the precursor evaporation temperature on the produced iron oxide particle size. It is clear that iron oxide nanoparticles can be produced within the studied temperature range.

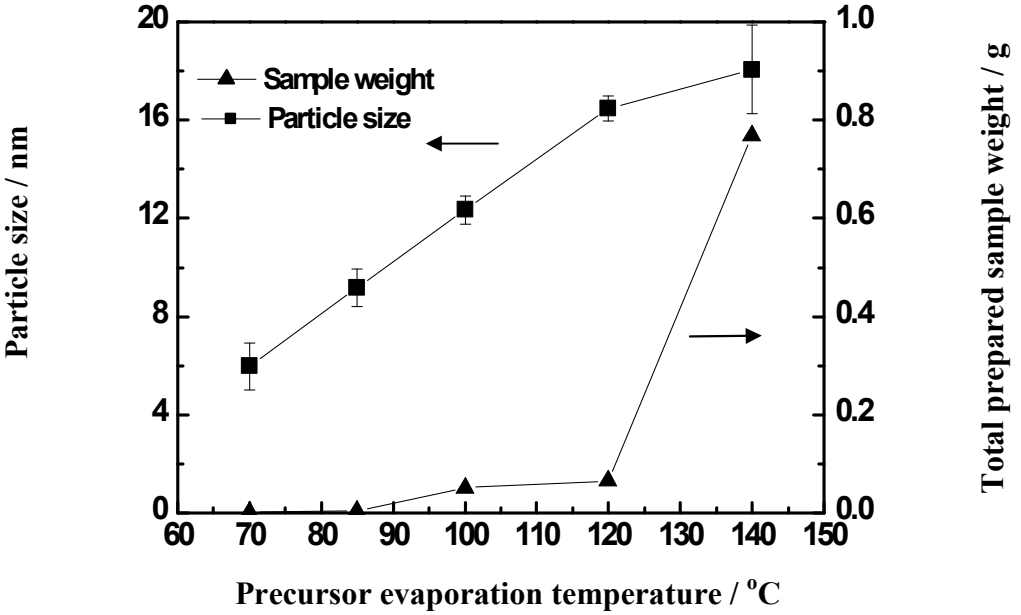

Figure 19: Effect of the ferrocene precursor evaporation temperature on the Fe_2O_3 particle size prepared at reaction temperature = 800°C using N_2 carrier gas flow = 20 sccm and buffer gas flow = 500 sccm, O_2 flow = 5 sccm

The figure shows that the particle size changes from 6 to 19 nm by increasing the evaporation temperature from 70 to 140°C. Siddiqi studied the ferrocene stability using the TG analysis in a range from 70°C to 120°C and reported that ferrocene is stable within this temperature range [114]. The total weight of sample produced is found to increase with increasing evaporation temperature. As shown in Figure 19, a precursor evaporation temperature below 100°C produces an almost negligible total sample weight. This behaviour can be explained by the fact that with increasing

evaporation temperature, the partial pressure of ferrocene vapour increases, hence the iron content in the gas mixture increases and then much more Fe_2O_3 could be produced what enhances the agglomeration leading to a higher particle size. Although a smaller particle size can be produced at an evaporation temperature of 70°C, the temperature of 100°C was chosen to evaporate the precursor for further investigation for the other parameters. This is due to the observation of a very small amount of particles (0.001 g) produced at 70°C while a higher yield can be produced at 100°C meanwhile, the particle size could be mostly in the 10 nm range.

A change in the precursor concentration can be made not only by changing the evaporation temperature but also by changing the carrier gas concentration. So in the next part the effect of the carrier gas mole fraction on the produced particle size will be studied at a precursor evaporation temperature of 100°C.

5.2.2. Effect of the precursor concentration

The influence of the ferrocene molar ratio on the formed particle size was investigated in the range of $5.67 \cdot 10^{-5}$ to $1.98 \cdot 10^{-4}$. The concentration was changed by variation of the N_2 carrier gas flow rate through the bubbler within a range from 10 to 35 sccm while the reaction temperature was kept at 800°C and the total flow was 525 sccm and the oxygen flow was 5 sccm. Figure 20 shows a sample of SEM images of the prepared iron oxide with different precursor concentrations due to variation of the N_2 flow through the bubbler.

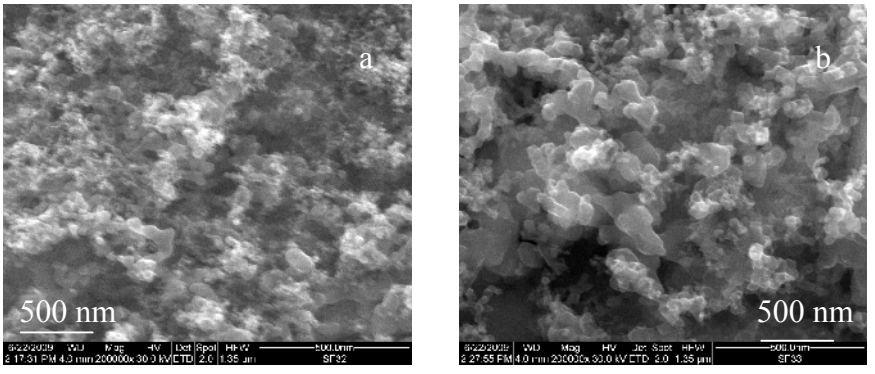

Figure 20: SEM images for the Fe_2O_3 particles prepared at a) $5.67 \cdot 10^{-5}$ and b) $1.98 \cdot 10^{-4}$ precursor molar ratio

The results for the effect of precursor concentration on the particle size are shown in Figure 21. The curve demonstrates that the particle size increases with increasing the flow rate through the bubbler, in a similar way as in the previous case

for β-SiC (see Figure12), simultaneously from 3.6 – 22.8 nm. This can be explained by that at higher carrier gas flow rate a more precursor concentration is transported to the reaction chamber thus, more iron oxide is formed. The higher iron oxide formation at a higher carrier gas flow may result in agglomeration.

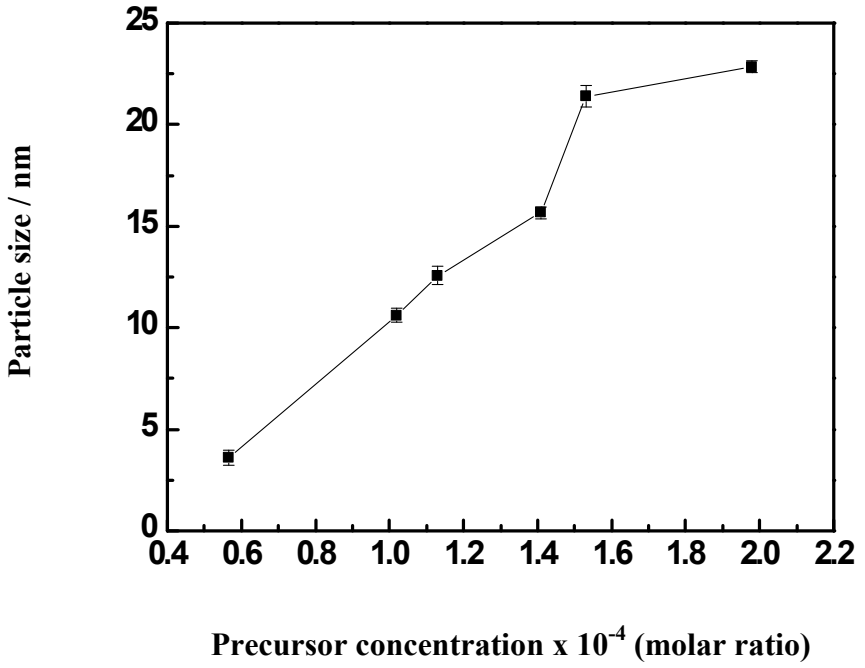

Figure 21: Effect of precursor molar ratio on the Fe_2O_3 particle size prepared at reaction temperature = 800°C and buffer gas flow = 500 sccm, O_2 flow = 5 sccm

5.2.3. Effect of oxygen concentration

In order to make sure that the provided oxygen oxidises all the iron supplied to the reactor into the Fe_2O_3 phase and does not reduce from iron (III) oxide to (II,III) iron oxide due to oxygen or water adsorbed on the reactor surface, the effect of oxygen concentration was studied.

In this experiment the oxygen flow was changed in a range from 5 to 40 sccm. Meanwhile, the precursor evaporation temperature was held constant at -10°C, the carrier gas and diluent flow were kept constant at 20 and/or 525 sccm and the reaction was carried out at a furnace temperature of 800°C.

Figure 22 shows the effect of oxygen concentration on the phase change for the prepared particles investigated using XRD. It is clear that all samples showed the peaks of α-Fe_2O_3 phase. This may be explained by the fact that ferrocene was dosed into the reactor with the aid of N_2 carrier gas due to its low vapour pressure. Therefore, the mass of ferrocene available to react with the fluid bed per unit time was

much smaller than that for oxygen. According to this only the Fe_2O_3 phase was produced.

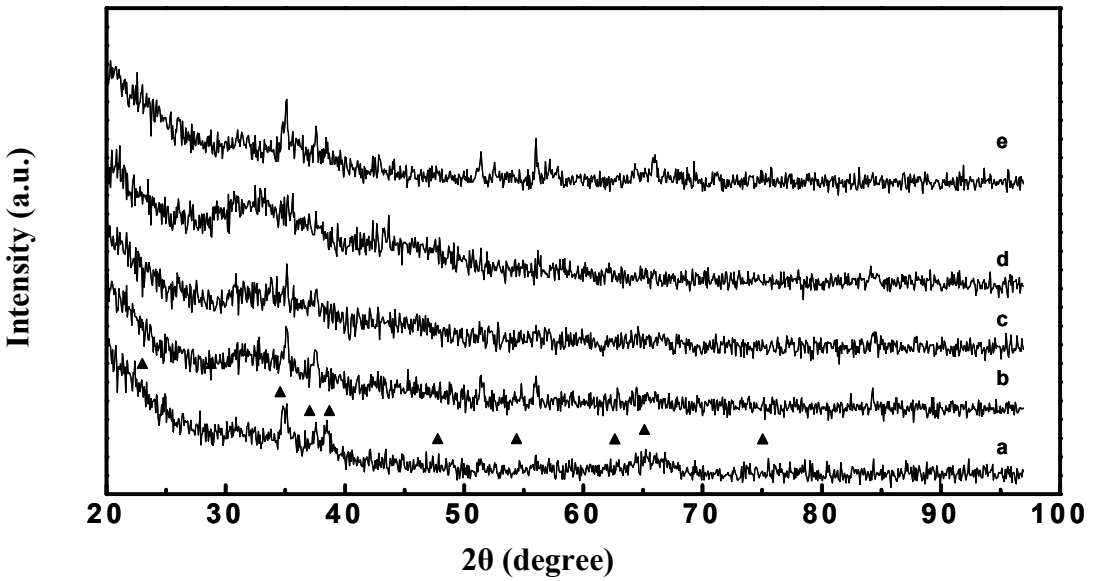

Figure 22: Powder X-ray diffraction patterns of unsupported α-Fe_2O_3 fresh catalyst prepared by CVS at an O_2 flow of a) 5 sccm b) 10 sccm c) 20 sccm d) 30 sccm and e) 40 sccm

Based on the previous results, the condition of supplying ferrocene precursor at an evaporation temperature of 100^{o}C, N_2 carrier gas flow of 20 sccm, diluent gas flow of 500 sccm and oxygen flow of 5 sccm at a reaction temperature of 800^{o}C appears to be the most suitable condition to precipitate iron oxide with 12 nm particles.

5.3. Preparation of α-Fe_2O_3/SiC particles

In this part efforts are reported to prepare α-Fe_2O_3/SiC nanoparticles using the setup discussed in the experimental part through providing the TMS and ferrocene precursors from both sides of the reactor chamber. The furnace temperature was adjusted in two hot zones of 1100^{o}C to produce SiC first; then the particles went to the second hot zone of 800^{o}C to produce iron oxide. For all experiments reported in this part, the optimum conditions found before for the production of SiC were kept constant while various parameters were changed to increase the iron oxide content in the prepared samples. This set of experiments was carried out to produce a series of different iron oxide contents over the SiC particles. For such purpose, the effect of different parameters of the gas mixture inlet tube length inside the reactor, change of the precursor evaporation temperature and finally the carrier gas flow on the iron oxide content of the produced samples were studied.

5.3.1. Effect of the gas mixture inlet tube distance inside the reactor on the iron content

The dependence of the iron content on the gas mixture inlet tube length inside the reactor in a range from 2 to 14 cm was firstly studied. The experiments were carried out at the previously found optimum conditions for the pure SiC and Fe_2O_3 production, while the inlet tube position inside the reactor was changed in a separate experiment. The chemical composition regarding the iron content was investigated using the EDX analysis. Figure 23 shows the EDX spectrum of the prepared samples at an inlet tube distance from the furnace beginning of 5 and 10 cm.

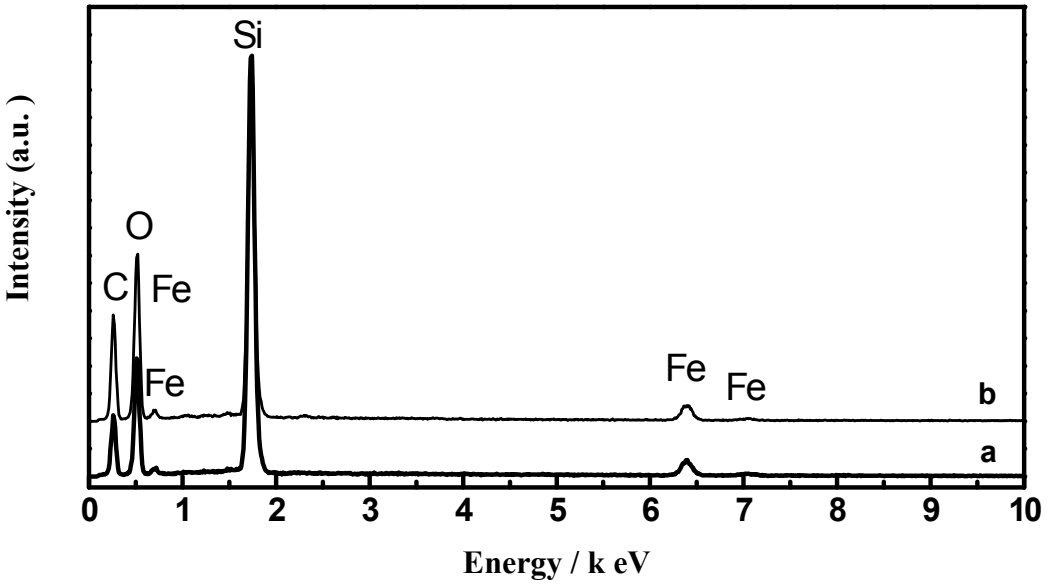

Figure 23: EDX spectrum of the prepared Fe_2O_3/SiC particles by introduced inlet tube for a) 5 cm and b) 10 cm distances inside the furnace

The samples particle size was measured by DLS and found that it varied from 8.3 to 10 nm. This particle size was confirmed by the particle size calculations from BET measurements to be within a range from 5.2 to 10.2 nm. Figure 24 illustrates the effect of the inlet tube distance inside the reactor on the iron content for the prepared sample. It is seen that the iron content increases with increasing the distance of the inlet tube length up to 10 cm and then decreases significantly at the long distance. These results may be because of that at a smaller tube length the precursor does not reach enough the reaction chamber hot zone, because it is near to the exhaust, and the flow from the other side helps to push it away from the furnace. As a result, only few of it goes to the reactor and consequently lower iron content is produced. At a smaller tube length most of the precursor can reach the hot zone and react to produce high

iron content. At distances longer than 10 cm, the line providing the precursor becomes hotter and may reach the temperature of iron oxide deposition so that the particle is deposited inside the tube thus supplying less iron to the reactor and producing samples with lower iron content. This explanation is supported by the observing iron oxide in the exhaust tube at a lower inlet distance and blocking of the tube with iron oxide at a tube distance larger than 10 cm.

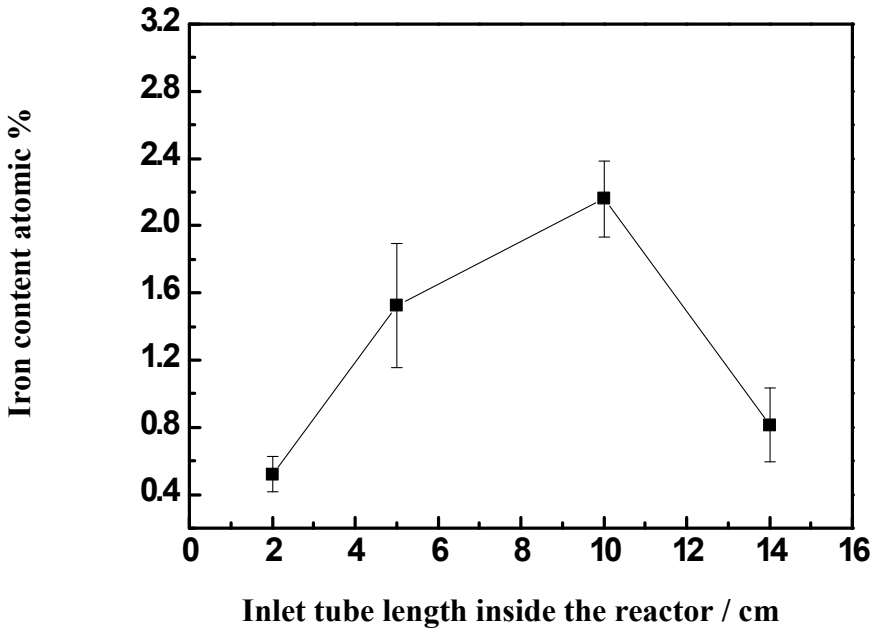

Figure 24: Iron content as a function of inlet tube distance inside the furnace at precursor temperature = 100°C, reaction temperature = 800°C, carrier flow = 20 sccm, buffer gas flow = 500 sccm and O_2 flow = 5 sccm

Figure 24 also shows that the iron content on those conditions is reproducible with some alteration for the sample with 5 cm distance what may be due to experimental error.

Based on this experiment, the iron content of the sample can be controlled by changing the precursor inlet tube length inside the reactor. The tube length of 5 cm inside the reactor was chosen as the best place to produce the iron oxide since it produces considerable iron content with low particle size sample. The particles prepared on optimum conditions and with inlet tube lengths of 5 and 10 cm were chosen as the first two samples in the supported Fe_2O_3/SiC series to test its catalytic activity towards ethanol oxidation. Those samples represent the first two catalysts with low iron content and low particle size samples.

5.3.2. Effect of precursor evaporation temperature on iron content

In these experiments the effect of the ferrocene precursor evaporation temperature on the iron content of the prepared sample was studied. For this purpose, the precursor evaporation temperature was varied in the range from 100 ^{o}C to 120 ^{o}C while the preparation parameters were kept constant at 800 ^{o}C, total flow at 525 and the gas mixture inlet tube with 5 cm inside the reactor. The precursor evaporation temperature was varied in such a way that the precursor mole fraction was varied within a range from $1.13 \cdot 10^{-4}$ to $3.7 \cdot 10^{-4}$. Then the prepared particles were analysed using EDX to determine the iron content. Figure 25 shows the EDX spectrum for the prepared particles at ferrocene evaporation temperatures of 100^{o}C and 120^{o}C.

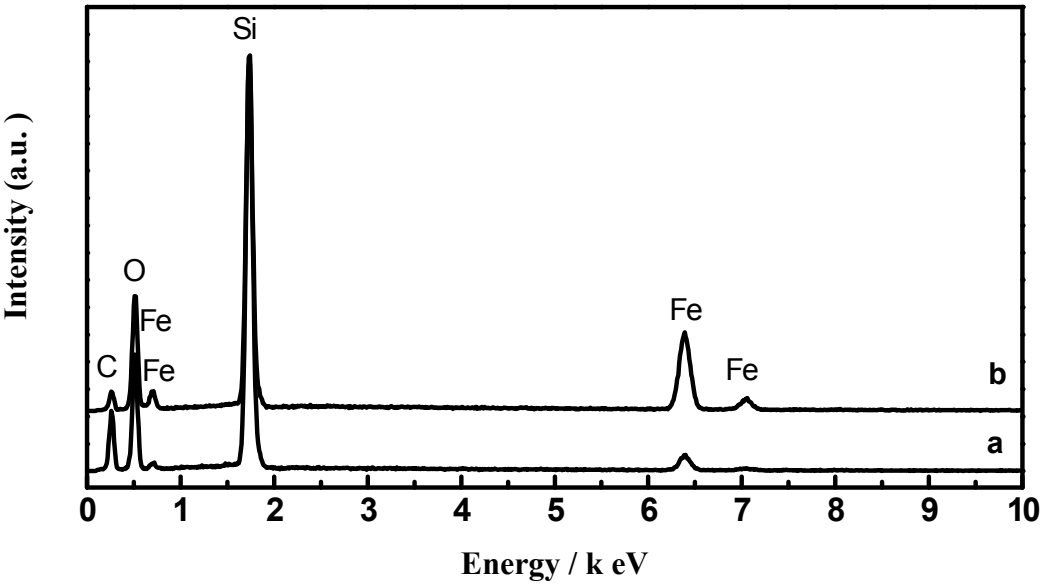

Figure 25: EDX spectrum of the prepared Fe_2O_3/SiC samples at a) 100 ^{o}C and b) 120 ^{o}C

The dynamic light scattering technique (DLS) was used to determine the particle size of the prepared samples. The particle size for such samples was varied from 9.3 nm to 12.9 nm. The particle sizes were also determined from the BET measurements and were found to be within a range from 5.3 nm to 14.5 nm. Figure 26 shows the iron content variation with mole fraction change. The iron content was found to be increased with increasing the evaporation temperature. This may be attributed to the fact that at higher evaporation temperature, higher precursor sublimation, the precursor partial pressure increased so that a higher precursor mass was transferred to the reactor. This increase provided more monomer to the reactor chamber which caused the higher iron oxide quantity deposition. The studied temperature range was

chosen depending on the previous experiments for testing different precursor temperatures (see page 54) to produce a sufficient yield with less difference in particle size. The evaporation temperature of 140°C was not tested here to avoid the possibility of precursor decomposition.

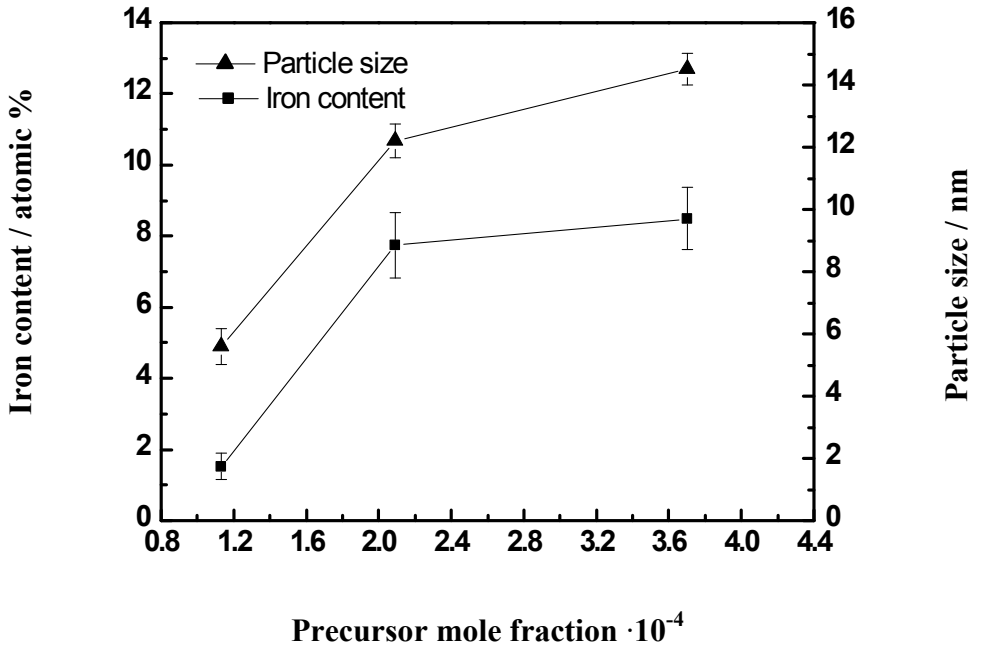

Figure 26: Iron content as a function of the precursor mole fraction variation due to the precursor evaporation temperature change at conditions of nozzle distance = 5 cm, reaction temperature = 800 °C, carrier flow = 20 sccm, buffer gas flow = 500 sccm and O_2 flow = 5 sccm

The samples prepared at evaporation temperatures of 110°C and 120°C were chosen to be medium iron content samples in the supported particles series to test its catalytic activity towards ethanol oxidation. The particle size for these samples was measured from the BET measurements. The particle size for these samples was 12.2 and 14.5 nm, respectively.

5.3.3. Effect of precursor mole fraction on iron content

The ferrocene precursor concentration was the last studied factor to increase the iron content in the prepared supported particles series. The experiments were carried out by changing the flow through the bubbler within a range from 20 to 40 sccm. The other preparation conditions were kept constant at a precursor evaporation temperature of 120°C, a reaction temperature of 800°C, a diluent flow of 500 sccm, an oxygen flow of 5 sccm and an inlet tube of 5 cm inside the reactor.

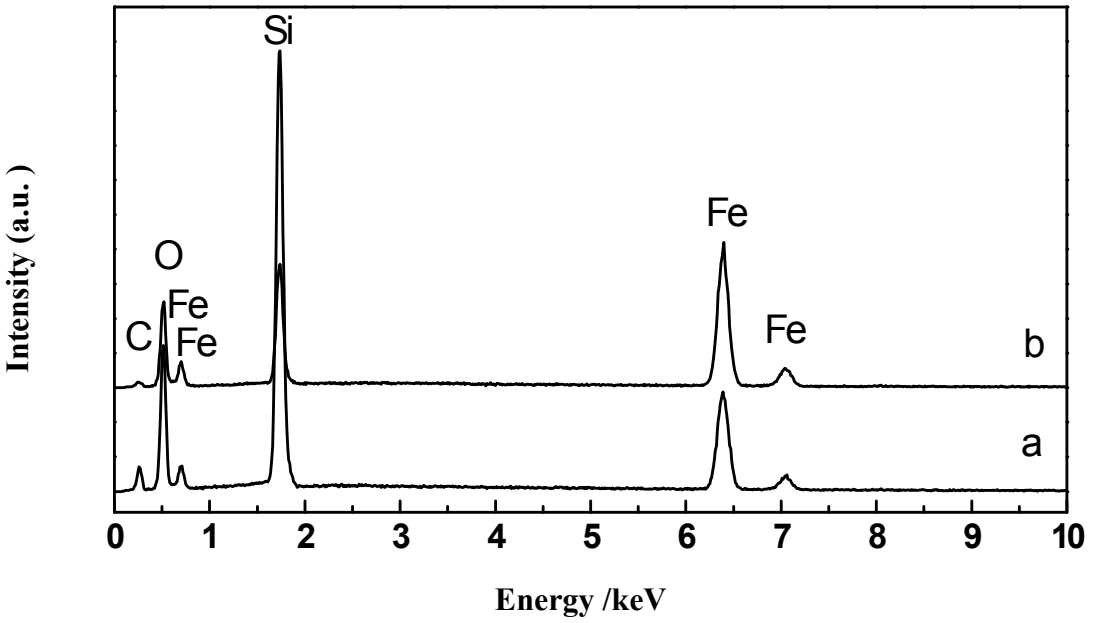

Figure 27: EDX spectrum of Fe_2O_3/SiC particles prepared using carrier gas flow of a) 20 sccm and b) 40 sccm

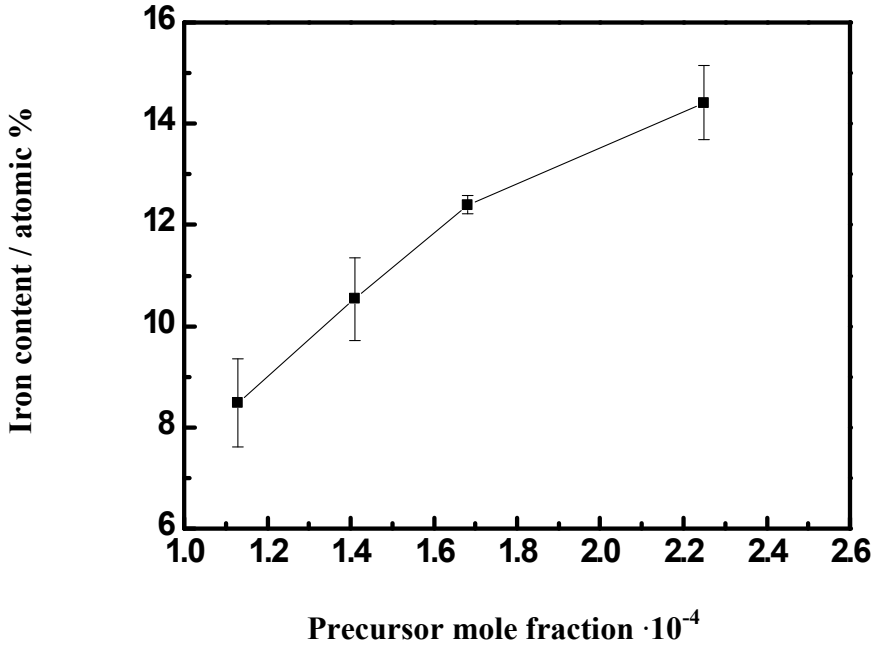

Figure 28: Effect of precursor molar ratio on the iron content of the prepared Fe_2O_3 at evaporation temperature = 120°C, reaction temperature = 800°C, buffer gas flow = 500 sccm and O_2 flow = 5 sccm

The prepared samples were analysed using the EDX technique to identify the iron content. Figure 27 shows an EDX sample analysis of the prepared particles at a carrier flow of 20 and 40 sccm, respectively.

The particle size was determined using the DLS technique. The results showed a small particle size variation within a range from 12.8 to 15 nm. These results were also confirmed by the particle size measurements based on the BET method. Figure 28 shows the change in iron content corresponding to the increase in the carrier gas flow or in other words by increasing the precursor mole fraction.

As the figure shows, the iron content increases linearly within a range of 8.5 to 14.5 with increasing precursor mole fraction from $1.13 \cdot 10^{-4}$ to $2.25 \cdot 10^{-4}$. This is due to the continuous saturation of the N_2 carrier gas with increasing its flow through the bubbler. As a result more precursor molecules are transferred to the reaction chamber and increase the iron content. The highest iron content of 13.4% was assigned to the experiment where the carrier gas flow of 40 sccm was used, so it is chosen to represent the high iron content member in the catalysts series.

The comparison between Figures 24, 26 and 28 shows that a change of the ferrocene molar ratio (Figure 28) is the greatest factor that influences the iron mass content of the prepared particles. In contrary, the change was not nearly as significant for both factors of change in the ferrocene evaporation temperature and the inlet tube length inside the reactor. This indicates that the flow of N_2 carrier gas is the main factor that affects the much higher precursor mass transfer to the reactor chamber by significantly loading precursor vapour at suitable sublimation temperature and, as a result, produces more iron content in the prepared sample. The XRD analysis showed that the formed iron oxide during the course of the previous experiments was in α-Fe_2O_3 (hematite phase) as will be discussed later in the next chapter.

In conclusion this series of samples was chosen to investigate the catalytic activity as a function of the iron content while maintaining the formation of a large sample quantity with small particle size. Based on the results in Figures 24, 26 and 28, samples with 5 and 10 cm long inlet tubes, prepared at evaporation temperatures of 100^{o}C, 110°C and 120^{o}C and samples prepared using carrier gas flow of 40 at 120^{o}C were chosen to prepare the desired sample series catalysts.

CHAPTER 6
CATALYTIC ACTIVITY

6. Catalytic activity

Hydrogen is considered a promising candidate as a future clean energy carrier. It can be obtained from renewable sources (like water or biomass) through thermal or catalytic processes utilizing a diverse set of domestic resources in this way. The use of renewable hydrogen will reduce the energy dependence on fossil fuels, cut greenhouse gas emissions and provide for a sustainable energy supply [40, 145, 146]. Bioethanol produced by fermentation of biomass is considered as a promising feedstock for the sustainable production of hydrogen for fuelling polymer electrolyte fuel cells. Hydrogen can be produced directly from ethanol using several technologies. Among those processes, catalytic ethanol partial oxidation is quite promising [29]. The development of suitable catalysts for this reaction is one of the technical barriers to be overcome for cost-effective fuel processing [85], especially in small fuel cell systems. Many studies have been performed on supported metal oxides particularly for industrial applications [147, 148]; however, the origin of their high activity has not been fully ascertained to date. Among these metal oxides, metal or metal oxide supported iron oxides play wonderfully as catalyst for hydrogen production and organic oxidation reactions [63, 149-151]. In this study ethanol partial oxidation using pure oxygen as oxidant was investigated over different phases of unsupported and supported silicon carbide nanoscale iron oxide catalysts. Catalytic activity for bulk α-Fe_2O_3 was also investigated to be compared with the nanoscale iron oxide. Unsupported Fe_2O_3 with phases of γ, α /γ - and α- Fe_2O_3 were tested as catalysts for the partial oxidation process to investigate their catalytic activity, selectivity in order to optimise the condition to produce the highest possible quantity of hydrogen gas. Deactivation behaviour during the process was also studied for 10 hours time on stream. α-Fe_2O_3 supported silicon carbide particles were tested to understand the effect of support on the reaction products and activity on the one hand, and to investigate the catalyst deactivation and thermal stability on the other hand.

6.1. Ethanol oxidation pre-experiment results

In this study a quadruple mass spectrometer (QMS) was used to identify and follow the time evolution of reactants, products molecules and the masses of the characteristic fragments from them. Firstly, the most abundant fragment ion peaks, the so-called basic peaks, in the mass spectrum were detected for each component in

order to deal with the raw data came out of QMS. The basic peak for each component was detected by measuring the spectra of the pure substances and selection of the highest peak intensity for a specific mass as a characteristic peak for such component. Figure 29 shows the spectrum of 10 % ethanol in a helium solution at a total pressure of 600 mbar. This pressure was chosen because ethanol had a partial pressure of 60 mbar at 25°C [152] so that the total pressure fulfilled the 10% ethanol vapour in the given helium solution at this temperature. It may be recognised that the fragments from ethanol were 14, 15, 17, 29, 31, 45 and 46 mass units corresponding to the fragmentations of CH_2^+, CH_3^+, OH^+, $CH_3CH_2^+$, $CH_3CH_2O^+$ and unfragmented ethanol molecule $CH_3CH_2OH^+$, respectively. Those fragment intensities were identified for ethanol and the values were stated to be constant for half an hour.

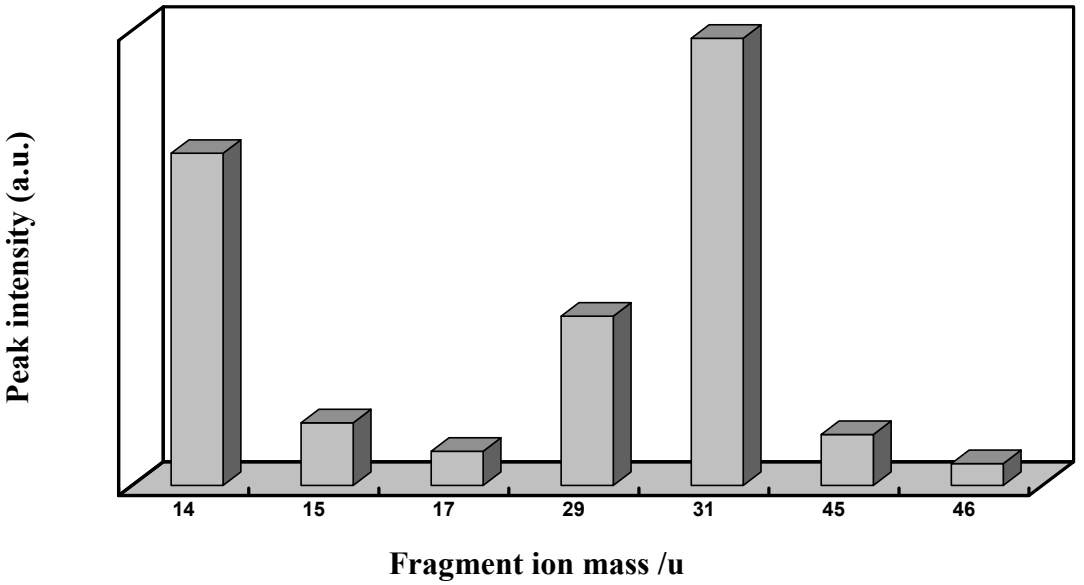

Figure 29: Mass spectrum for a 10% ethanol helium mixture at ambient temperature, total pressure = 600 mbar and actual flow = 500 sccm

As the figure shows, the fragment mass of 31 u is the highest peak intensity for pure ethanol. Therefore, it was chosen to detect and follow the time evolution for ethanol. The same procedures were used for all of the other components of the reactants and prospected products to determine their basic peaks. Table 4 shows the masses chosen for the reactants and products according to the discussed procedure to follow the compounds partial pressure during the ethanol partial oxidation reaction. The figure also shows the prospected fragments and which molecules correspond to the chosen masses.

Table 4: Basic peaks chosen for the reactant and products of ethanol partial oxidation

Compound	Structure	Basic peak	Fragment
Hydrogen	H_2	2	H_2
Helium	He	4	He
Oxygen	O_2	16	O
Water	H_2O	18	H_2O
Carbon monoxide	CO	28	CO
Acetaldehyde	CH_3CHO	29	CHO
Ethanol	C_2H_5OH	31	CH_2OH
Carbon dioxide	CO_2	44	CO_2

For the partial oxidation reaction experiment, it is easier and clearer to express the components in partial pressure instead of its basic peak intensity. For this purpose, a calibration curve for each component was measured in order to calculate the partial pressure of the components from its measured basic peak intensity. This calibration curve was measured for different mixtures of each substance at different partial pressures, which were mixed with helium, and then the corresponding peak intensity was recorded using the QMS method. Then these peak intensities were correlated to the helium peak intensity as a reference inert gas.

Figure 30 illustrate the calibration curve for 10 % ethanol vapour in helium solution. The obtained ethanol peak intensity was normalised to the helium peak intensity. From this curve, the ethanol peak intensity can be directly converted into the corresponding partial pressure using the slope of the straight line.

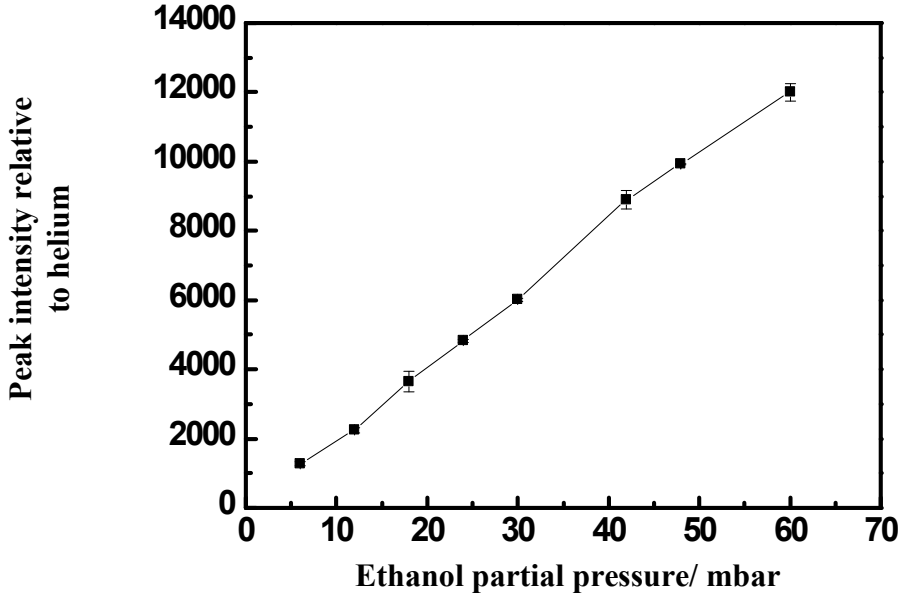

Figure 30: Ethanol peak intensity relative to helium as a function of its partial pressure at ambient temperature and a total pressure of 600 mbar

The same procedures were again used for the other expected components to determine the partial pressure from its measured peak intensity. Using the slope of the straight line in Figure 30, the measured ethanol basic peak intensity during the experimental run can be converted to the corresponding partial pressure.

Figure 31 shows a typical kinetic experimental run for gas phase ethanol partial oxidation using oxygen over the γ-Fe_2O_3 nanoparticle catalyst surface produced by Orthner and Roth. The figure shows the time evolution for the partial pressure of reactants and products during the reaction of ethanol of 60 mbar with oxygen of 60 mbar at 270°C over γ-Fe_2O_3 with 24 m^2 area for one hour.

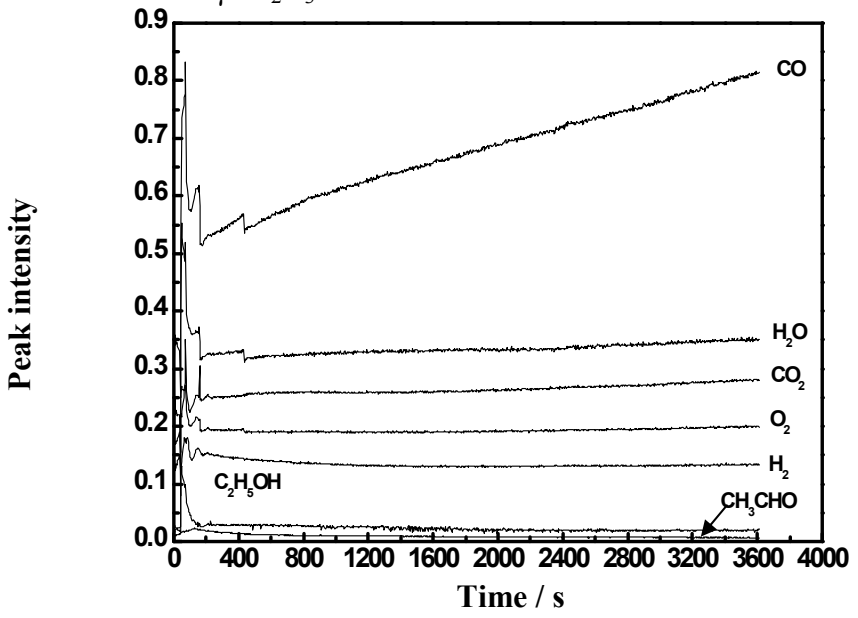

Figure 31: Reaction components peak intensities relative to helium as a function of reaction time for the γ-Fe_2O_3 catalyst at a temperature = 270°C, O_2/ethanol = 1.0, catalyst area = 24 m^2 and a total pressure of 600 mbar

The knowledge of the slope of calibration curve for each component, as shown in Figure 18, was used for the conversion of the peak intensities to the corresponding partial pressures and the row data for the relation between the components partial pressures and time evolution as shown in Figure 19. The components partial pressure was then used to calculate the catalyst activity and selectivities towards ethanol oxidation and the produced component, respectively, after one hour of reaction.

Figure 32 shows the components partial pressure formed during the ethanol partial oxidation as a function of the reaction time. The figure shows that hydrogen and carbon dioxide were the main products of the ethanol partial oxidation over γ-Fe_2O_3 catalyst besides other products like water, carbon monoxide and acetaldehyde

which were also produced at lower partial pressures when applying an O_2/ethanol ratio of 1:1 and a reaction temperature of 270°C. Moreover, for the ethanol and oxygen consumption and the hydrogen and carbon dioxide partial pressures, the main reaction that takes place could be described as follows:

$$C_2H_5OH + 1.5\,O_2 \longrightarrow 3\,H_2 + 2\,CO_2 \qquad \Delta H^{\circ}_{298} = -557 \text{ kJ / mol}^{-1}$$

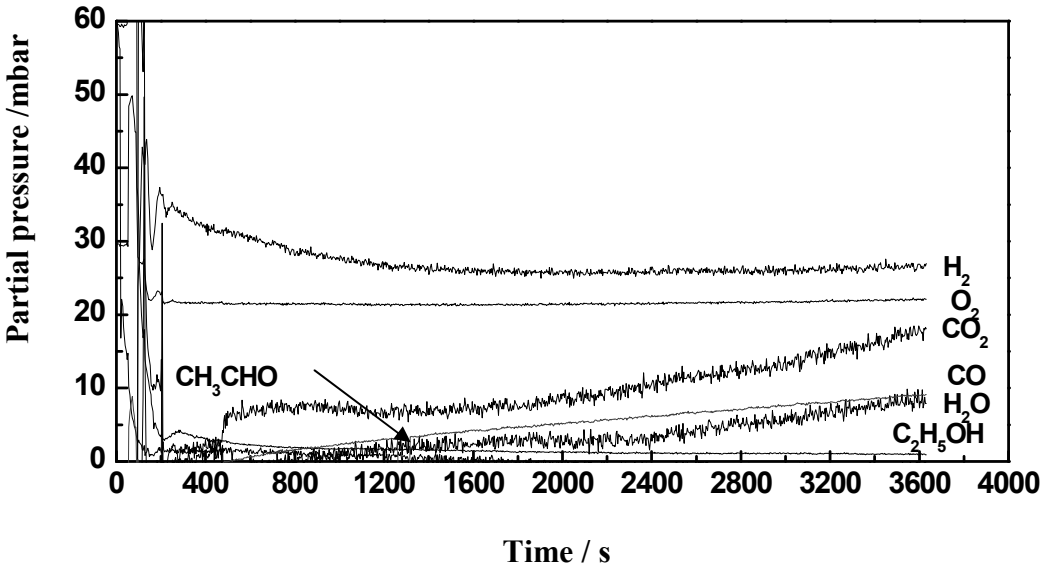

Figure 32: Components partial pressure relative to helium as a function of the reaction time for the γ-Fe_2O_3 catalyst at a temperature = 270°C, O_2/ethanol = 1.0, a surface area = 24 m^2/g and a total pressure of 600 mbar

The chemical equation shows that the reaction is exothermic with 557 kJ mol^{-1} enthalpy of formation accordingly, the reaction needs less energy to be started up what give the POX process the advantage of energy saving. Another observation from Figure 19 is that the reaction was almost completely finished after 6 minutes. Furthermore, not all the oxygen was consumed whereas 20 mbar remained in the reaction chamber in most of the experiments carried out later.

6.2. Unsupported catalysts

In this part, the unsupported bulk Fe_2O_3 (material in microscale) supplied by ABCR GmbH and the nanoscale Fe_2O_3 samples prepared by means of the CVS technique were tested as catalysts for ethanol partial oxidation using oxygen as an oxidant. The reaction parameters of temperature, oxygen to ethanol ratio, surface area and reaction time on stream were varied to optimise the reaction condition in order to produce hydrogen rich gas. The nanoscale Fe_2O_3 in γ-phase and α/γ mixed phases was prepared and supplied by Orthner and Roth [108] while nanoscale α-Fe_2O_3 was home

made using the CVS method. These different phases were used to investigate the effect of the phase on the process activity, selectivity and the effect of the process conditions on the catalyst stability and its physical and chemical properties. Iron oxide was investigated here as a catalyst for ethanol partial oxidation reaction because it is a cheap and environmentally friendly material. Moreover, research on it for POX is scarce. Shi *et al*. [64] shows that nanoscale Fe_2O_3 is an active catalyst to oxidise the benzyl alcohol to benzaldehyde and for other higher aromatic alcohols to corresponding aldehydes and ketones using hydrogen peroxide as oxidant. Chang *et al.* [104] also reported that a noble metal supported Fe_2O_3 nanomaterial catalyst is a complete reactive and stable catalyst for the hydrogen production by methanol partial oxidation. Chang *et al.* also reported that the bulk Fe_2O_3 is an inactive catalyst to produce hydrogen from methanol partial oxidation while it only produces high concentrations of methane gas. Depending on this previous knowledge, bulk Fe_2O_3 and also a different phase of nanoscale Fe_2O_3 were tested later on as catalyst to produce hydrogen from ethanol partial oxidation.

6.2.1. Bulk Fe_2O_3 catalyst

The catalyst sample was first characterised before its catalytic activity was tested using the XRD, SEM and BET surface area measurements. The XRD pattern for the bulk α-Fe_2O_3 without calcination is shown in Figure 33. XRD shows a sharp pattern with high intensity at 2θ of 33.1^o and 35.6^o corresponding to the hematite (α-phase) structure. The sharp peaks indicate the well crystalline structure of the sample.

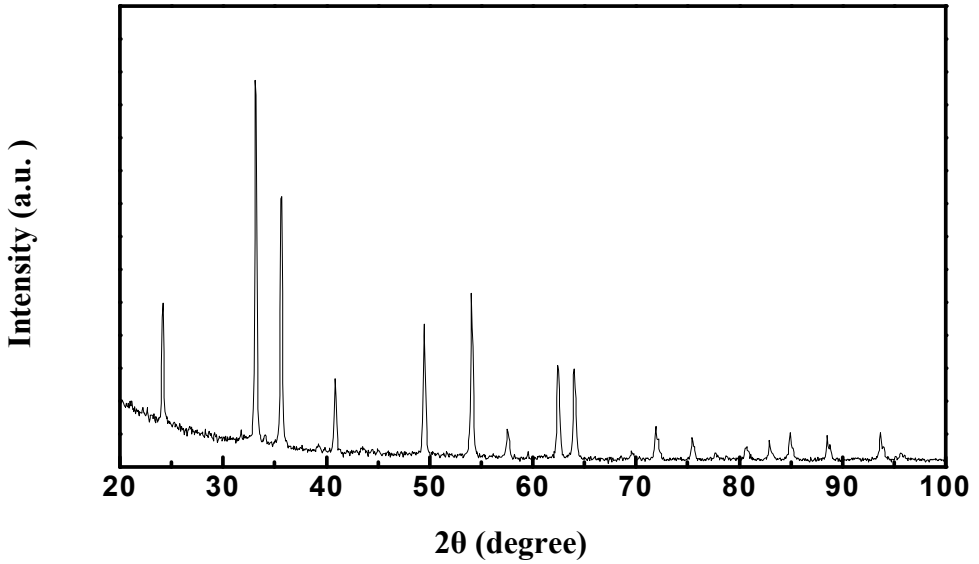

Figure 33: Powder X-ray diffraction pattern of a fresh bulk α-Fe_2O_3 catalyst

The SEM was used to determine the morphology and particle size for the bulk iron oxide. Figure 34 shows the SEM image and particle size distribution for bulk α-Fe_2O_3. The particle size of this sample was 123 nm. The SEM image shows a wide range of particle size distribution in a range from 114 to 134 nm.

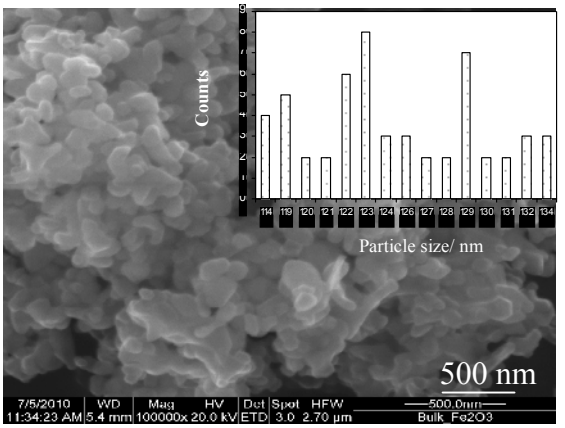

Figure 34: SEM for bulk α-Fe_2O_3 particles. The insert show the particle size distribution

The EDX analysis shows that the sample contains iron, oxygen and carbon elements with 25%, 49% and 25% atomic percent, respectively. The N_2 adsorption isotherm for bulk the α-Fe_2O_3 sample was recorded to determine the sample surface area (S_{BET}) by means of the BET technique. The surface area (S_{BET}) of the sample was 10 m^2/g.

Figure 35 shows the unsupported bulk hematite catalytic activity towards the ethanol partial oxidation and product selectivity within a temperature range from 240 to 280^oC for O_2/ethanol of 0.5, a catalyst area of 1m^2 and a reaction time of one hour. The figure indicates that even at the highest temperature, the bulk α-Fe_2O_3 shows a low ethanol conversion of at last 61.6% at 280^oC. It may be due to a low surface area that the catalyst had a low activity towards ethanol partial oxidation. Meanwhile, with increasing the reaction temperature, the catalyst showed a low acetaldehyde yield of 20% at 220^oC; then it disappeared completely at higher temperatures. In contrast, the carbondioxide yield was found to have increased with temperature. The water yield was found slightly decreased with temperature. Within the temperature range, hydrogen was not detected. This may be explained by the fact that ethanol initially partially oxidised to acetaldehyde because of the low energy supplied for the reaction at low temperature, while at higher temperature acetaldehyde was re-adsorbed and further oxidised to water and carbon dioxide.

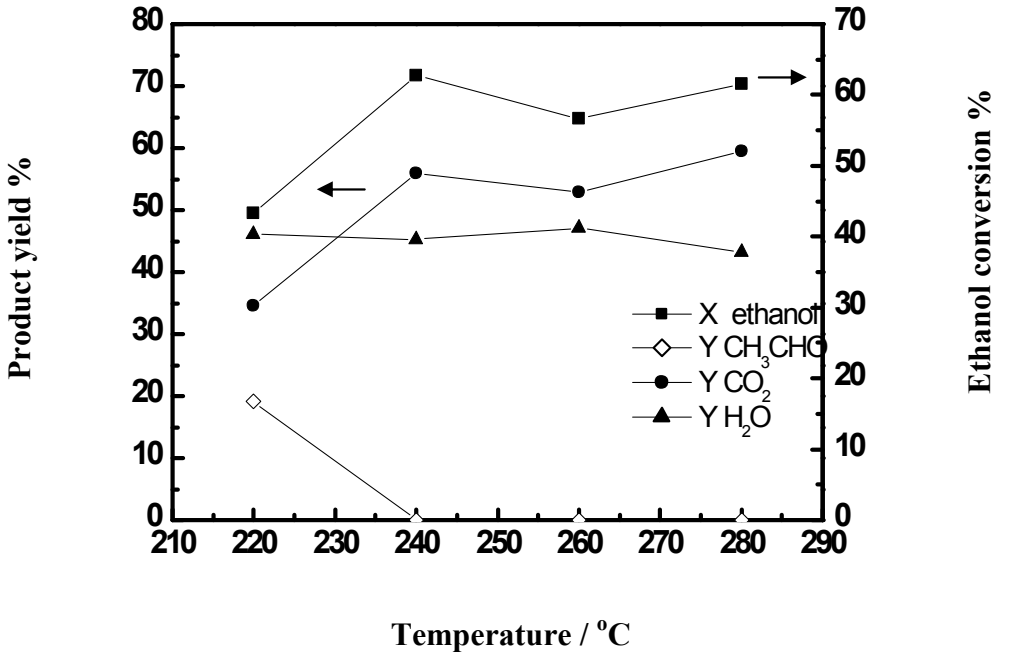

Figure 35: Effect of the reaction temperature on ethanol conversion and product distribution for ethanol partial oxidation over bulk α-Fe_2O_3 at O_2/ethanol ratio of 0.5 and a catalyst surface area of 1.0 m^2/g for a reaction time of 1 hour

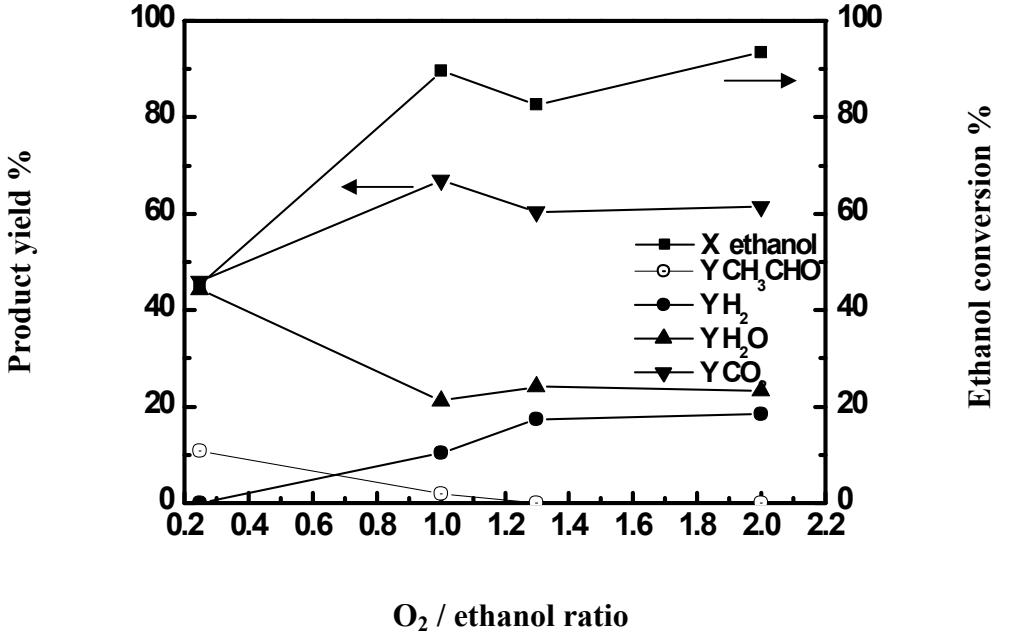

Figure 36: Effect of O_2/ethanol molar ratio on ethanol conversion, CH_3CHO yield for ethanol partial oxidation over bulk α-Fe_2O_3 catalyst at a temperature of 270°C, catalyst area of 1.0 m^2 and reaction time of 1 hour

The effect of oxygen to the ethanol ratio on the ethanol partial oxidation process was studied on reaction condition, i.e. a reaction temperature of 270°C and a catalyst area of 1 m^2. The O_2/ethanol ratio was varied by changing the oxygen partial pressure in a range from 12 to 120 mbar in separate experiments while the ethanol partial pressure was kept constant at 60 mbar. The effect of the O_2/ethanol ratio on the bulk Fe_2O_3 catalyst activity and product distribution are illustrated in Figure 36. The figure shows that by increasing the O_2/ethanol ratio from 0.25 to 2, the ethanol conversion increased from about 45% to 93%, respectively. For products distribution, acetaldehyde yield decreased from 15 to 0 % by increasing the O_2/ethanol molar ratio from 0.25 to 2. The hydrogen yield increased slightly up to 20.1% at a ratio of 2. At an O_2/ethanol ratio of 2, no acetaldehyde was detected while the hydrogen yield increased to 17.8 %. Those observations provided evidence that with increasing oxygen ratio the catalytic selectivity towards hydrogen was enhanced. The increase in ethanol conversion may be attributed to the rich oxygen environment which allows that more ethanol is oxidised. At a lower O_2/ethanol ratio, ethanol was adsorbed on the catalyst surface and oxidised to acetaldehyde, then at higher ratios oxidation extended further to acetaldehyde which generated hydrogen and carbon dioxide. The acetaldehyde oxidation can be proved by the fast decline of its yield at the O_2/Ethanol ratio.

These results indicated that the highest acetaldehyde production using a bulk α-Fe_2O_3 catalyst can be achieved at temperatures of 270°C and an O_2/ethanol molar ratio of 0.25 while hydrogen can be produced in a poor yield at higher ratios probably due to the dehydrogenation of acetaldehyde.

6.2.2. Nanoscale iron oxide catalysts

Here the results for the different phases of nanoscale Fe_2O_3 are discussed regarding the catalytic activity, represented by the ethanol conversion, the product distribution and the catalyst deactivation. The characterisations of the catalysts before and after ethanol oxidation are also reported. In an approach to optimise the process conditions, the parameters of temperature, O_2/ethanol ratio and catalyst with different surface area were studied and are reported.

6.2.2.1. γ-Fe_2O_3 catalyst

Before the ethanol oxidation was carried out over the catalyst surface, the catalyst as prepared was first characterised using the XRD, BET and SEM methods to determine the solid material phase and surface area. Figure 37 shows the X-ray pattern for the γ-Fe_2O_3 catalyst. The diffractogram shows a wide band at 35.5^o which is characteristic for the (311) crystalline structure of γ-Fe_2O_3. The broad XRD reflections indicate the nanosized prepared catalyst. The nanoscale γ-Fe_2O_3 was also proved by SEM analysis. Figure 38 shows the SEM image of the γ-Fe_2O_3 particles. The particle size was calculated from the photo by choosing 100 particles and determining the particle size for this. The particle size was plotted against its counts to show the particle size distribution. As a result of this procedure, the highest count assigned to a specific particle size was chosen as the particle size for this sample. Following this procedure, the particle size for γ-Fe_2O_3 was 4.9 nm.

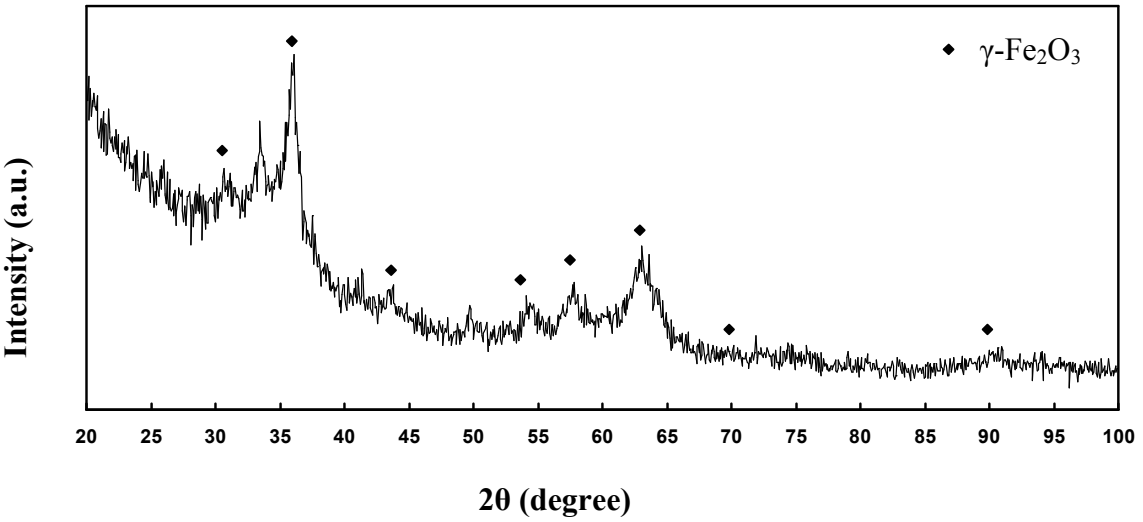

Figure 37: X-ray diffraction pattern of an unsupported γ-Fe_2O_3 fresh catalyst

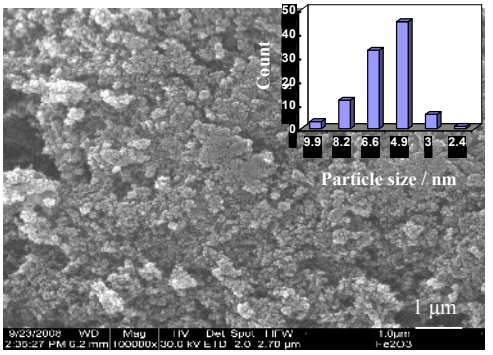

Figure 38: SEM for unsupported γ-Fe_2O_3 particles. The insert show the particle size distribution

The chemical composition of the catalyst was determined by energy dispersive X-ray (EDX) analysis. The EDX of such particles only resolved the presence of oxygen and iron atoms with an atomic content of 61% and 38%, respectively. The result obtained from BET showed that the surface area of the catalyst was found to be 240 m^2/g. The particle size for γ-Fe_2O_3 particles was also calculated from the BET method and gave the value of 5.1 nm which agreed with the result obtained from the SEM. For catalytic activity measurements, the catalyst was then packed in the reactor and the ethanol partial oxidation reaction was done over its surface under different conditions to optimise process conditions.

6.2.2.1.1. Effect of temperature

The experiment was conducted at an O_2/ethanol ratio of 0.5 over a 24 m^2 catalyst area corresponding to a catalyst weight of 0.1 g. Figures 39 and 40 represent the temperature dependence of the ethanol conversion and product selectivity over the γ-Fe_2O_3 catalyst surface. The catalyst was found to be highly active towards ethanol partial oxidation (POE) in this low temperature range which was represented by the high ethanol conversion within the reaction temperature range. By increasing the reaction temperature, the ethanol conversion was almost complete. The conversion increased slightly from 92% at 260^{o}C to 97% at 290^{o}C. The experimental data indicated that the reaction temperature had a significant impact on the hydrogen selectivity and yield. The catalyst selectivity toward hydrogen production increased from 42% to 80.6% at 260^{o}C and 290^{o}C, respectively. Considering the CO production, the CO selectivity decreased from 69% to 29% at temperatures of 260^{o}C and 290^{o}C, respectively.

In contrast, the water selectivity decreased with temperature increase from 57% to 19%, while the CO_2 selectivity increased from 30% to 70% in this temperature range. This trend of high selectivity towards H_2 and low CO production with increasing temperature can be explained by the competition between the side reactions: ethanol steam reforming may occur by the produced water from one side and water gas shift reaction (WGS) represented in equations 1, 2. Ethanol reforming increased the hydrogen production while the water gas shift reaction consumed the formed CO and also enhanced the hydrogen production. Furthermore, the activity for both reactions increased with increasing reaction temperature.

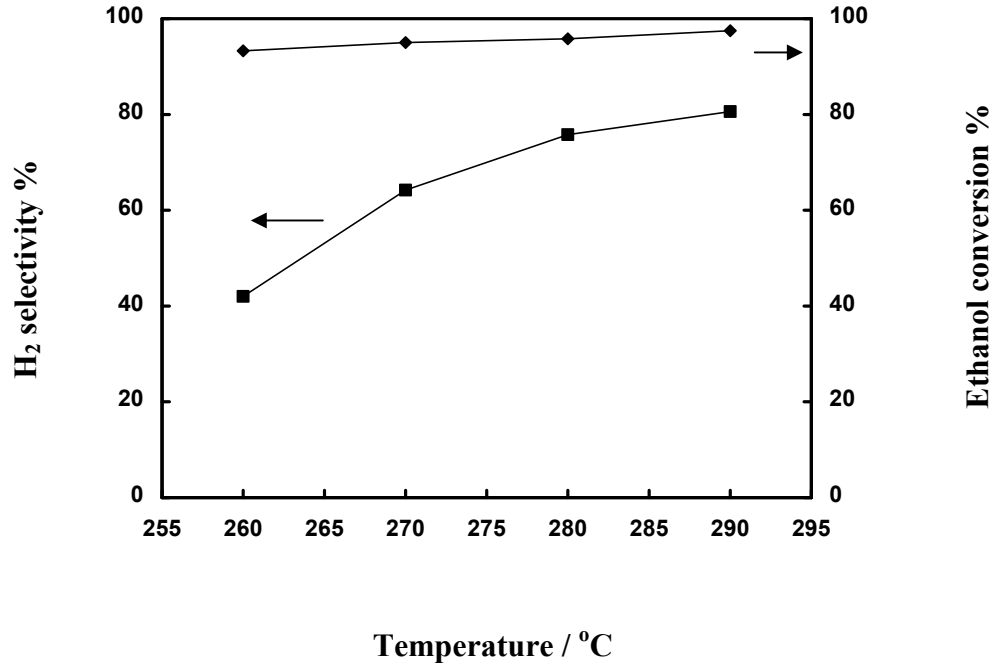

Figure 39: Effect of the reaction temperature on ethanol conversion and H_2 selectivity for ethanol partial oxidation over γ-Fe_2O_3 catalyst at an O_2/ethanol ratio of 0.5 and a catalyst area of 24 m^2 for a reaction time of 1 hour

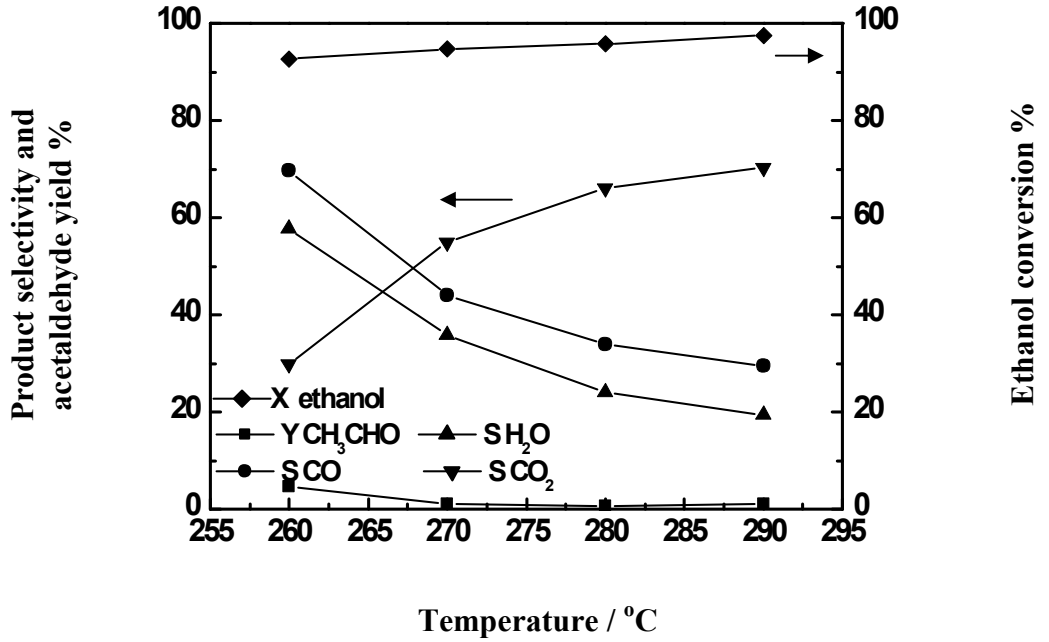

Figure 40: Effect of reaction temperature on ethanol conversion, products selectivities and acetaldehyde yield for ethanol partial oxidation over γ-Fe_2O_3 catalyst at an O_2/ethanol ratio of 0.5, a catalyst surface area of 24 m^2 and a reaction time of 1 hour

$$C_2H_5OH + 3\,H_2O \longrightarrow 6\,H_2 + 2\,CC \qquad \Delta H^{\circ}_{298} = +374\,kJ\,mol^{-1} \qquad (1)$$

$$CO + H_2O \longrightarrow CO_2 + H_2 \qquad \Delta H^{\circ}_{298} = -41\,kJ\,mol^{-1} \qquad (2)$$

These results indicating that ethanol can be partially oxidised to produce a reasonable hydrogen yield with a considerably lower CO yield in the low temperature range from 260°C to 290°C. Several authors reported that ethanol can be oxidised to CO_2 and H_2 in the same temperature range and also up to 500°C due to the ethanol steam reforming by the formed water during ethanol partial oxidation and/or water gas shift reaction [27, 104, 153]. The reaction temperature of 270°C was chosen as the optimum temperature because at higher temperatures the catalyst tends to be reduced to Fe_3O_4 (magnetite) once it was heated up and after reaction at 270°C for more than 2 hours.

6.2.2.1.2. Effect of the O_2/ethanol ratio

In order to enhance the hydrogen production via ethanol partial oxidation, the oxygen to ethanol ratio was varied. Figure 41 reflects the effect of the O_2/ethanol ratio on the ethanol conversion and hydrogen selectivity. With increasing O_2/ethanol ratio, the ethanol conversion increased gradually and reached its maximum of 99.9 at an O_2/ethanol ratio of 2.

The hydrogen selectivity was enhanced from 64% and reached a maximum of 79% with increasing O_2/ethanol ratio up to a ratio of 1.0; then it obviously decreased to 45% at an O_2/ethanol ratio of 2. This behaviour can be explained in this way that at an O_2/ethanol ratio higher than 1.5, the stoichiometric ratio for the ethanol oxidation, the produced hydrogen was further oxidised to water according to equation 3;

$$H_2 + 0.5\,O_2 \longrightarrow H_2O \qquad \Delta H^{\circ}_{298} = -241\,kJ\,mol^{-1} \qquad (3)$$

Wang *et al.* [63] observed similar results by studying the ethanol oxidation over a Ni-Fe catalyst. They observed that hydrogen selectivity increased by increasing the O_2/ethanol ratio up to 1.5, which was then decreased at higher ratios. They attributed the effect of hydrogen selectivity decreasing at O_2/ethanol ratios higher than 1.5 to the hydrogen oxidation by excess oxygen.

Regarding the production of carbon monoxide, the carbon monoxide yield decreases with increasing O_2/ethanol ratio. Figure 30 illustrates the effect of the O_2/ethanol ratio on the product distribution for ethanol oxidation over the γ-Fe_2O_3

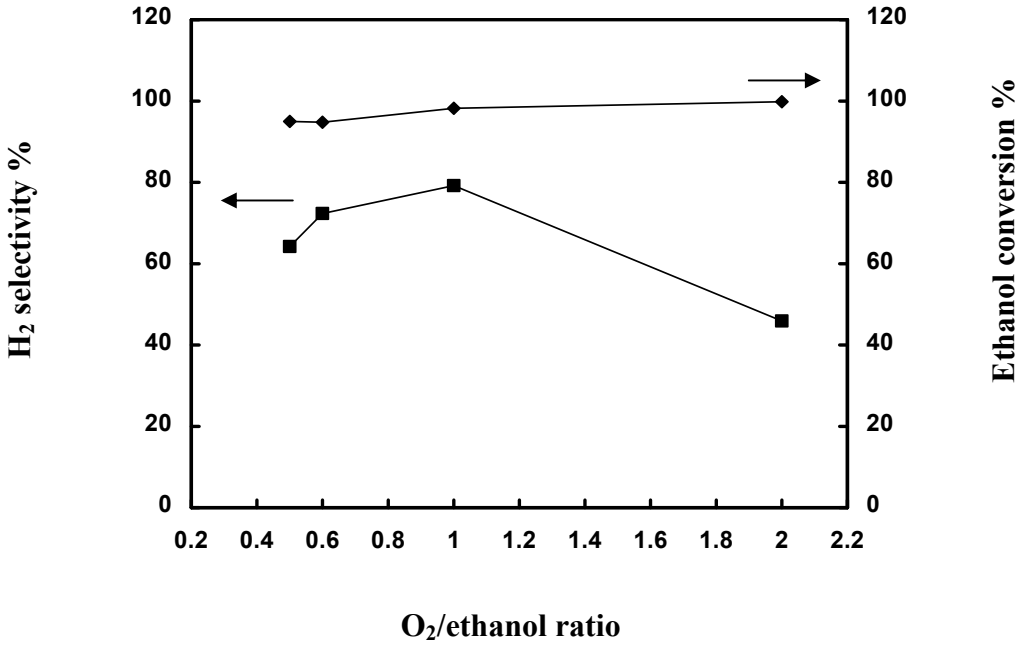

Figure 41: Effect of the O_2/ethanol ratio on ethanol conversion and H_2 selectivity for ethanol partial oxidation over γ-Fe_2O_3 catalyst at a reaction temperature of 270°C and a catalyst area of 24 m^2 for a reaction time of 1 hour

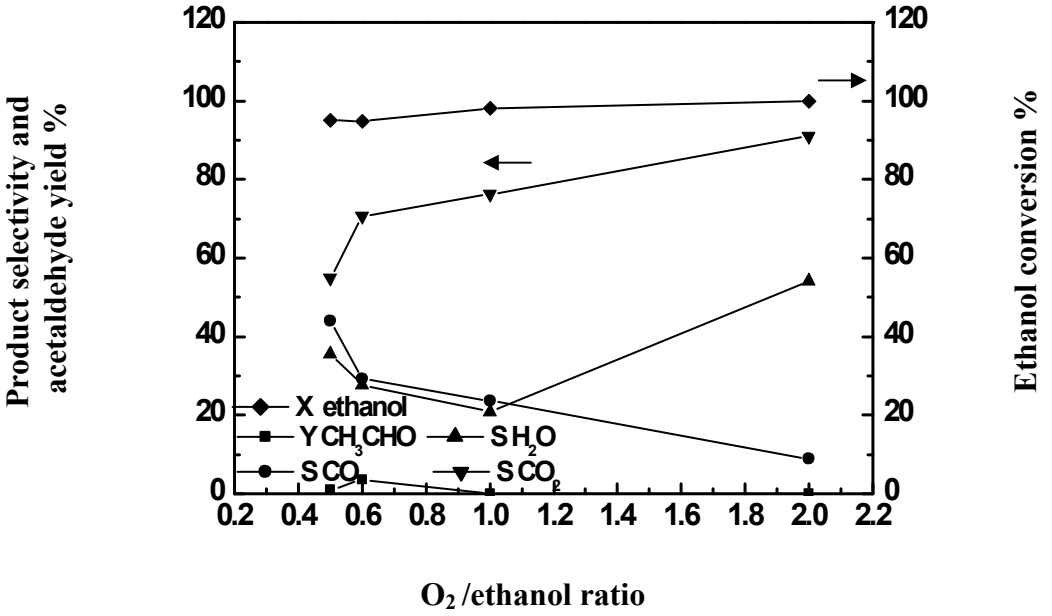

Figure 42 : Effect of the O_2/ethanol ratio on ethanol conversion, products selectivity and acetaldehyde yield for ethanol partial oxidation over γ-Fe_2O_3 catalyst at a reaction temperature of 270°C and a catalyst area of 24 m^2 for a reaction time of 1 hour

The carbon monoxide was detected in the complete range investigated. The CO selectivity was 44% at an O_2/ethanol ratio of 0.5. However, the addition of more O_2 dramatically decreased the CO selectivity to 8.7 at an O_2/ethanol ratio of 2. This result can be attributed to a competition between water gas shift reaction according to equation 2 and oxidation of CO formed in the presence of a rich oxygen environment to CO_2 according to equation 4 over the catalyst surface [83, 117].

$$CO + 0.5\ O_2 \longrightarrow CO_2 \qquad \Delta H^{\circ}_{298} = -283\ kJ\ mol^{-1} \qquad (4)$$

The oxidation of CO may also be enhanced by the ability of iron oxide to participate in the oxidation reaction. An iron oxide reducibility was reported by many authors [139]. The mechanism of metal oxide reducibility during the oxidation reactions were first suggested by Mars and van-Krevelen [154]. The mechanism suggests that the presence of oxygen intermediates came from the ability of metal oxide lattice to lose one oxygen atom, which has a high activity for the oxidation of CO to CO_2. This lattice oxygen from the catalyst surface was involved in the reaction and then compensated by O_2 from the feed. Therefore, high lattice oxygen mobility is favourable.

In this set of experiments, the O_2/ethanol molar ratio of 1.0 showed higher hydrogen selectivity with almost complete conversion of ethanol so that this value was chosen as the optimum ratio and later used to evaluate the catalyst performance over different catalyst surface areas and to investigate the catalyst stability for POE reaction.

6.2.2.1.3. Effect of the surface area

In this set of experiments, the catalyst surface area was varied by using different catalyst weights for separate experiments while the other reaction conditions were kept constant. Figure 43 illustrates the effect of a catalyst surface area on the hydrogen selectivity. The catalyst area in a range from 4.8 to 24 m^2 was studied to see how far the surface area influences the ethanol conversion and hydrogen formation on reaction conditions at 270^{o}C and the O_2/ethanol ratio. The results showed that the catalyst was found to be highly active towards POE even at a very low catalyst area of 4.8 m^2. An increase in ethanol conversion from 92% up to 98% over the catalyst area of 4.8 and 24 m^2 respectively was found. Hydrogen selectivity increased with increasing surface area, i.e. H_2 selectivity increased from 23 % over a catalyst area of

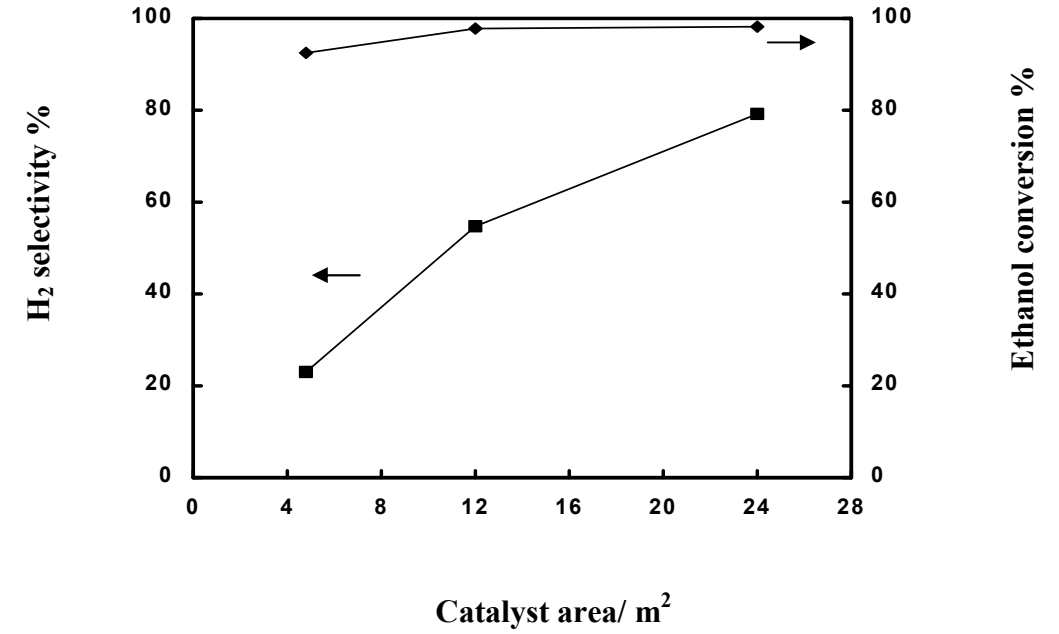

Figure 43: Effect of the catalyst area on ethanol conversion and H_2 selectivity for ethanol partial oxidation over γ-Fe_2O_3 catalyst at 270°C and an O_2/ethanol ratio of 1.0 for a reaction time of 1 hour

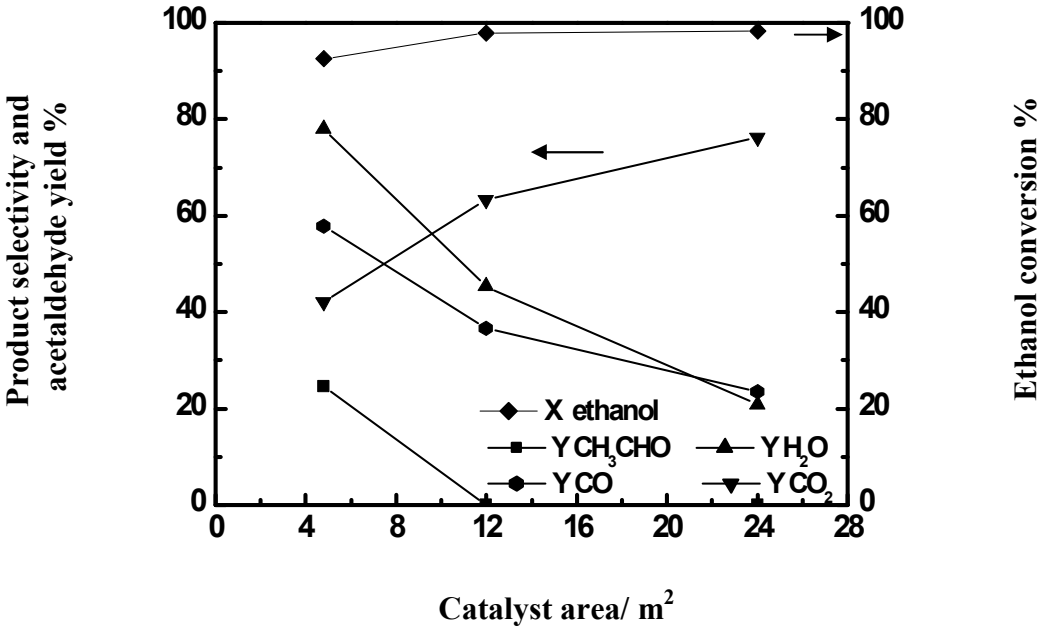

Figure 44: Effect of the catalyst area on ethanol conversion, products selectivity and acetaldehyde yield for ethanol partial oxidation over γ-Fe_2O_3 catalyst at a reaction temperature of 270°C and an O_2/ethanol ratio of 1.0 for a reaction time of 1 hour

4.8 m^2 until a maximum of 79% was reached over a catalyst area of 24 m^2. The effect of the surface area on the CO formation and the other products distribution results were represented in Figure 44. The figure shows that the CO selectivity decreased from 57% produced over a catalyst area of 4.8 m^2 to about 23% over a catalyst area of 24 m^2. These observations may be attributed to the fact that the presence of more surface area provides more active sites enhancing the ethanol oxidation process. Moreover, it provides evidence that the iron oxide supplies oxygen through the Mars van Krevelen to the POE reaction to oxidise CO with such a high activity since there was no more oxygen supplied and all experiments were carried with the same oxygen concentrations.

6.2.2.1.4. Catalyst stability

The long term stability of the present catalyst was studied on reaction conditions at 270^oC, an O_2/ethanol ratio of one over a catalyst area of 12 m^2. The low surface area was used here in order to be able to compare this catalyst results over a constant area with the following catalysts. This was because of the smaller surface area of the next catalysts which would need a higher weight to reach a catalyst area of 24 m^2 what was not possible due to the reactor capacity. In the catalyst stability experiments, stability tests were carried out for 10 hours. The catalyst was subjected to the ethanol oxidation reaction for 5 and 10 hours respectively, then the setup was evacuated and later a new gas mixture was fed to the reactor and circulated over the catalyst surface for one hour to test the catalyst activity after 10 hours of time on stream. Figure 45 shows the effect of time on stream for the ethanol partial oxidation on ethanol conversion and H_2 selectivity. In Figure 45 the zero time on stream represents the results obtained over the fresh catalyst sample. By testing the catalyst for 10 hours of reaction, the catalytic activity significantly decreased where the conversion of ethanol decreased from 97% to 92%. The hydrogen selectivity declined strongly along the investigated time on stream. The hydrogen selectivity decreased from 54% to 5 in a time intervals of 10 hours. This may be attributed to the deactivation or due to a phase change as shown in Figure 47. A continuous decrease of CO formation along the time on stream was observed as demonstrated in Figure 46. The figure shows that CO selectivity also decreased from 36.7% after only one hour to about 7.2% after 10 hours on stream which may attributed to CO oxidation reactions according to equations 4 (see page 78).

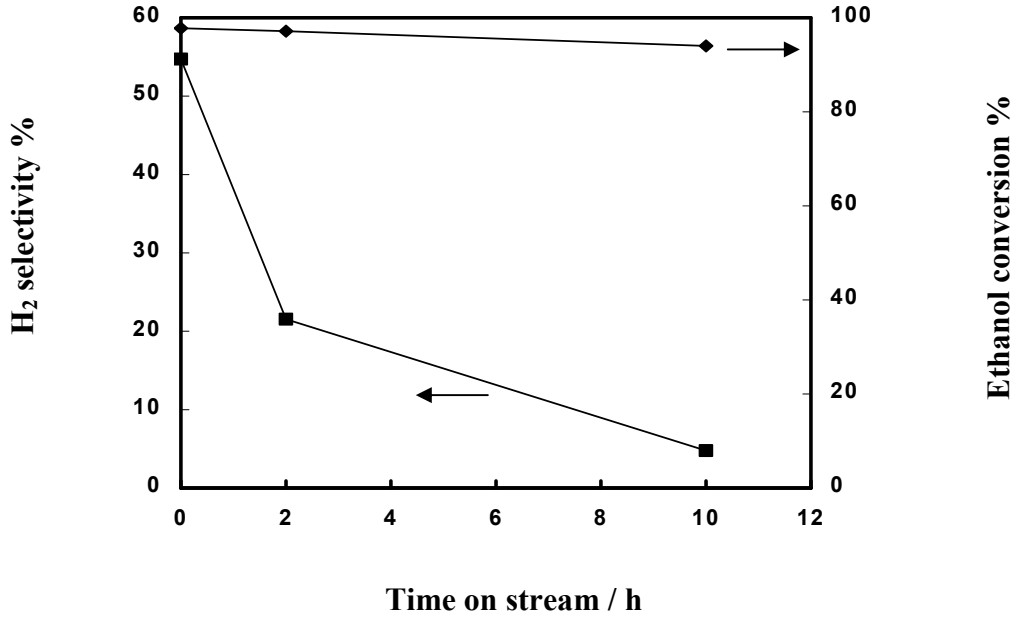

Figure 45: Effect of catalyst deactivation on ethanol conversion and H_2 selectivity for ethanol partial oxidation over γ-Fe_2O_3 catalyst at an O_2/ethanol ratio of 0.1 and a catalyst area of 12 m^2

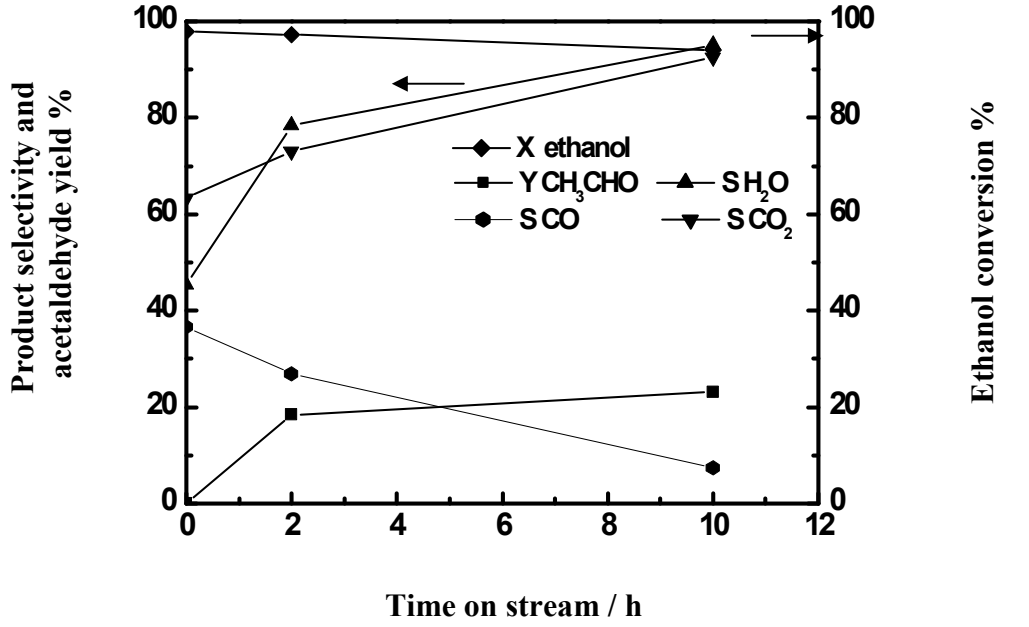

Figure 46: Effect of catalyst deactivation on ethanol conversion, products selectivity and acetaldehyde yield for ethanol partial oxidation over γ-Fe_2O_3 at an O_2/ethanol molar ratio of 0.1 and a catalyst surface area of 12 m^2

6.2.2.1.5. Catalyst characterisation

The catalyst was characterised by XRD, SEM and BET after 10 hours time on stream to give an overview of the catalyst changes during the reaction time. Figure 47 compares the XRD patterns of the fresh and used catalysts for 5 and 10 hours. the figure shows the phase change of used and fresh catalysts through the XRD patterns indicated for each. The figure shows that the catalyst give the XRD patterns of 2θ at 30.06°, 35.45°, 43.1°, 56.9°, 62.5°, 74.9° and 89.8° which are characteristic for Fe_3O_4 (magnetite) with (311) orientation after 5 hours on stream of reaction. The N_2 adsorption isotherms for used catalysts were measured using the BET technique. The BET measurements showed a sharp decrease in the surface area (S_{BET}) after 10 hours on stream. The S_{BET} was decreased from 240 m^2/g measured to fresh catalyst to 80 m^2/g for the used one after 10 hours time on stream. The SEM images of the used catalysts after 5 and 10 hours time on stream were shown in Figure 48. The figure shows that the particle size distribution is not so wide that the particle size distribution found to be in a range from 7 to 10.5 nm. From the BET and SEM analysis it is clear that, although there was a sharp decrease in the surface area but the particle size was not changed so far after 10 hours reaction time, this may be explained by the loss of some active sights through phase change or coking and carbon deposition over the catalyst surface area.

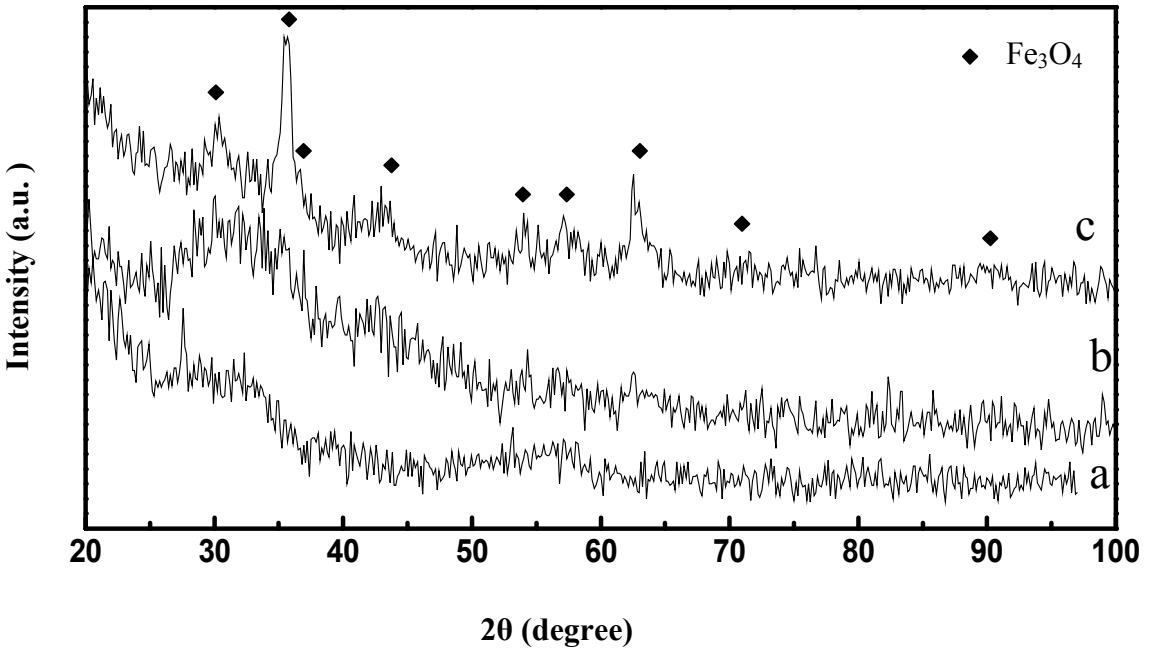

Figure 47: Powder X-ray diffraction patterns of unsupported γ-Fe_2O_3 a) fresh, b) after 5 hours and c) after 10 hours time on stream

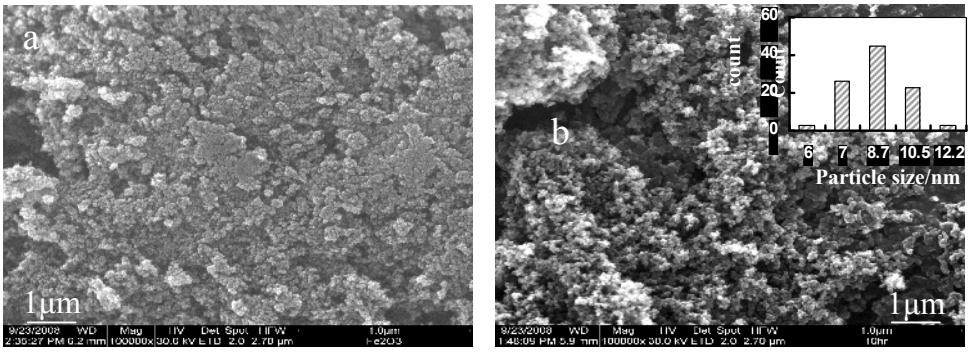

Figure 48: SEM for unsupported a) fresh and b) used after 10 hours γ-Fe_2O_3 particles catalyst. The insert show the particle size distribution

6.2.2.2. α/γ-Fe_2O_3 catalyst

In this part, a sample of α/γ-Fe_2O_3 iron oxide mixed phases was prepared by Orthner and Roth and investigated as a catalyst for ethanol partial oxidation. The catalytic activity for such a catalyst was studied under different conditions of temperature and O_2/ethanol in order to compare it with the other catalysts under investigation in this work. For this purpose, the experiments of ethanol partial oxidation were carried out over 12 m^2 catalyst area for one hour. Before the catalyst was subjected to POE reaction, the particles phase, surface area and morphology were characterised by XRD, BET and SEM respectively. Structural characteristics of the samples under study were investigated by X-ray diffraction. Figure 49 shows the XRD patterns obtained from the prepared iron oxide sample. The XRD patterns were indicated at 2θ of 24.12°, 33.11°, 35.61°, 49.48°, 54.08° and 72.17° while the highest pattern indicated at 33.11 ° corresponded to (104) orientation of α-Fe_2O_3.

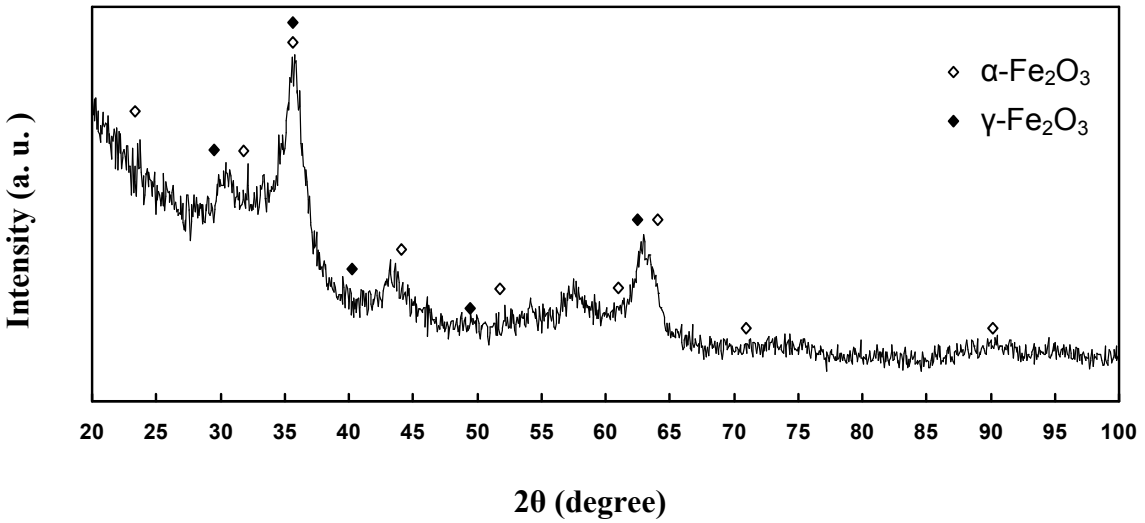

Figure 49: Powder X-ray diffraction patterns of unsupported α/γ-Fe_2O_3 fresh catalyst

The XRD patterns also gave a reflection of 2θ at 30.2°, 35.5°, 43.3°, 57.1°, 62.7° and 90.2° which characterise the γ-Fe_2O_3. The highest peak was detected at 35.5° indicating the (311) orientation of γ-Fe_2O_3.

Figure 50 shows an SEM image for the prepared catalyst. The particle size was estimated from this SEM image according to the procedure discussed before (see page 46) and was found to be 9.5 nm. The surface area (S_{BET}) for the catalyst was measured using the N_2 adsorption isotherm and found to be 160 m^2/g. The chemical composition of the catalyst was detected by using the energy dispersive X-ray (EDX) analysis. The EDX analysis of the catalyst sample showed the presence of oxygen and iron content only. The EDX analysis showed 40.59% and 59.41% iron and oxygen atomic content, respectively.

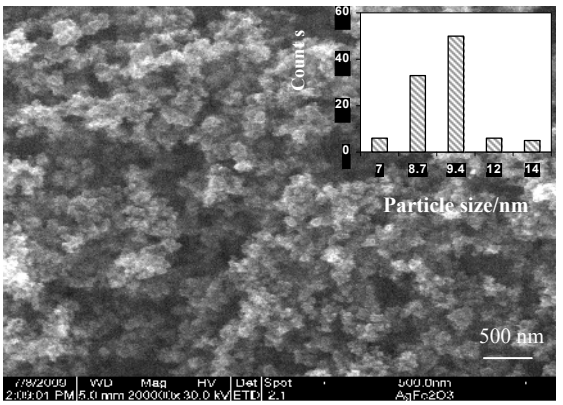

Figure 50: SEM image of an unsupported α/γ-Fe_2O_3 fresh catalyst. The insert show the particle size distribution

6.2.2.2.1. Effect of the temperature

The partial oxidation of ethanol was carried out over the catalyst under investigation at temperatures ranging from 260°C to 290°C and an O_2/ethanol ratio of 0.5 for 1 hour. The parameters of the temperature and the O_2/ethanol ratio were again investigated here over this catalyst to make sure whether these determined optimum conditions are applicable to all the iron oxide phases.

Figure 51 shows the effect of temperature on ethanol conversion and H_2 selectivity. The ethanol conversion was found to be complete over the mixed phase iron oxide catalyst. Typically, the ethanol conversion reached 99.9 % at 260°C. Ethanol conversion was found to decrease slightly from 99.9% to 95.1% by increasing the temperature from 260 to 290°C. The hydrogen yield was found to increase from 14.8% to 37% within the investigated temperature range. Meanwhile, the H_2

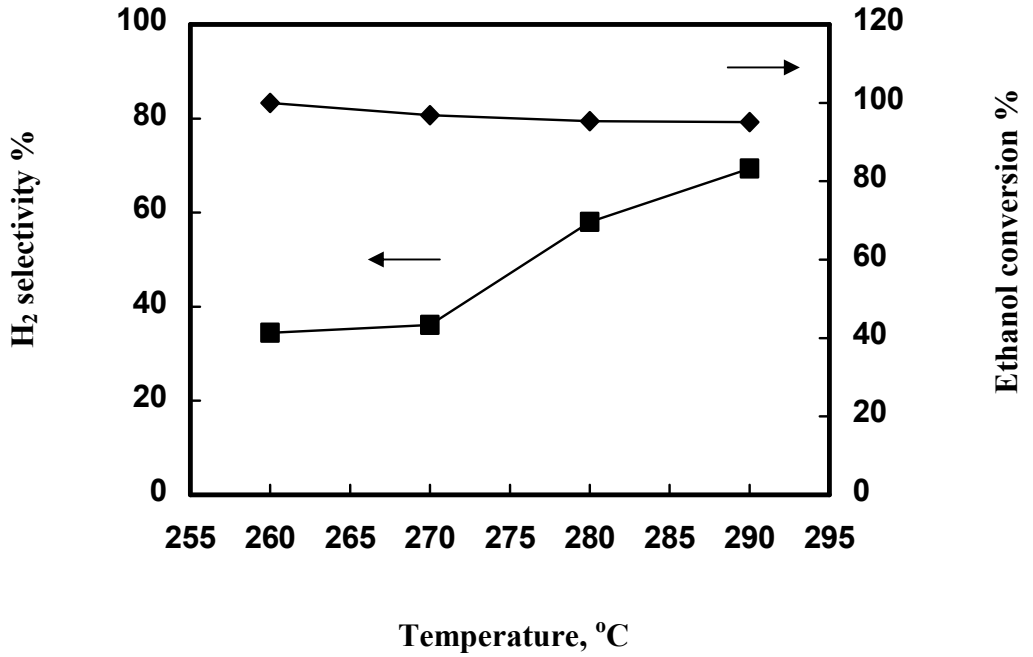

Figure 51: Effect of the reaction temperature on ethanol conversion and H_2 selectivity for ethanol partial oxidation over α/γ-Fe_2O_3 at an O_2/ethanol ratio of 0.5 and a catalyst area of 12 m^2 for a reaction time of 1 hour

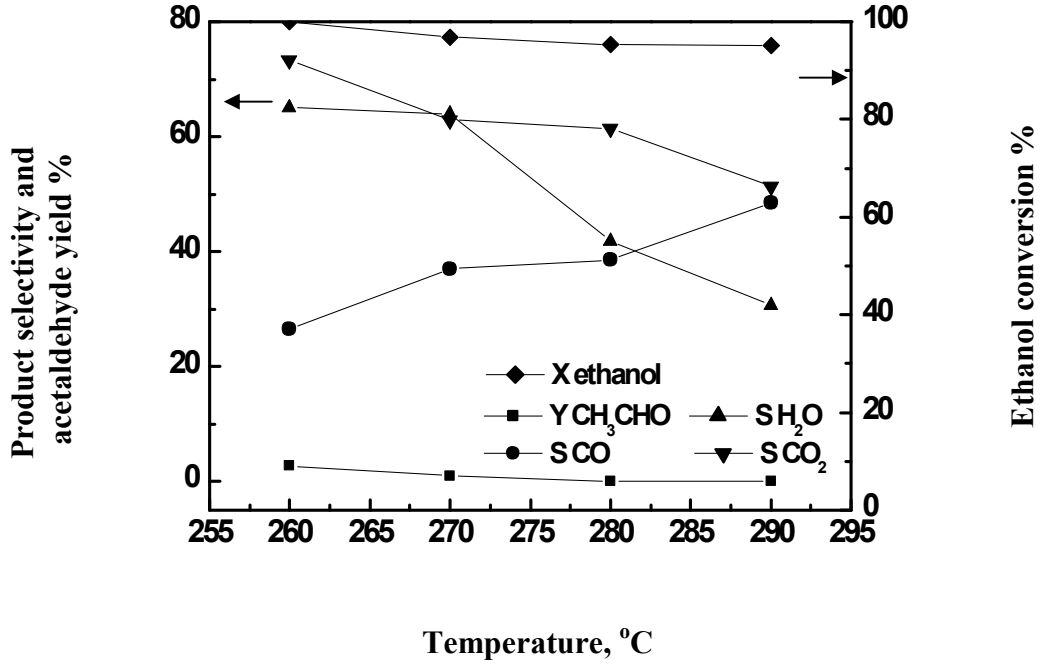

Figure 52: Effect of the reaction temperature on ethanol conversion, products selectivity and acetaldehyde yield for ethanol partial oxidation over α/γ-Fe_2O_3 at an O_2/ethanol ratio of 0.5, a catalyst area of 12 m^2 and a reaction time of 1 hour

selectivity significantly increased from 34% to 69%. The product distribution at different temperatures is illustrated in Figure 52. The figure shows that the water selectivity decreased with increasing temperature. The catalyst selectivity towards CO_2 formation decreased with increasing temperature. In comparison, an increase of the reaction temperature caused an increase of the CO selectivity (S_{CO}) from 26 % to 48% at a reaction temperature from 260°C to 290°C respectively. Contrary to what might be expected, the above results showed that the hydrogen and carbon monoxide increased with rising temperature. These results may be explained by the following: the α/γ-Fe_2O_3 catalyst may promote the adsorption and decomposition of ethanol to CH_4 and CO. Furthermore, methane may be reformed by the generated water and/or CO_2 to CO and H_2 which increase both concentrations [84] according to equation 5:

$$CH_4 + H_2O \longrightarrow CO + 3\,H_2 \qquad \Delta H^{\circ}_{298} = 221\ kJ\ mol^{-1} \tag{5}$$

Here the H_2, CO and CO_2 concentrations were controlled by the reverse water gas shift equilibrium according to equation 6.

$$CO_2 + H_2 \rightleftharpoons CO + H_2O \qquad \Delta H^{\circ}_{298} = 41\ kJ\ mol^{-1} \tag{6}$$

Ethanol oxidation via ethoxy species was observed on the iron oxide surface [139], and the promotion of iron oxide for the water-gas shift reaction was also reported [155] before. Several authors reported a high yield of H_2 and CO with a considerable production of methane from ethanol partial oxidation over Pt/CeO_2 [29], Pd/Y_2O_3 [92], Ir/CeO_2 [84] Pt/Ce-Al_2O_3 [22], Ni//Al_2O_3 [17] and Pt/ZrO_2 [117]. All of them attributed similar results to the reforming of formed methane with water to CO and H_2 while CO conversion to CO_2 was controlled by reverse water gas shift reaction. To enhance the hydrogen production and reduce the CO formation, the effect of the O_2/ethanol ratio was investigated.

6.2.2.2.2. Effect of the O_2/ethanol ratio

The effect of the O_2/ethanol ratio on the activity of the α/γ-Fe_2O_3 catalyst and its selectivity towards hydrogen production at 270°C is illustrated in Figure 53. When increasing the O_2/ethanol ratio from 0.5 to 2, the amount of oxygen was increased while the ethanol partial pressure was kept constant at 60 mbar. The ethanol conversion increased and reached a maximum of 99.9% at a ratio of 2. On the other hand, hydrogen selectivity increased and reached a maximum of 72 % at an O_2/ethanol ratio of 1; then it further decreased to 30.5% at a ratio of 2 which is higher

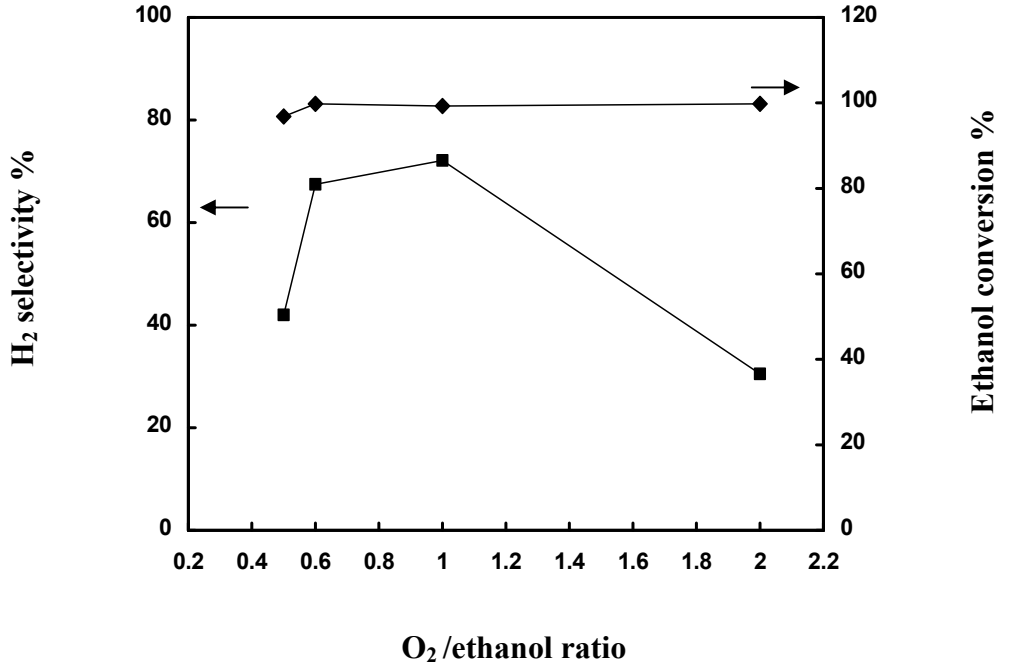

Figure 53: Effect of the O_2/ethanol ratio on ethanol conversion and H_2 selectivity for ethanol partial oxidation over α/γ-Fe_2O_3 at a reaction temperature of 270°C and a catalyst area of 12 m^2 for a reaction time of 1 hour

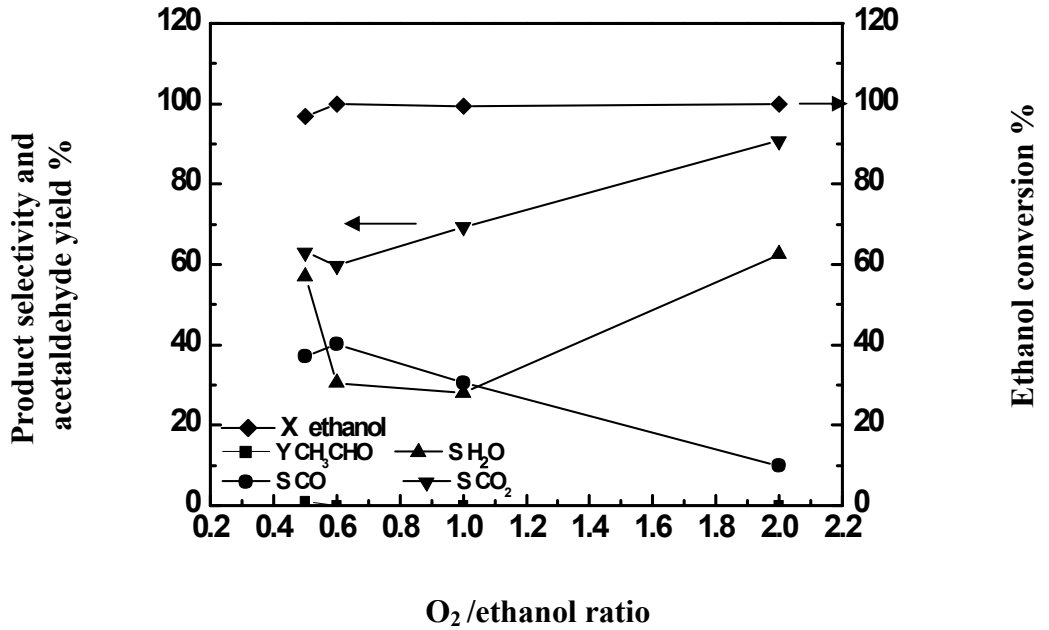

Figure 54: Effect of the O_2/ethanol molar ratio on ethanol conversion products selectivity and acetaldehyde yield for ethanol partial oxidation over α/γ-Fe_2O_3 at a reaction temperature of 270°C and a catalyst area of 12 m^2 for a reaction time of 1 hour

than the stoichiometric value. These results may be explained by the fact that the increased oxygen concentration enhanced the ethanol oxidation. For hydrogen production, the selectivity increased due to the enhancement of ethanol oxidation and intermediates continuous dehydrogenation until the stoichiometric ratio was reached while over the stoichiometric ratio the formed hydrogen was further oxidised to water according to the oxygen rich environment. This explanation can be proved by considering the water selectivity variation with the O_2/ethanol ratio. The catalyst showed a low water selectivity within the O_2/ethanol ratio range until the ratio of one was reached then the water selectivity was increased. Figure 54 shows the product distribution for ethanol partial oxidation over the α/γ-Fe_2O_3 catalyst at different O_2/ethanol ratios. Considering the CO production, the figure indicates that CO selectivity initially rose to 41.1% at an O_2/ethanol ratio of 0.6 and then decreased with increasing O_2/ethanol ratio to reach about 10% at an O_2/ethanol ratio of 2. On the other hand, the catalyst selectivity towards CO_2 was initially decreased and then increased by increasing oxygen ratio from 0.6 to 2. This trend for the CO and CO_2 selectivity with increasing O_2/ethanol ratio may be attributed to the high availability of oxygen that can oxidise the CO to CO_2.

From the results described above the mixed phase α/γ-Fe_2O_3 catalyst showed a high activity towards ethanol oxidation reaction which was expressed by a very high ethanol conversion. The conversion reached the maximum of 99.9% at 270^{o}C and an ethanol to oxygen ratio of 2. Since the highest hydrogen selectivity of 72% with low CO selectivity was achieved at 270^{o}C and an O_2/ethanol ratio of 1 over a catalyst area of 12 m^2, these conditions were taken as the optimum condition for the hydrogen production over this catalyst. These conditions also agreed with the results for γ-Fe_2O_3 catalyst described before (see page 79).

6.2.2.2.3. Catalyst characterisation

The catalyst was subjected to the ethanol partial oxidation reaction at 270^{o}C and an O_2/ethanol ratio of 1 for 5 and 10 hours time on stream, then it was analysed by means of XRD while the surface area was determined using the BET technique, and finally the SEM was used to determine the morphology and check if agglomeration of the particles might have taken place during the reaction. Figure 55 shows the XRD patterns for the fresh and used catalyst after 5 and 10 hours on stream, respectively. The figure shows that reflections at 2θ of 30.2^o, 35.5^o, 43.1^o, 53.2^o, 57.1^o, 62.5^o, 73.8^o

and 89.5° were obtained representing a characteristic pattern for Fe_3O_4 (magnetite). These patterns were assigned for the catalyst for both investigated times on stream, i.e. after 5 and 10 hours. This proved that the catalyst was also reduced during the ethanol oxidation experiment from Fe_2O_3 to Fe_3O_4. The sharp peaks for magnetite were seen even after 5 hours time on stream what proved the fast reduction of the catalyst. The BET surface area found to be decreased from 160 m^2/g for the fresh catalyst to 51.5 m^2/g after 10 hours time on stream. Figure 56 shows the SEM image for the used catalyst after 10 hours. The SEM shows a significant increase in particle size from the fresh sample, the particle size changed from 9.4 nm for the fresh catalyst to 19.2 nm after 10 hours.

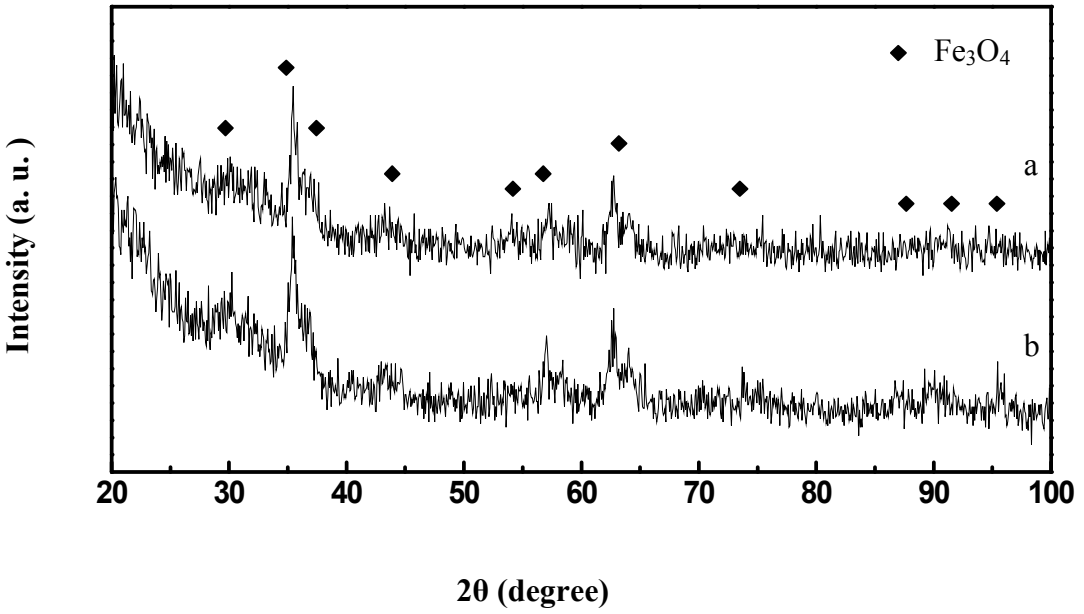

Figure 55: Powder X-ray diffraction patterns of unsupported α/γ-Fe_2O_3 a) after 5 hours and b) after 10 hours time on stream

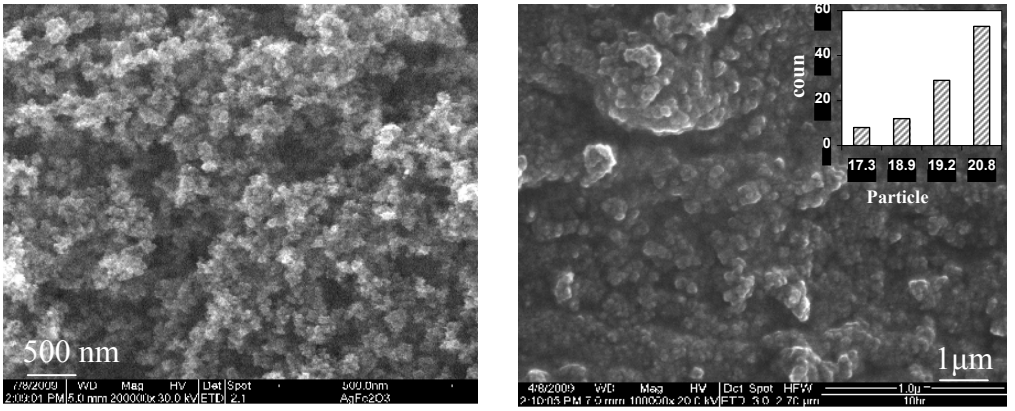

Figure 56: SEM and particle size distribution for unsupported a) fresh and b) used for 10 hours α/γ-Fe_2O_3 catalyst

6.2.2.3. α-Fe_2O_3 catalyst

α-Fe_2O_3 particles prepared by CVS using the home made setup was the last unsupported catalyst investigated in ethanol partial oxidation. The catalyst was characterised by XRD, BET and SEM to determine its phase, surface area and morphology before the catalyst was subjected to ethanol partial reaction. Figure 57 shows the XRD pattern for the fresh and as prepared catalyst. The XRD pattern indicated were at the 2θ angle of 24.1°, 33.1°, 35.6°, 49.4°, 54.0° and 72.1° degrees while the highest pattern indicated at 33.15 ° corresponding to (104) reflection of α-Fe_2O_3 (hematite). The XRD gave well defined peaks indicating the crystalline structure. Energy dispersive X-ray (EDX) analysis was used to determine the chemical composition of the catalyst. The EDX of such particles distinguished the presence of only oxygen and iron with an atomic of iron of 41.27% and oxygen of 58.73% corresponding to Fe_2O_3. The BET surface area (S_{BET}) for the as prepared catalyst was measured using the N_2 adsorption isotherm at -77°C.

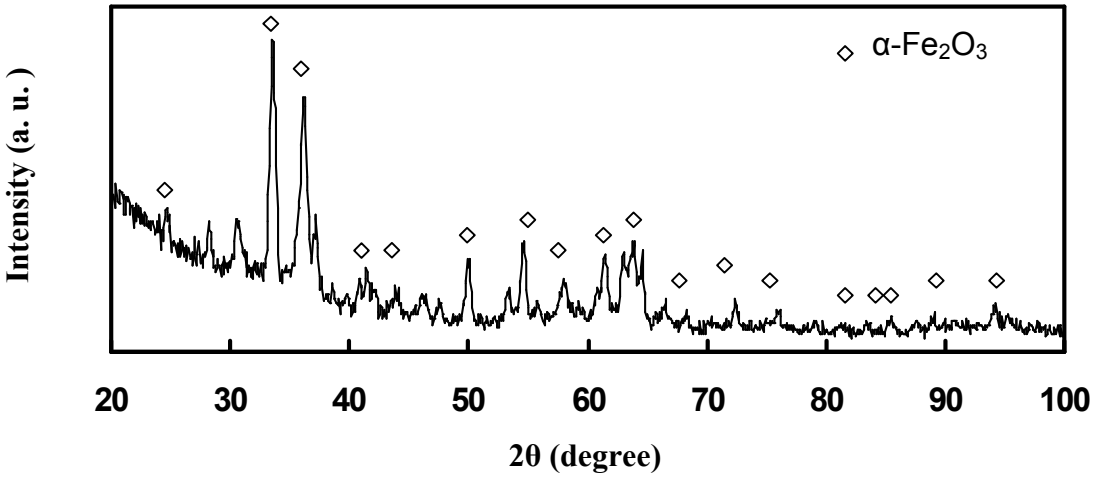

Figure 57: Powder X-Ray diffraction patterns of unsupported α -Fe_2O_3 fresh catalyst

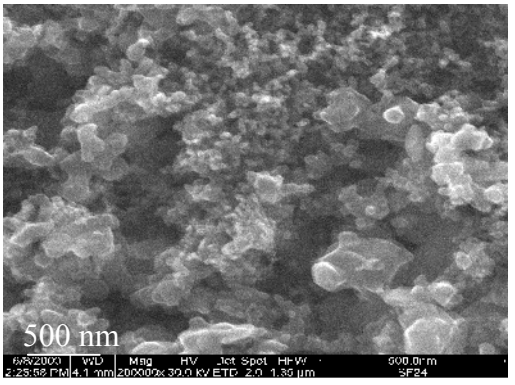

Figure 58: SEM image and particle size distribution of unsupported α-Fe_2O_3 fresh catalyst

The S_{BET} for the catalyst showed a very small surface area and was found to be only 6 m^2/g. Figure 58 shows the SEM image of the α-Fe_2O_3. The SEM for the as prepared catalyst indicated the nanosized particles formation. The particle size was determined by calculation using the BET result and was confirmed by measuring the dynamic light scattering (DLS).

The particle size was found to be 10.7 nm from DLS and 12 nm from the BET calculations which indicate the monocrystalline particles formation.

6.2.2.3.1. Catalytic activity

The optimum conditions proved over the previous catalysts were applied here in order to investigate the α-Fe_2O_3 catalytic activity towards ethanol partial oxidation (POE) and to compare its catalytic activity and products selectivity with the previous catalysts. Figure 59 represents the ethanol conversion and product distribution obtained for the ethanol partial oxidation at a reaction temperature of 270°C, an O_2/ethanol ratio of 1 over a catalyst area of 12 m^2 for one hour. The figure shows that the ethanol conversion was almost complete (95.2 %). In terms of selectivity, the main products obtained were hydrogen and carbon dioxide with a considerable water content of 37%. The ability to produce a high amount of CO_2 may be attributed to the enhancement of iron oxide catalyst for water gas shift reaction since there is no oxygen rich environment to directly oxidise the formed CO to CO_2.

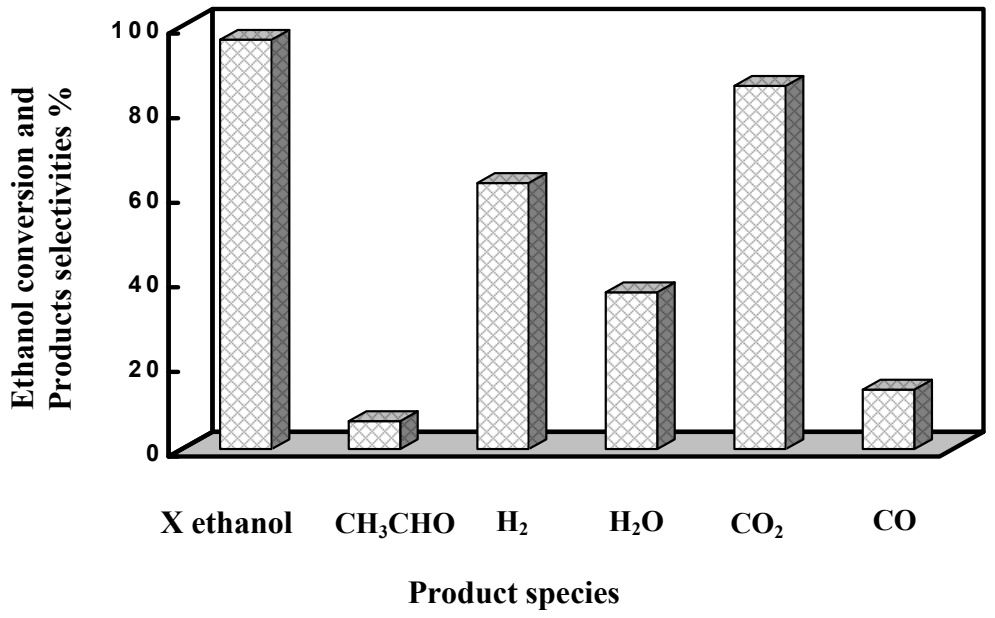

Figure 59: The ethanol conversion and products selectivity obtained over unsupported α-Fe_2O_3 at 270°C, O_2/ethanol ratio of 1 over a catalyst area of 12 m^2 for a reaction time of one hour

Another possible prospective reaction path can be proposed firstly by oxidising ethanol to acetaldehyde. Then acetaldehyde is dehydrogenated to form an ethoxy species which is then oxidised to acetic acid. The acetic acid is later decomposed to carbonate species which further oxidised to CO_2 while of negligible amount of CO is formed.

6.2.2.3.2. Catalyst stability

The catalyst stability was tested on the reaction condition of 270^{o}C, an O_2/ethanol ratio of 1 over a catalyst area of 12 m^2 for 10 hours. In Figures 60 and 61, the ethanol conversion and product distribution are represented as a function of time on stream for the ethanol partial oxidation outlet.

Considering the catalytic activity, the ethanol conversion of 96% was measured over the fresh catalyst which remained near this value without obvious variation during the entire time on stream investigation. However, a significant change in the hydrogen and carbon containing product yields and selectivity was observed.

For hydrogen selectivity, it reached 64.4% at the beginning and remained up to 5 hours on stream and then it decreased to 52% after 10 hours. Meanwhile, a similar behaviour was observed for the CO_2 yield which emerged at high values of 71% at the beginning and then slightly decreased to 66% after 5 hours, then it was kept at 67% after 10 hours on stream. The high yield was also accompanied by a high selectivity where the CO_2 selectivity for the fresh catalyst was 85.9% and increased within the entire investigated time range up to 90% after 10 hours of ethanol partial oxidation over the catalyst surface. Water and acetaldehyde yields also increased with the time intervals. The water yield slightly increased from 9.8% over the fresh catalyst to 10.9% after 10 hours while the acetaldehyde yield increased with time on stream from 1.4% to 10% over the fresh catalyst and after 10 hours, respectively. The catalyst selectivity towards those by-products was also found to increase along the time intervals. Selectivity to CO was decreased from 14% to 9% along the investigated time intervals. This discussion proved that α-Fe_2O_3 phase catalyst was highly active towards ethanol partial oxidation reaction and produced hydrogen with high selectivity and low CO formation.

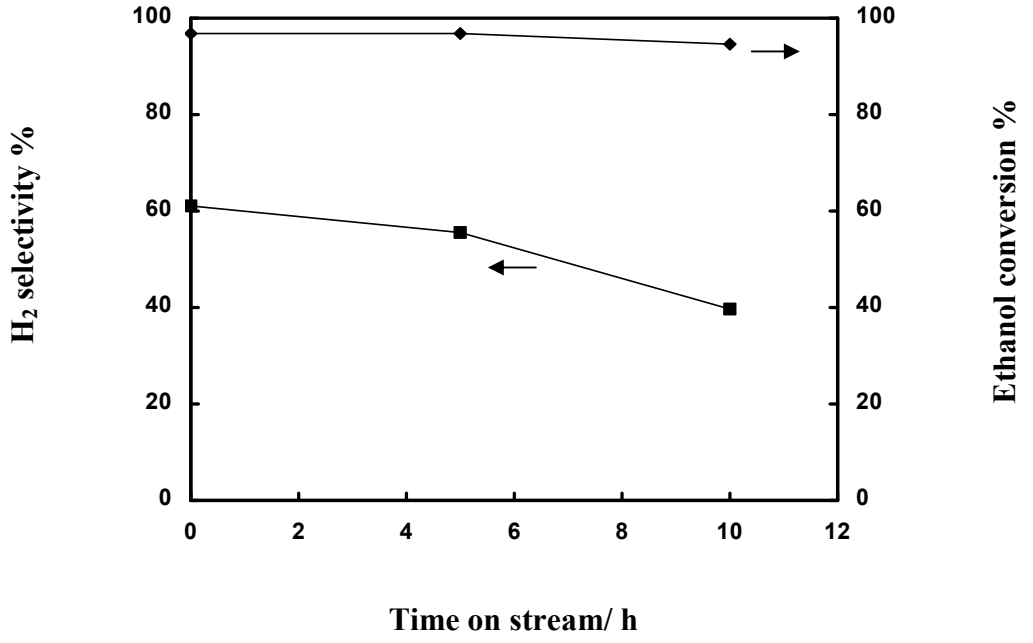

Figure 60: Effect of the time on stream on ethanol conversion and H_2 selectivity for ethanol partial oxidation over α-Fe_2O_3 at 270°C, an O_2/ethanol ratio of 1.0 and a catalyst surface area of 12 m^2

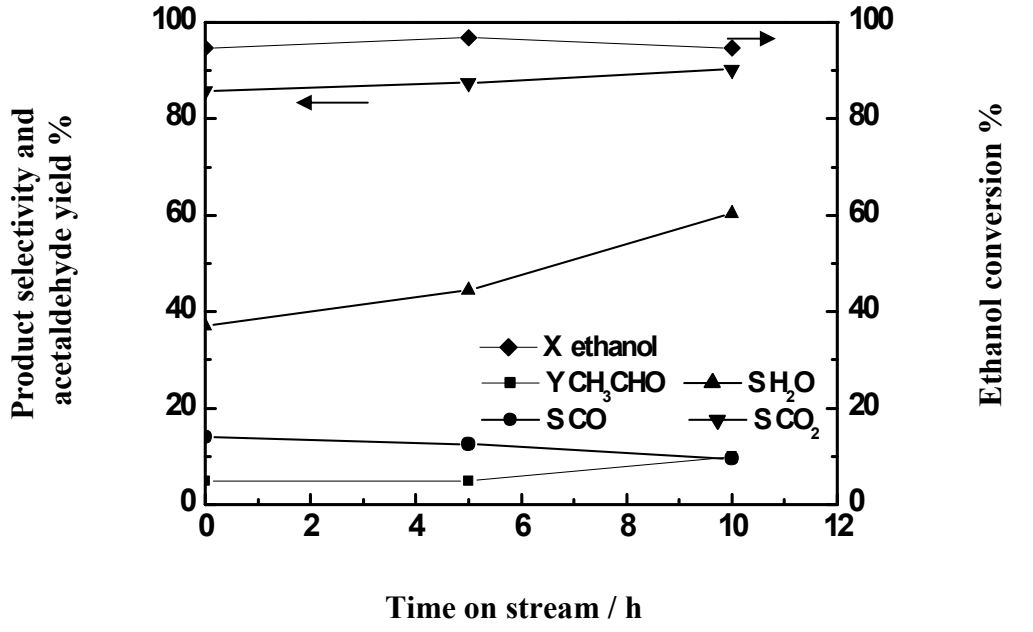

Figure 61: Effect of the time on stream on ethanol conversion, products selectivity and acetaldehyde yield for ethanol partial oxidation over α-Fe_2O_3 at an O_2/ethanol ratio of 1.0 and a catalyst area of 12 m^2

The catalyst, after 10 hours on stream, was again characterised using XRD and BET techniques to distinguish the change in structure and surface area that may occur to the catalyst during the reaction time. Figure 62 shows the XRD patterns for the used α-Fe_2O_3 for 10 hours in ethanol partial oxidation reaction. The diffractogram represents an XRD pattern of α-Fe_2O_3 which shows that the catalyst was not reduced to Fe_3O_4 (magnetite) during the catalytic reaction long run. It also confirms the results obtained for the catalytic activity since there was no sharp decrease towards hydrogen production or ethanol conversion with the time on stream due to the catalyst stability.

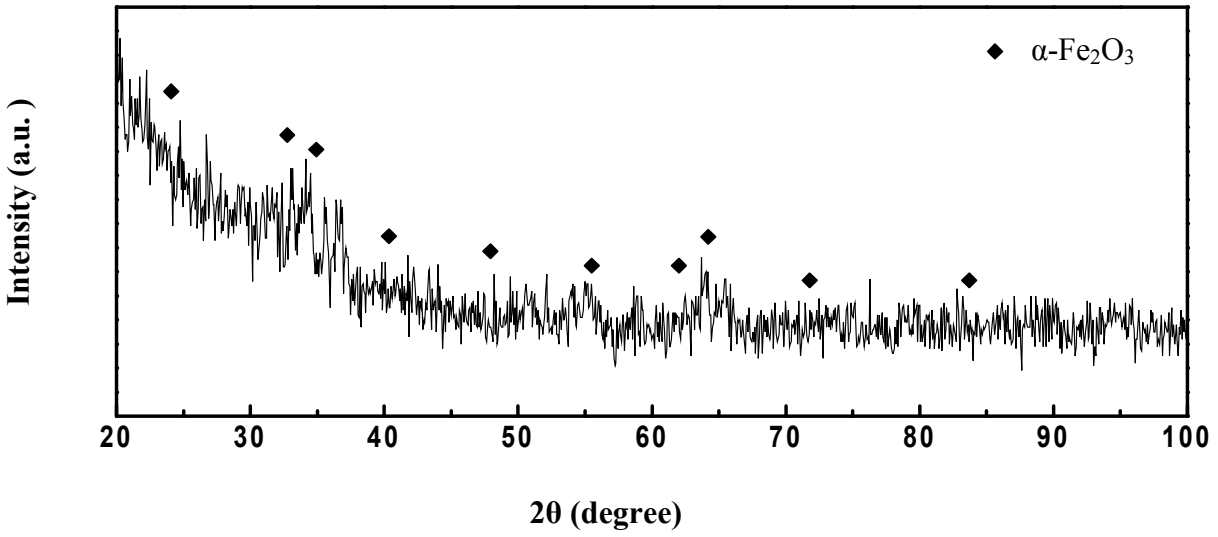

Figure 62: Powder X-Ray diffraction patterns of unsupported α-Fe_2O_3 used catalyst for 10 hours time on stream

The BET measurement for the used catalyst showed no significant change after the 10 hours time on stream since it was found to be 5.8 m^2/g for the used catalyst versus 6 m^2/g for the fresh one. The particle size change was accordingly not so significant since it changed from 10.3 nm to 12 nm what also proved that during reaction no agglomeration of the catalyst particles took place.

6.2.2.4. Catalytic activity of SiC support

It is useful to check the catalytic activity of SiC particles since it will be used as support for the iron oxide catalyst later on. This test will give information about whether the SiC particles themselves have a catalytic activity or not on the one hand, and on the other hand it will provide data on how far it will give a conversion and product distribution that has to be known for its effect on the iron oxide activity and selectivity. Before the SiC catalytic activity investigation, the physical and chemical

properties of the prepared SiC nanoparticles were characterised by XRD, SEM and EDX. Figure 63 shows the XRD result for SiC particles. The X-ray diffraction only showed a broad band in the range from 35° to 41° which is characteristic for β-SiC. The undetected sharp pattern may be explained by the amorphous structure and/or the small particle size of the prepared particles. Many authors [128, 131-133] reported the formation of the amorphous phase of SiC on the conditions used in this work. The N_2 adsorption isotherm for the as prepared particles was measured and the BET surface area (S_{BET}) of 171 m^2/g was obtained.

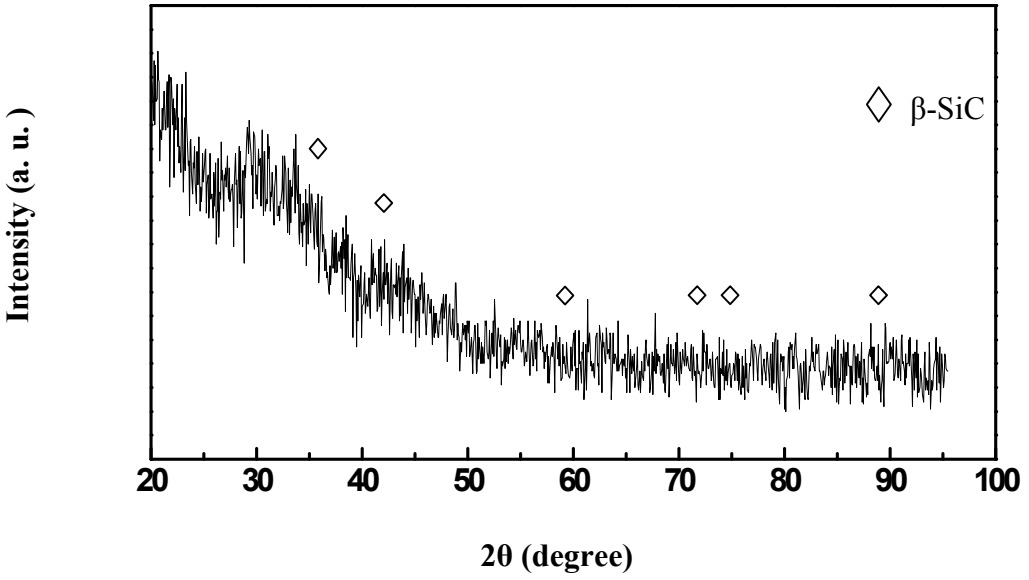

Figure 63: Powder X-ray diffraction patterns of SiC fresh catalyst

To obtain information about the morphology and particle size of the SiC particles, the SEM image was chosen. Figure 64 shows the SEM of as prepared SiC particles. The image indicates a random particle distribution in the sample. The figure also shows a uniform sample that appeared from the homogenous particles shape and size. Further, it shows a narrow particle size distribution ranging from 4 to 7 nm.

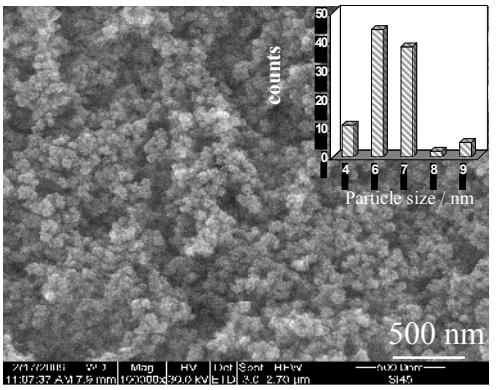

Figure 64 SEM image of SiC fresh sample. The insert show the particle size distribution

The study of the prepared SiC particles catalytic activity towards ethanol partial oxidation on optimum conditions investigated before resulted in no ethanol conversion. As proved, the SiC particles are chemically inert material and only used for thermal stability or to enhance the catalytic activity of the active phases [129]

6.3. Comparison between the unsupported catalysts

The catalytic activity, selectivity and stability factors are the factors considered to compare the previous unsupported iron oxide catalysts with different phases towards the ethanol partial oxidation. Experiments for the catalytic activity were investigated on the same condition, i.e. at a reaction temperature of 270^{o}C and an O_2/ethanol ratio of 1.0, using different catalyst weights for the different catalysts which were equivalent to a catalyst total area of 12 m^2 for one hour. For stability tests, the catalyst was subjected to ethanol oxidation for 10 hours. Then the catalytic activity and catalyst characterisation were carried out. From the previous discussion for unsupported catalysts, the catalysts selectivity towards the different products over iron oxide catalysts found to be dependent on the catalyst phase. Figure 65 indicates the effect of different phases on ethanol conversion and selectivity to H_2, H_2O, CO and CO_2 for the different iron oxide phase catalysts. It is found that the catalysts activity towards ethanol oxidation followed the order of α/γ-Fe_2O_3 > γ-Fe_2O_3 > α-Fe_2O_3. Ethanol conversions were 99.9, 97.1, and 95.2% for α/γ-Fe_2O_3, γ-Fe_2O_3 and α-Fe_2O_3, respectively. The slightly higher catalytic activity for the mixed phase iron oxide may be attributed to the fact that it provides more active sites allowing more ethanol to be oxidised and thus enhancing the conversion.

For hydrogen selectivity, it was found that the hydrogen production depends on the iron oxide catalyst phase. Among the different phases, α/γ-Fe_2O_3 showed a selectivity of 72.5% which is the highest selectivity recorded, while γ-Fe_2O_3 showed a hydrogen selectivity of 54.7%, and 61% was obtained for α-Fe_2O_3 on the same conditions. This high selectivity towards hydrogen production attributed to the side reactions occurs over α/γ-Fe_2O_3 surface. These side reactions include reverse water gas shift reaction and methane reforming. In these reactions, the formed water from the ethanol oxidation reform methane to carbon monoxide and hydrogen and convert the formed carbon dioxide to hydrogen and carbon monoxide. These side reactions may also be enhanced by inversed amount of the mixed phase, while the reverse water gas shift and methane reforming reactions are limited over the other phases.

The methane reforming with the formed water can be proved by the lowest calculated water selectivity over the α/γ-Fe_2O_3.

Comparing the other two iron oxide phases, Figure 65 shows that α-Fe_2O_3 possesses a higher hydrogen selectivity than γ-Fe_2O_3. The hydrogen selectivity, for example, was found to be 54.7% and 61% for γ-Fe_2O_3 and α-Fe_2O_3, respectively. This observation agrees with the literature cited for different metal supported Fe_2O_3. Horva´th *et al.* [156] reported for Au/Fe_2O_3 catalysts that the phase of iron oxide played an important role in the catalytic oxidation of CO. He claimed that the most active catalyst is the one which contains Fe_2O_3 in the alpha phase (hematite). Selectivity to CO was also found to be phase dependent. CO selectivity follows the order of γ-Fe_2O_3 > α/γ-Fe_2O_3 > α-Fe_2O_3. For instance, the selectivity was 36.7% over γ-Fe_2O_3 catalyst, 30.4 over α/γ-Fe_2O_3 whereas it decreased dramatically to 15.4 % over α-Fe_2O_3. In contrast, CO_2 selectivity increased in the order of α-Fe_2O_3 > α/γ-Fe_2O_3 > γ-Fe_2O_3.

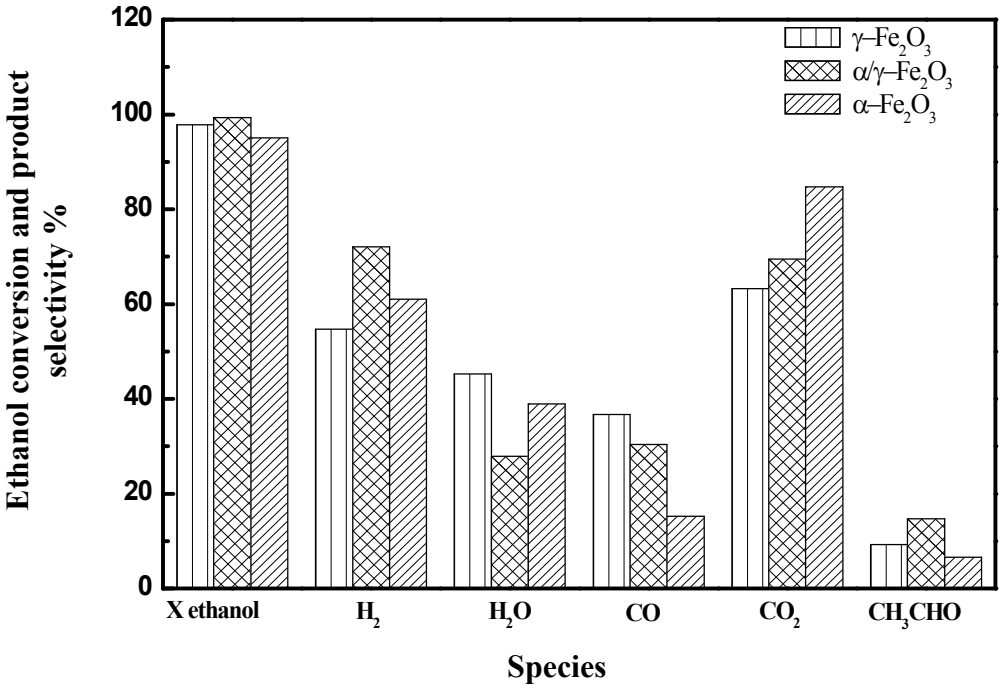

Figure 65: Comparison for ethanol conversion and products distribution over γ-Fe_2O_3 catalyst (240m^2/g), α/γ-Fe_2O_3 (160 m^2/g) and α-Fe_2O_3 (6 m^2/g) at a reaction temperature of 270°C, an O_2/ethanol ratio of 1.0 over a catalyst area of 12 m^2

These results for CO_2 and CO selectivity over α-Fe_2O_3 catalyst surface indicates that the α-phase plays an efficient role in converting CO into CO_2 and H_2 production by WGS, as the selectivity for H_2 and CO_2 increased while the selectivity for CO

decreased. Hutchings et al. [157] studied CO oxidation over Au/Fe_2O_3 and concluded that the Fe_2O_3 catalyst support plays a vital role in CO oxidation. The α-Fe_2O_3 (hematite) acts as an active phase for this reaction, where the Au catalysts cause a transformation from disordered nanocrystalline iron oxyhydroxide to hematite. Those results obtained from the catalytic activity were also confirmed by studies of the reaction kinetics to that effect that the initial rate constant for the ethanol partial oxidation reaction was determined and compared over all catalysts at the same temperatures ranging from 260°C to 290°C and O_2/ethanol ratio of one. The rate constant k for the reaction at each temperature was calculated by plotting the square root of initial hydrogen partial pressure against the time. The slope in s^{-1} for the initial hydrogen pressure curve was taken for the points from 0 to about 300 seconds from the beginning of reaction since it was the most linear section in the curve. The calculation of the slope of this line gave the rate constant. Figure 66 shows the Arrhenius plot of log k versus 1/T for γ-Fe_2O_3 and α/γ-Fe_2O_3. It is clear from the figure that the slope of the straight line for γ-Fe_2O_3 is higher than that for α/γ-Fe_2O_3, which reflects the higher initial rate of hydrogen formation over α/γ-Fe_2O_3 catalyst.

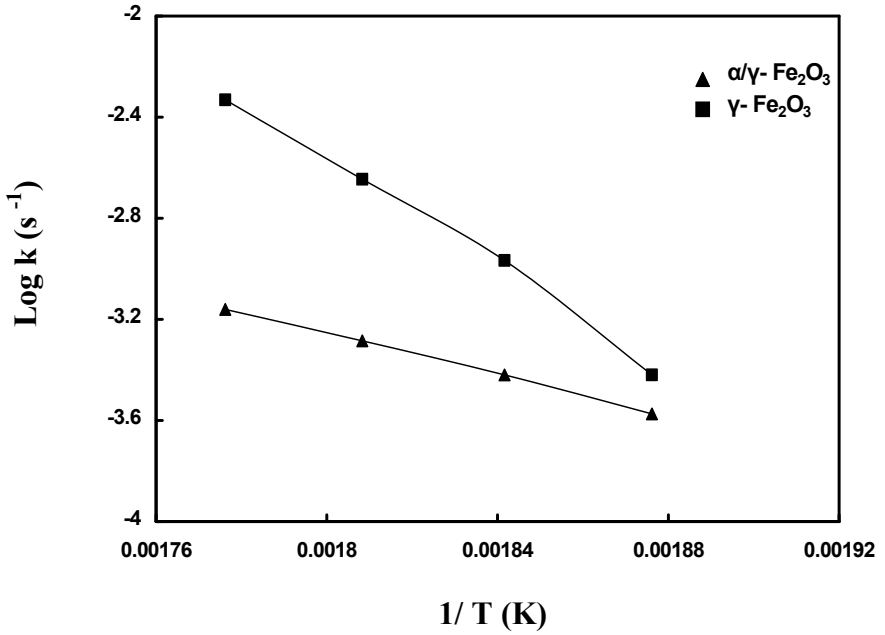

Figure 66: Arrhenius plot for ethanol partial oxidation reaction over γ-Fe_2O_3 and α/γ-Fe_2O_3 catalysts using O_2/ethanol of 0.5 over a catalyst area of 12 m^2

The activation energy was derived from the slope of the straight lines for both catalysts derived from the Arrhenius plot and found to be 87.63 and 33.57 kJ mol^{-1} for γ-Fe_2O_3 and α/γ-Fe_2O_3, respectively.

In spite of a higher surface area for γ-Fe_2O_3 (240 m^2/g) than for α/γ-Fe_2O_3 (160 m^2/g), the α/γ-Fe_2O_3 showed a lower rate constant and activation energy by almost the half of γ-Fe_2O_3. These results prove that the α/γ-Fe_2O_3 mixed phase catalyst is more active towards hydrogen production than the γ-Fe_2O_3 catalyst which agreed with the experimental results shown in Figure 65. Although the α/γ-Fe_2O_3 catalyst showed the highest ethanol conversion and selectivity to hydrogen production, it seems to be fast reduced to crystalline magnetite after 5 hours of reaction as indicated in Figure 55.

Although the α-Fe_2O_3 catalyst produced a lower hydrogen yield and showed lower conversion than α/γ-Fe_2O_3 but, in contrary, α-Fe_2O_3 still has the advantage of inability to oxidation along the investigated time on stream experiments, since the hematite is a stable phase, as can be indicated from Figure 62. It also did not show a really significant difference in ethanol conversion or hydrogen selectivity to α/γ-Fe_2O_3.

Again α-Fe_2O_3 showed 6% higher hydrogen selectivity than γ-Fe_2O_3 and almost the same ethanol conversion over the fresh sample catalyst. Moreover, the catalysts analysis after 10 hours on stream supports the idea of the α-Fe_2O_3 catalyst being the most active catalyst. The BET surface area for γ-Fe_2O_3 decreased from 240 m^2/g assigned to the fresh catalyst to 80 m^2/g after 10 hours on stream, whereas the α/γ-Fe_2O_3 phase decreased significantly from 160 m^2/g, measured for the fresh sample catalyst, to 51.5 m^2/g after 10 hours of reaction. Inversely, the nano α-Fe_2O_3 catalyst surface area was not so much declined after 10 hours of reaction since it decreased from 6 m^2/g, measured for the fresh catalyst, to 5.8 m^2/g for the used catalyst.

The catalyst stability is another major factor to decide what the best catalyst among the catalysts used in this study is and which can be used to produce hydrogen via ethanol partial oxidation. Figure 67 compares the stability for α-Fe_2O_3 and γ-Fe_2O_3 catalysts after 10 hours on stream at a reaction temperature of 270^oC and an O_2/ethanol ratio of one over a catalyst area of 12 m^2 for each catalyst. Although both catalysts exhibit a high ethanol conversion and hydrogen selectivity, the hydrogen selectivity initially strongly declines with the time on stream over the γ-Fe_2O_3 catalyst, whereas α-Fe_2O_3 showed an almost constant ethanol conversion and a much smaller decrease in the hydrogen selectivity for the same time on stream period. Based on all these discussed results, the α/γ-Fe_2O_3 catalyst was recommended as the best catalyst if higher hydrogen selectivity is needed. Generally, the α-Fe_2O_3 phase would be the best to produce higher hydrogen selectivity with small CO production

for a long time during a stable active phase. These results for α-Fe_2O_3 meet the actual need industry is looking for to apply the ethanol oxidation process commercially.

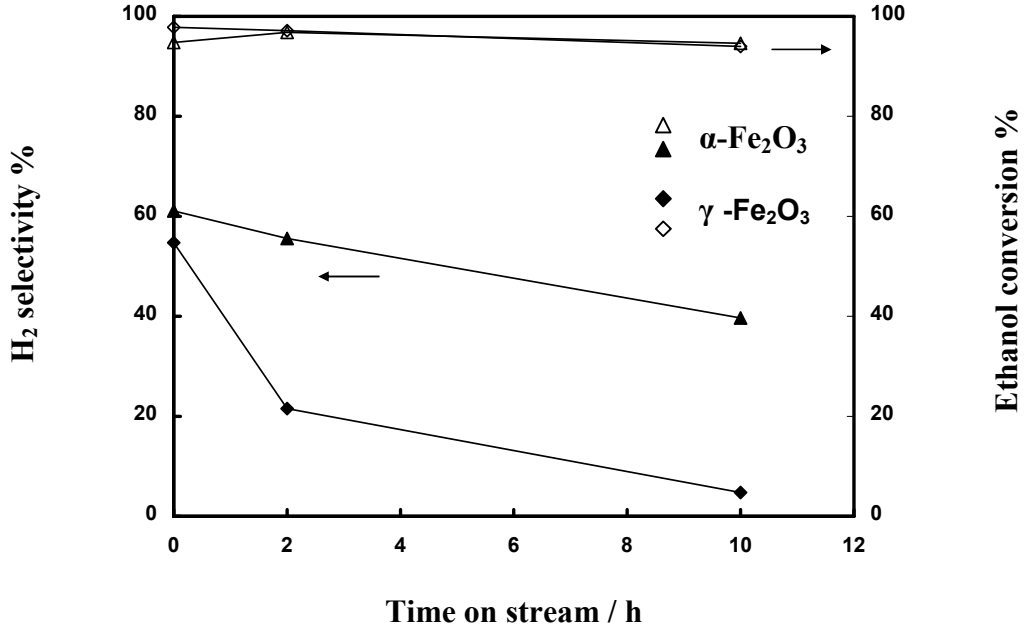

Figure 67: Effect of time on stream on ethanol conversion, H_2 selectivity for ethanol partial oxidation over α-Fe_2O_3 and γ-Fe_2O_3 at a reaction temperature of 270 ^oC, O_2/ethanol molar ratio of 1.0 and a catalyst area of 12 m^2 for

Further experiments were carried out to check out the effect of support on the catalytic activity of hematite through the investigation of ethanol partial oxidation reaction over the α-Fe_2O_3/SiC catalyst system.

6.4. Supported catalysts activity towards ethanol oxidation

6.4.1. Catalyst characterisation

The phase and structure of the prepared particles were identified by X-ray diffraction (XRD). Figure 68 shows the XRD patterns of the prepared α-Fe_2O_3, SiC and α-Fe_2O_3/SiC particles as well. The patterns shown in Figure 68a at 33.18^o and 35.5^o characterises the pure α-Fe_2O_3 phase. Figure 68b shows broad peaks at 35.5, 41 and 72 which characterise β-SiC. The broad peaks are attributed to amorphous particles and/or a small particle size. The other XRD charts were given for the supported catalysts. The disappearance of the iron oxide peaks in the supported samples may be explained by the high dispersion of α-Fe_2O_3 in the β-SiC support.

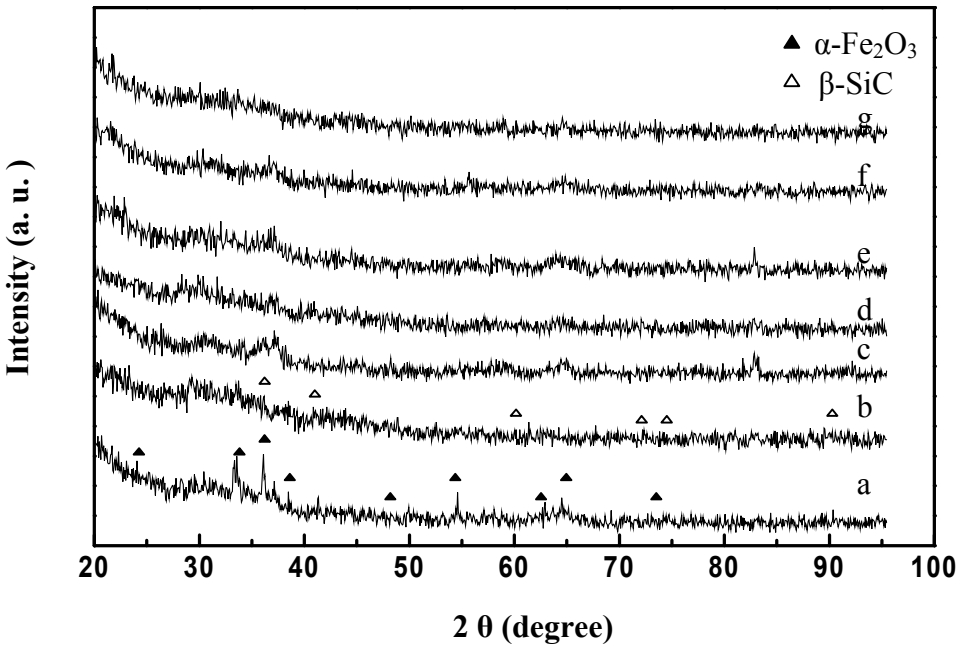

Figure 68: XRD patterns of; a) α-Fe_2O_3; b) silicon carbide support and α – Fe_2O_3/SiC with an iron content of c) Fe $_{1.9}$; d) Fe $_{2.3}$; e)Fe $_{7.1}$; f) Fe $_{9.2}$ and g) Fe $_{13.4}$

The morphology of particles was investigated by HRTEM. Figure 69 shows the TEM images for the supported iron oxide particles from which crystalline iron oxide can be seen over the amorphous SiC.

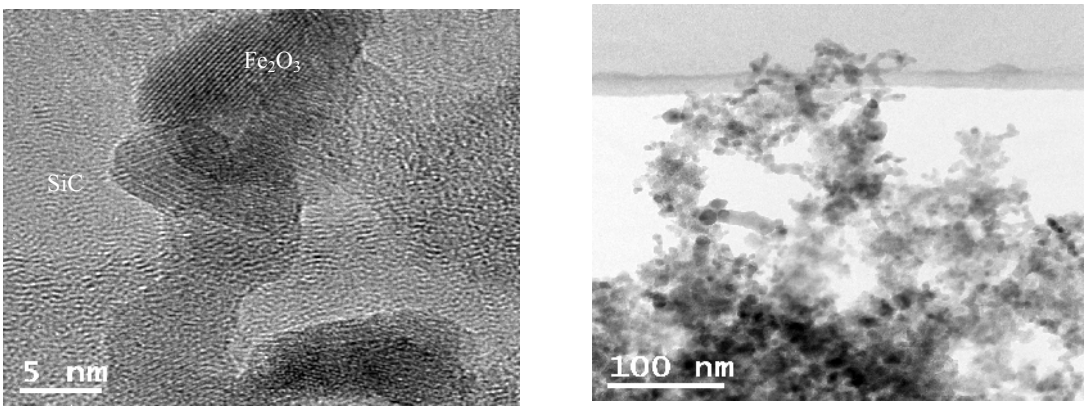

Figure 69: TEM image of α–Fe_2O_3/SiC fresh catalyst with Fe 9.2% prepared by CVS using TMS precursor for SiC and ferrocen for α–Fe_2O_3**.**

The HRTEM images proved the samples nanoscale particle size. Results for the chemical composition detected by EDX are shown in Table 5. The EDX detected Si and carbon atoms with almost 1:1 atomic percent also showed the Fe and O atomic percent equivalent to Fe_2O_3 composition. Amorphous carbon was seen in some other places. It is indicated that particles have a high oxygen content which may be explained by silica formation. Klein *et al*. [128] also showed a graphite deposition

over amorphous β-SiC at a lower pressure of 5 kPa. These observations were also reported by other authors [125, 126, 133] on similar deposition conditions. Table 2 summarises the measured atomic percent for each component of the supported catalyst series. In this catalyst series, the catalysts were given the symbols of Fe_x where X represents the iron content in the sample obtained from the EDX analysis.

Table 5: EDX analysis for the chemical composition of the prepared α-Fe_2O_3/SiC series

	SiC	Fe_2O_3	Fe 1.9	Fe 2.4	$Fe_{7.2}$	$Fe_{9.1}$	$Fe_{13.4}$
C %	41	---	28.62	27.65	43.99	28.69	36.33
O %	29	58.73	46.78	52.17	44.68	43.77	43.31
Si %	29	---	22.7	17.76	4.13	18.39	6.93
Fe %	---	41.27	1.91	2.42	7.21	9.16	13.42

Additional information on the Fe_2O_3/SiC structure can be achieved by X-ray photoelectron spectroscopy (XPS) analysis. XPS can be used to confirm the chemical composition and the oxidation state for both Fe_2O_3 and SiC. The measurement was performed for the sample catalysts with 9.4 % iron content as an example for the catalyst series using pass energy of 44eV. The results of XPS measurements are shown in Figure 58. Studying the 2p core level of iron oxide resulted in the appearance of two bands at 710.8 and 728 eV binding energy which was assigned to Fe $2p_{3/2}$ and Fe $2p_{1/2,}$ respectively. Those two peaks prove the presence of Fe^{3+} in Fe_2O_3 [158, 159]. Another small band appeared at around 718 eV, 732 eV and 741 eV which are characteristic bands for Fe_2O_3 [160], the measured band at 709.4 eV is a characteristic band for Fe-O-Si bridges [161]. Hawn et al.[159] compared the XPS spectra for iron metal and different iron oxide. According to him, the alpha phase shows small bands at 718.8, 732 and 741; however they do not appear in iron metal or in the magnetite phase. For SiC support, XPS was carried out at higher pass energy of 90 eV.

The results of XPS at the given higher binding energy are represented in Figure 59. The results show two bands at 58.3 and 95.8 which are assigned to Fe 3s and Fe3p, respectively. In contrast, sharp bands with high intensity appeared at 106.6 eV and 156.6 eV binding energies which were assigned to Si 2s and Si 2p respectively [162-164].

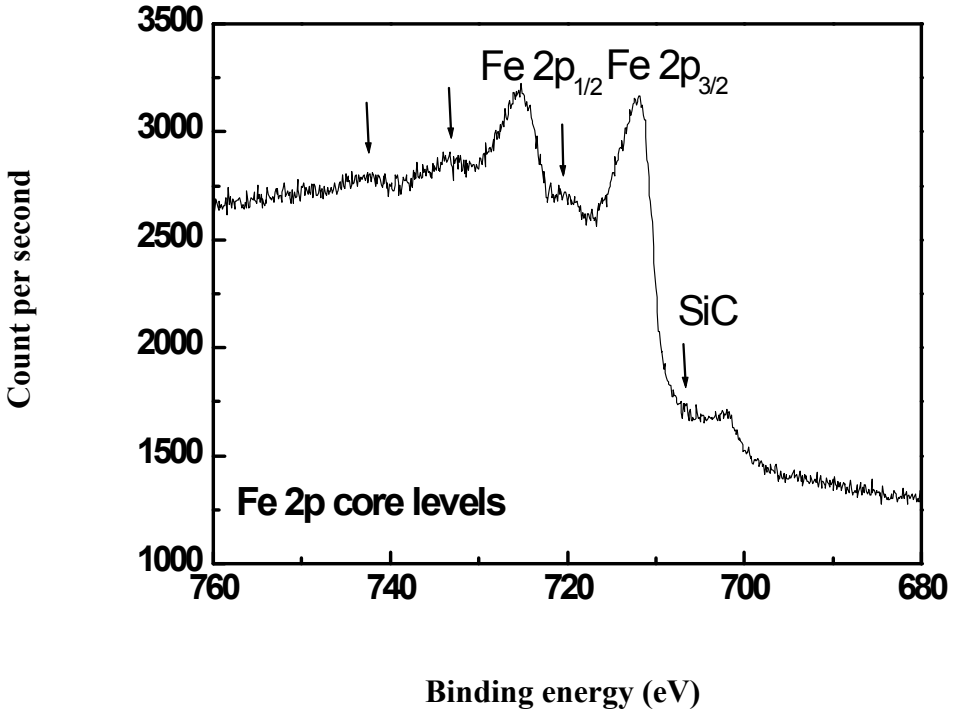

Figure 70: Fe 2p core level X-ray photoelectron spectroscopy (XPS) spectra of iron oxide supported nanoparticles.

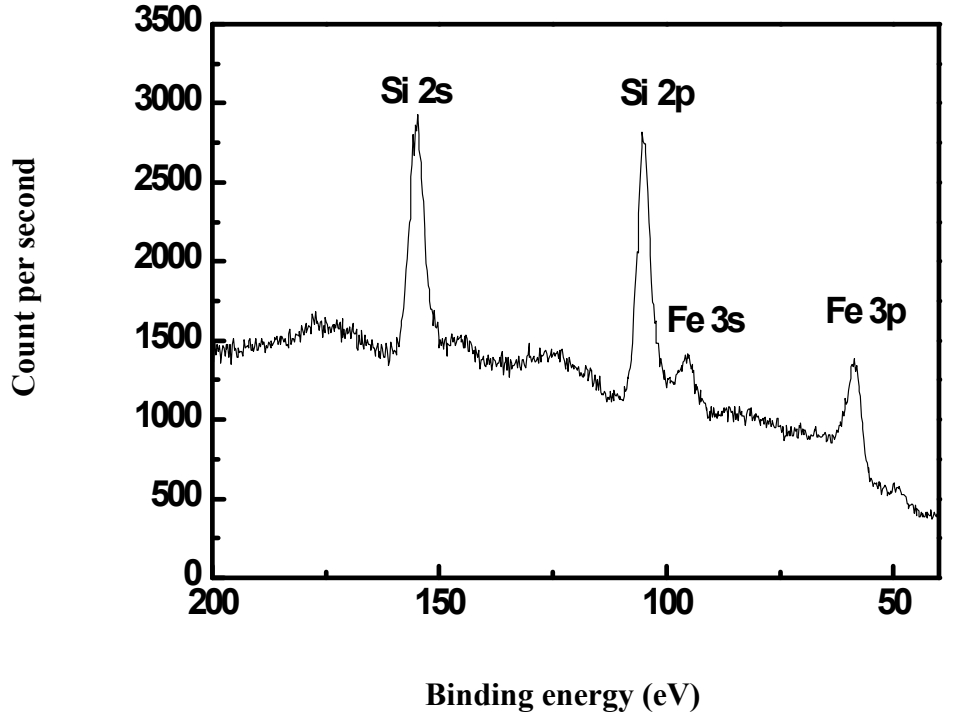

Figure 71: Si 2p core level X-ray photoelectron spectroscopy (XPS) spectra of iron oxide supported nanoparticles.

Table 6 summarises the physical properties of all prepared particles. The particle size for the supported samples was determined using BET and DLS techniques. The particle size found to be within a range from 6 to 15 nm. With increasing iron oxide content, the BET of samples decreased due to the loading with iron oxide of larger particle size. The table shows no significant difference in particle size measured by both methods. The larger particle size calculated by the BET may be explained by measuring the N_2 adsorption over agglomerates which is not found by the DLS technique due to ultrasonication made before measurement.

Table 6: Physical characterisation of SiC supported iron oxide catalyst series

Catalysts	Fe %	S_{BET} m^2/g	Particle size/ nm	
			DLS	BET
SiC	0	171	---	5
α –Fe_2O_3	41.5	6	10.7	12
Fe $_{1.9}$	1.9	193	9.3	5.6
Fe $_{2..3}$	2.3	138	9.7	9.36
Fe $_{7.2}$	7.2	105	10.5	12.2
Fe $_{9.16}$	9.16	94	12.8	14.5
Fe $_{13.2}$	13.2	87	14.6	15.7

For more information about how the atoms are bonded together in the samples, the functional groups in the sample were studied using Fourier transformation infrared spectroscopy (FTIR). Figure 72 presents the FTIR analysis for the catalyst series. The low frequency bands at about 450 cm^{-1} are assigned to Si-O-Si stretching vibration while the high frequency band from 500 to 750 cm^{-1} is ascribed to Fe-O stretching vibration from α-Fe_2O_3. The band shown from 800 to 900 cm^{-1} represents the interference of two peaks assigned to Si-O-Fe vibrations [119] and transversal optic (TO) mode Si–C vibrations (793 cm^{-1}) [165].

The broad band from 1000 to 1200 cm^{-1} is assigned to Si-O and Si-O-C stretching [162]. With increasing iron content, the transmittance intensity of Si-O-Si meanwhile decreased and the peaks for Si-O-Fe and Fe-O became sharper.

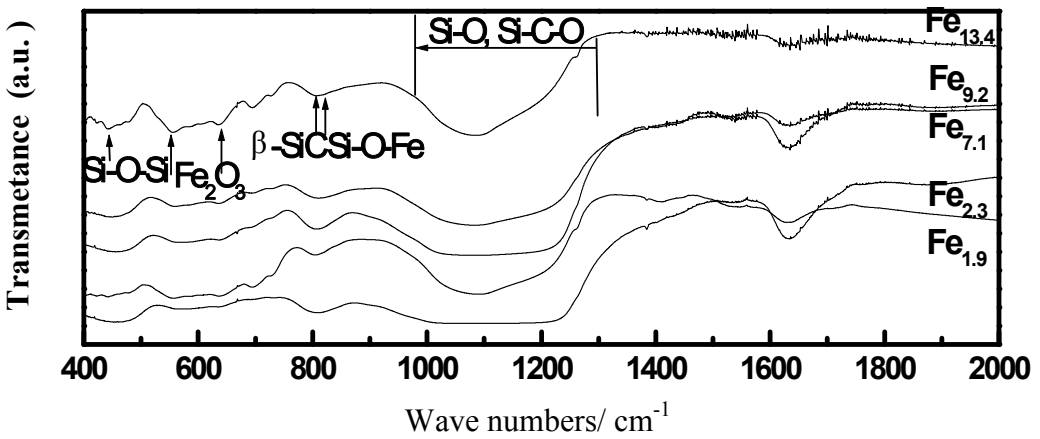

Figure 72: FTIR spectra of prepared catalysts with different iron content of a) 1.9 %, b) 2.3 %, c) 7.2 %, d) 9.1% and e) 13.2%

6.4.2. Catalytic activity

The ethanol partial oxidation reaction was used to investigate the catalytic activity of Fe_2O_3/SiC series catalysts. By applying the Fe_2O_3/SiC catalysts, the initial main products were acetaldehyde and water with a low combustion by-product of CO and CO_2. Figure 73 shows the comparison between the catalytic performances of the fresh catalyst series for POE on optimum reaction conditions found for the unsupported catalysts. The figure shows that the ethanol conversion increased with increasing iron content. With increasing iron content, the acetaldehyde yield obviously decreased accompanied by increasing selectivity to CO_2 and water. The highest yield of acetaldehyde of 56.8 % was found for the lowest iron content catalyst with a lower production of CO and CO_2. Water production increased up to 35.5 % over the highest iron content catalyst. CO_2 production increased from 7.3 % to 29 % while CO decreased from 21.4 % to about 8%. In combination of the blank run for SiC support with those observations, this proves that the ethanol oxidation occurred over the surface of the iron oxide and Fe_2O_3-SiC support interface which increased by increasing the iron oxide content. It could also be indicated from literature about the ethanol oxidation mechanism [32, 39, 92] that at low iron content the process of ethanol dehydrogenation to acetaldehyde is favoured.

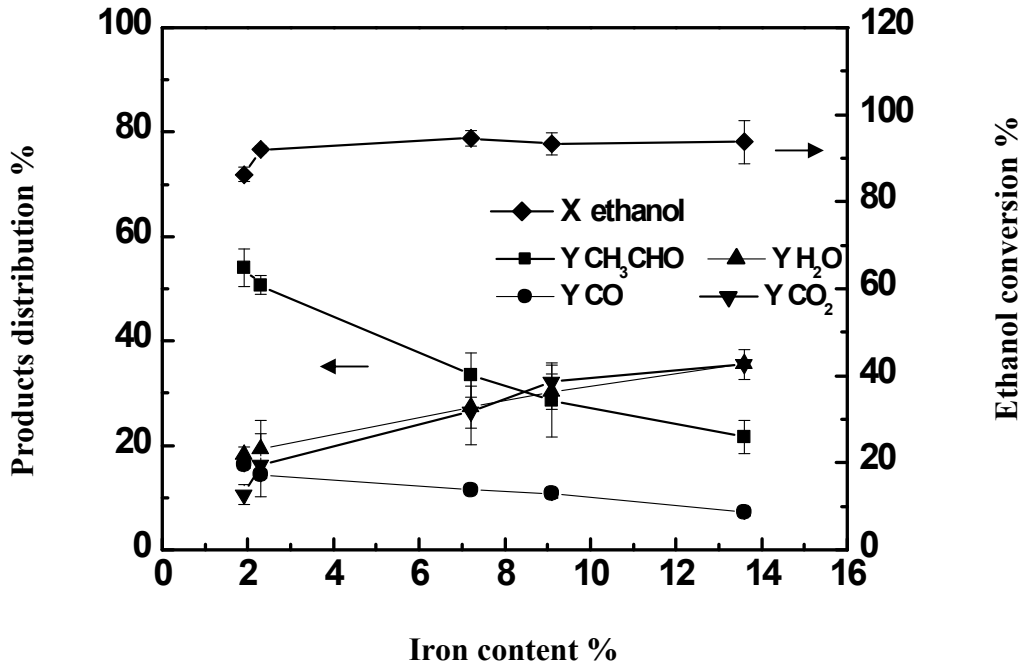

Figure 73: Effect of iron content on ethanol conversion and products yield for ethanol partial oxidation over different α-Fe_2O_3/ SiC catalysts at Temp. = 270°C, O_2/ ethanol = 1 and surface area = 12 m^2 for a reaction time of 1 hour

While higher iron content allows a higher catalyst area and iron-support interface, a higher catalytic activity is provided, and the process is continued to dehydrogenate the acetaldehyde to another oxygenate intermediate which is later oxidised to acetic acid probably by iron oxide lattice oxygen. The formed acetic acid has the ability during the reaction to oxidise to a carbonate species which is then deoxygenated to produce CO_2. The ability of Fe_2O_3 to provide a lattice oxygen which increases the redox effect of iron containing catalysts has been explained before by some authors [104, 139]. According to Vedrine et al. [166], this oxygen lattice supply mechanism that was first proposed by Mars-van-Krevelen, is also shown for other materials such as CeO_2 [29] and ZrO_2 [95]**.** The other pathway of ethanol oxidation to methane and CO is only favoured for low iron content catalysts. This was proved by a higher formation of CO with lower iron oxide content catalysts. The absence of hydrogen may be explained by oxidation of formed hydrogen to water what is proved by the linear increase of water selectivity.

In order to investigate how far the POE reaction is affected by the iron content, the reaction was carried out over an unsupported α-Fe_2O_3 with different catalyst areas. Those areas were typically 0.6 m^2 corresponding to the iron area of the supported

catalyst with 9.1% iron content and 12m^2 corresponding to the unsupported iron oxide catalysts. Figure 74 shows the ethanol conversion ($X_{ethanol}$) and product yield in the outlet stream.

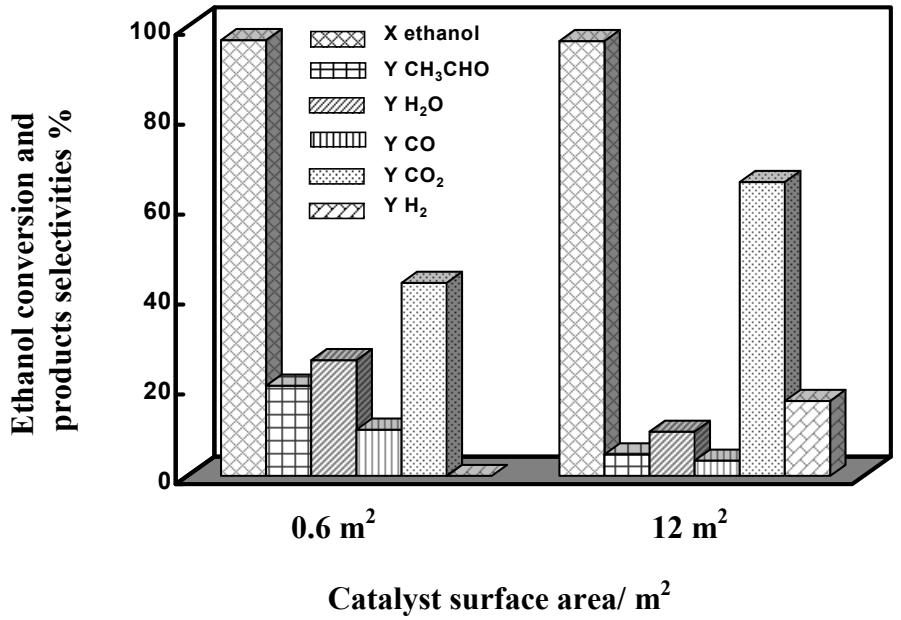

Figure 74: Products distribution obtained at a reaction temperature of 270^{o}C and an O_2/ethanol ratio of 1.0 for ethanol partial oxidation over α–Fe_2O_3 catalyst with different surface areas for a reaction time of 1 hour

The results show that with a higher catalyst surface area, ethanol is oxidised to acetaldehyde which is further oxidised to produce a significant yield of hydrogen and carbon dioxide. This pathway can be supported by the high CO_2 and reasonable hydrogen yields with lower acetaldehyde yield formed over the higher iron content samples. This may be attributed to the high surface area what means that a higher iron content allows the acetaldehyde to be re-adsorbed on the catalyst and dehydrogenated to some oxygenates and then the carbon oxygenates formed oxidizes leading to a high CO_2 yield.

6.4.3. Catalyst stability

The stability test was conducted for POE over all supported catalysts at 270^{o}C and an O_2/ethanol ratio of 1.0 over a catalyst area of 12 m^2 for 10 hours. Figure 75 shows the ethanol conversion over the used catalyst surface and acetaldehyde yield in the outlet stream as a function of the POE reaction time. The ethanol conversion decreased slightly by maximum 9 percent with point's time. The catalysts found to be active to initially produce the same amount of acetaldehyde while its yield of all

catalysts appeared to have increased with increasing iron oxide along the time on stream due to the decrease of ethanol conversion.

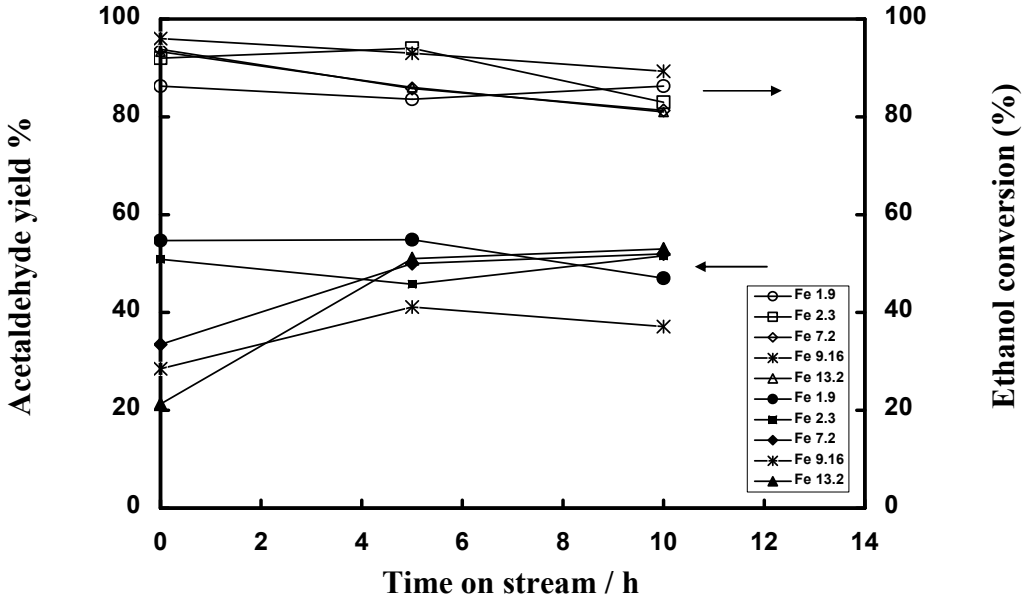

Figure 75: Effect of the time on stream on the acetaldehyde yield formed by ethanol partial oxidation over different α-Fe_2O_3/SiC catalysts at a reaction temperature of 270°C and an O_2/ethanol ratio of 1.0 over a catalyst area of 12 m^2

The figure shows that the catalyst series is strongly active along the investigated time on stream and that the acetaldehyde production does not change with time. The catalysts were then analysed to obtain information about how the reaction affected the physical and chemical properties of the catalysts. The XRD patterns of the used α-Fe_2O_3/SiC catalysts for POE after 10 hours showed no iron oxide characteristic peaks. The absence of the iron oxide diffraction peak indicates that no aggregation or sintering of iron oxide particles or oxidation to other phases along the reaction time took place. Nevertheless, it seems that the iron oxide-support interaction prevents iron oxide particles to be sintered on reaction conditions along the reaction time.

A good agreement with this observation is the small difference in particle size between the fresh (see Table 6) and the used catalysts (see Table 7), measured by dynamic light scattering (DLS) from the iron oxide. Table 7 provides information about the physical characterisation for the supported catalysts after 10 hours on stream. The figure indicates a significant decrease of the BET surface area and an increase in the particle size after 10 hours of reaction compared with BET and the surface area for the fresh catalysts (see Table 6). This may be attributed to sintering of SiC nanoparticles or deposition of carboneous materials on the surface of SiC support.

The table also shows the iron content for the supported catalysts which were measured using the EDX analysis tool.

Table 7: Physical characterisation of the α-Fe_2O_3/SiC catalyst series after 10 hours of reaction

Catalysts	Fe %	BET m^2/ g	Particle size/ nm	
			DLS	BET
SiC	0	170	---	4.9
α – Fe_2O_3	41.8	5.8	11	---
Fe $_{1.9}$	1.9	132.2	10.36	12
Fe $_{2..3}$	2.3	65.5	10.88	12
Fe $_{7.2}$	7.2	87	11.56	23
Fe $_{9.16}$	9.16	72.3	13.33	25
Fe $_{13.2}$	13.2	51	14.78	37

The bigger size shown by BET may be explained by measuring the N_2 adsorption for the agglomerates produced by support sintering. However, in case of the DLS technique, the agglomeration was not found due to ultrasonication made before measurement for the catalyst sample.

To prove that iron oxide is not sintered on reaction conditions, a HRTEM image for the used supported catalyst was taken and represented in Figure 76. The figure shows the small particle size for the crystalline iron oxide with no visible change compared to the fresh catalyst SEM image (see page 103). This agrees with particle size measurement using DLS technique.

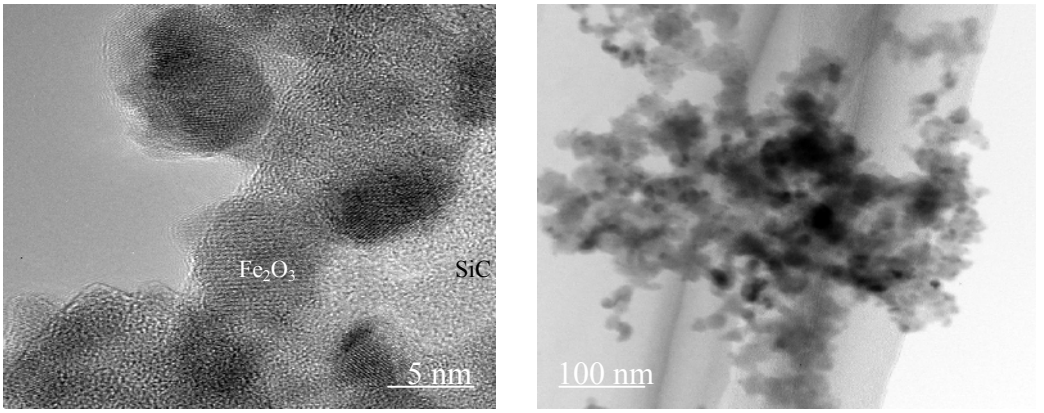

Figure 76: **TEM image of α–Fe_2O_3/SiC used catalyst with an iron content of 9.2%**

Cei *et al*. [84] investigated the ethanol oxidation via steam reforming, partial oxidation and oxidative steam reforming methods over Ir/CeO_2. According to him, the catalyst was stable for 60 hours of time on stream. The catalyst was then analysed

after those 60 hours by XRD and SEM. The XRD showed an absence of Ir peak. The HRTEM showed the dispersed Ir with particle size in a range from 2 to 3 nm which was the particle size for the fresh sample. The HRTEM also showed that the ceria particles with a larger particle size of 27nm after reaction. He attributed this to the high dispersion of Ir particles in ceria support preventing them from sintering while maintaining sufficient Ir-CeO_2 interface that provides oxygen to the system and inhibits the coke deposition.

CHAPTER 7
CONCLUSIONS

7. Conclusions

SiC, α-Fe_2O_3 and α-Fe_2O_3/SiC supported nanoparticles were prepared by the CVS process using a home-made hot wall reactor. The CVS was carried out at atmospheric pressure using a hot wall reactor (HWR) technique to avoid an expensive vacuum system. A new HWR setup was used successfully to produce the Fe_2O_3/SiC particles by introducing the reacting gases from both sides to a two different hot zone reactor. This setup could be later used to further produce other supported nanoparticles. It is concluded that the smallest SiC nanoparticles can be produced at a high temperature, low carrier gas flow and high diluent gas flow. The α-Fe_2O_3 can be produced from ferrocene precursor at 800^{o}C in an oxygen containing environment. All the findings represented in this wok indicate that unsupported iron oxide and SiC supported iron oxide catalysts are promising catalysts for ethanol partial oxidation on mild oxidation conditions, i.e. a reaction temperature of 270^{o}C and an O_2/ethanol ratio of 1:1. The catalytic performance of the unsupported iron oxide catalysts in the temperature range from 260°C to 290^{o}C suggests that the overall reactions involved are consecutive ethanol partial oxidation, steam reforming and water gas sift reaction. CO produced by ethanol oxidation is subsequently transformed into CO_2 by the water gas shift and CO oxidation reactions. The mixed phase unsupported iron oxide catalysts provide two types of active sites in this way enhancing the reformation of produced methane to hydrogen and CO. The performance of unsupported iron oxide catalysts for ethanol partial oxidation depends on the iron oxide phase. The α-Fe_2O_3 phase exhibits the best performance in comparison to the γ-Fe_2O_3 and the mixed α/γ-Fe_2O_3 catalysts. It has a high selectivity towards hydrogen production with a good stability. For SiC supported catalysts it was found that their activity depends on the iron oxide content. The catalysts showed a high selectivity towards acetaldehyde production with a high stability during the investigated time one stream. The catalysts showed a tendency to produce higher CO_2 and water yields with increasing iron content. The SiC support prevents the dispersed iron oxide nanoparticles to be reduced or sintered what, in turn, increases the catalyst life time.

PROSPECTIVE WORK

Prospective work

The fuel cell system offers a high potential for an efficient power generation and reduces emission of pollutants because hydrogen is used as fuel. Several routes for hydrogen production from ethanol have been studied. Partial oxidation of ethanol (POE) has been suggested as a suitable route for hydrogen extraction from ethanol. Previous studies on POE to produce hydrogen showed that ceria supported platinum and palladium catalysts are found to be the most active. This work showed that iron oxide, especially in the hematite phase, is also active towards the ethanol oxidation. Therefore, this work can be extended to study the ceria supported hematite catalyst system towards the POE process. It is further suggested to increase the iron oxide percent in the nano-Fe_2O_3/SiC catalyst system to increase the produced acetaldehyde oxidation rate to hydrogen and carbon dioxide.

Another idea for the future work is to develop an active and more stable catalyst for gas to liquid (GTL) process. GTL technology involves the conversion of methane into synthesis gas (H_2/ CO) and its posterior transformation into heavier hydrocarbons through the Fischer–Tropsch synthesis. However, one of the biggest disadvantages of the process is the high investment required to produce synthesis gas (syngas). The partial oxidation of methane (POM) has been considered as a good process in the production of syngas, specially in small reactors. However, to make this reaction economically viable, it is necessary to find catalysts with a high activity, selectivity and more important stability since several of them are deactivated by coke deposition. The catalysts suggested above can be investigated for this purpose since it is investigated for the same reasons in the POE process. Additionally, it is a cheap material and proved to be stable and completely active in the ethanol oxidation process.

REFERENCES

References

1. Farrauto, R.J., *Introduction to solid polymer membrane fuel cells and reforming natural gas for production of hydrogen.* Applied Catalysis B: Environmental, 2005. 56(1-2 SPEC. ISS.): p. 3-7.
2. Liguras, D.K., D.I. Kondarides, and X.E. Verykios, *Production of hydrogen for fuel cells by steam reforming of ethanol over supported noble metal catalysts.* Applied Catalysis B: Environmental, 2003. 43(4): p. 345-354.
3. Vaidya, P.D. and A.E. Rodrigues, *Insight into steam reforming of ethanol to produce hydrogen for fuel cells.* Chemical Engineering Journal, 2006. 117(1): p. 39-49.
4. Oetjen, H.F., et al., *Performance data of a proton exchange membrane fuel cell using H2/CO as fuel gas.* Journal of the Electrochemical Society, 1996. 143(12): p. 3838-3842.
5. J. Petrovic, J.M., P. Devlin, C. Read, Proceedings of the 2003 Fuel Cell Seminar, Miami Beach, FL, 2003: p. 988.
6. Joan M. Ogden, T.G.K.a.M.M.S., *Fuels for fuel cell vehicles.* Fuel Cells Bulletin 2000. 6: p. 5.
7. Velu, S., et al., *Selective production of hydrogen for fuel cells via oxidative steam reforming of methanol over CuZnAl(Zr)-oxide catalysts.* Applied Catalysis A: General, 2001. 213(1): p. 47-63.
8. Xu, W., et al., *New proton exchange membranes based on poly (vinyl alcohol) for DMFCs.* Solid State Ionics, 2004. 171(1-2): p. 121-127.
9. Xu, W., et al., *Low methanol permeable composite Nafion/silica/PWA membranes for low temperature direct methanol fuel cells.* Electrochimica Acta, 2005. 50(16-17): p. 3280-3285.
10. Dunn, S., *Hydrogen futures: Toward a sustainable energy system.* International Journal of Hydrogen Energy, 2002. 27(3): p. 235-264.
11. Wang, J., S. Wasmus, and R.F. Savinell, *Evaluation of ethanol, 1-propanol, and 2-propanol in a direct oxidation polymer-electrolyte fuel cell a real-time mass spectrometry study.* Journal of the Electrochemical Society, 1995. 142(12): p. 4218-4224.
12. Silva, A.M., et al., *Effect of the metal nature on the reaction mechanism of the partial oxidation of ethanol over CeO2-supported Pt and Rh catalysts.* Catalysis Today, 2008. 133-135(1-4): p. 755-761.
13. Breen, J.P., R. Burch, and H.M. Coleman, *Metal-catalysed steam reforming of ethanol in the production of hydrogen for fuel cell applications.* Applied Catalysis B: Environmental, 2002. 39(1): p. 65-74.
14. Fatsikostas, A.N., D.I. Kondarides, and X.E. Verykios, *Steam reforming of biomass-derived ethanol for the production of hydrogen for fuel cell applications.* Chemical Communications, 2001(9): p. 851-852.
15. Llorca, J., et al., *Direct production of hydrogen from ethanolic aqueous solutions over oxide catalysts.* Chemical Communications, 2001(7): p. 641-642.
16. de Lima, S.M., et al., *Steam reforming, partial oxidation, and oxidative steam reforming of ethanol over Pt/CeZrO$_2$ catalyst.* Journal of Catalysis, 2008. 257(2): p. 356-368.
17. Liberatori, J.W.C., et al., *Steam reforming of ethanol on supported nickel catalysts.* Applied Catalysis A: General, 2007. 327(2): p. 197-204.

18. Xi, J.Y., et al., *Investigation of partial oxidation of ethanol to hydrogen over CuZnNi catalysts.* J Mol Catal (China), 2001. 15: p. 255–258.
19. W. Wang, Z.W., Y. Ding and G. Lu, Chemical Research China University 2003. 19: p. 206.
20. Liguras, D.K., K. Goundani, and X.E. Verykios, *Production of hydrogen for fuel cells by catalytic partial oxidation of ethanol over structured Ni catalysts.* Journal of Power Sources, 2004. 130(1-2): p. 30-37.
21. Velu, S., et al., *In situ XPS investigations of $Cu_{1-x}Ni_xZnAl$-mixed metal oxide catalysts used in the oxidative steam reforming of bio-ethanol.* Applied Catalysis B: Environmental, 2005. 55(4): p. 287-299.
22. Navarro, R.M., et al., *Production of hydrogen by oxidative reforming of ethanol over Pt catalysts supported on Al_2O_3 modified with Ce and La.* Applied Catalysis B: Environmental, 2005. 55(4): p. 229-241.
23. Fierro, V., et al., *Ethanol oxidative steam reforming over Ni-based catalysts.* Journal of Power Sources, 2005. 145(2): p. 659-666.
24. Zhang, B., et al., *Steam reforming of bio-ethanol for the production of hydrogen over ceria-supported Co, Ir and Ni catalysts.* Catalysis Communications, 2006. 7(6): p. 367-372.
25. Aupretre, F., et al., *Ethanol steam reforming over $Mg_xNi_{1-x}Al_2O_3$ spinel oxide-supported Rh catalysts.* Journal of Catalysis, 2005. 233(2): p. 464-477.
26. Fajardo, H.V. and L.F.D. Probst, *Production of hydrogen by steam reforming of ethanol over Ni/Al_2O_3 spherical catalysts.* Applied Catalysis A: General, 2006. 306: p. 134-141.
27. Wang, H., et al., *Steam reforming of ethanol over Co_3O_4/CeO_2 catalysts prepared by different methods.* Catalysis Today, 2007. 129(3-4): p. 305-312.
28. Fierro, V., et al., *Oxidative reforming of biomass derived ethanol for hydrogen production in fuel cell applications.* Catalysis Today, 2002. 75(1-4): p. 141-144.
29. Mattos, L.V. and F.B. Noronha, *Hydrogen production for fuel cell applications by ethanol partial oxidation on Pt/CeO_2 catalysts: The effect of the reaction conditions and reaction mechanism.* Journal of Catalysis, 2005. 233(2): p. 453-463.
30. Wang, H., Z. Jusys, and R.J. Behm, *Ethanol electrooxidation on a carbon-supported Pt catalyst: Reaction kinetics and product yields.* Journal of Physical Chemistry B, 2004. 108(50): p. 19413-19424.
31. De Souza, J.P.I., et al., *Electro-oxidation of ethanol on Pt, Rh, and PtRh electrodes. A study using DEMS and in-situ FTIR techniques.* Journal of Physical Chemistry B, 2002. 106(38): p. 9825-9830.
32. Song, S.Q., et al., *Direct ethanol PEM fuel cells: The case of platinum based anodes.* International Journal of Hydrogen Energy, 2005. 30(9): p. 995-1001.
33. Shao, M.H. and R.R. Adzic, *Electrooxidation of ethanol on a Pt electrode in acid solutions: In situ ATR-SEIRAS study.* Electrochimica Acta, 2005. 50(12): p. 2415-2422.
34. Camara, G.A. and T. Iwasita, *Parallel pathways of ethanol oxidation: The effect of ethanol concentration.* Journal of Electroanalytical Chemistry, 2005. 578(2): p. 315-321.
35. V. Schmidt, R.I., E. Pastor, S. Gonzales, Journal of Physical chemistry B:, 1996. 100: p. 17901.

36. Iwasita, T. and E. Pastor, *A DEMS and FTIR spectroscopic investigation of adsorbed ethanol on polycrystalline platinum.* Electrochimica Acta, 1994. 39(4): p. 531-537.
37. Pastor, E. and T. Iwasita, *D/H exchange of ethanol at platinum electrodes.* Electrochimica Acta, 1994. 39(4): p. 547-551.
38. Sheng, P.Y., et al., *H_2 production from ethanol over Rh-Pt/CeO_2 catalysts: The role of Rh for the efficient dissociation of the carbon-carbon bond.* Journal of Catalysis, 2002. 208(2): p. 393-403.
39. Costa, L.O.O., et al., *Partial oxidation of ethanol over Pd/CeO_2 and Pd/Y_2O_3 catalysts.* Catalysis Today, 2008. 138(3-4): p. 147-151.
40. Salge, J.R., G.A. Deluga, and L.D. Schmidt, *Catalytic partial oxidation of ethanol over noble metal catalysts.* Journal of Catalysis, 2005. 235(1): p. 69-78.
41. Cavallaro, S., et al., *Hydrogen production by auto-thermal reforming of ethanol on Rh/Al_2O_3 catalyst.* Journal of Power Sources, 2003.123(1):p. 10-16.
42. Nakanishi, M. and C. Bolm, *Iron-catalyzed benzylic oxidation with aqueous tert-butyl hydroperoxide.* Advanced Synthesis and Catalysis, 2007. 349(6): p. 861-864.
43. MartiÌ n, S.E. and A. Garrone, *Efficient solvent-free iron(III) catalyzed oxidation of alcohols by hydrogen peroxide.* Tetrahedron Letters, 2003. 44(3): p. 549-552.
44. Pierson, H.O., *Handbook of chemical vapor depostion [ie deposition](CVD): principles, technology, and applications*. 1999: William Andrew Publishing.
45. Smith, D.L., *Thin-film deposition: principles and practice*. 1995: McGraw-Hill Professional.
46. S. Yu-Sheng, a.Z.Y., *Fe_2O_3 Ultrafine Particle Thin Films are Prepared by MO-CVD Method," Proc. 10th. Int. Conf. on CVD, (G. Cullen, ed.).* Electrochem. Soc, 1987.
47. Melero, J.A., et al., *Nanocomposite of crystalline Fe2O3 and CuO particles and mesostructured SBA-15 silica as an active catalyst for wet peroxide oxidation processes.* Catalysis Communications, 2006. 7(7): p. 478-483.
48. Harris, G.L., *Properties of silicon carbide*. 1995: Inspec/Iee.
49. Choyke, W.J. and G. Pensl, *Physical properties of SiC.* MRS Bulletin, 1997. 22(3): p. 25-29.
50. Hao, Y.J., et al., *Synthesis and characterization of bamboo-like SiC nanofibers.* Materials Letters, 2006. 60(11): p. 1334-1337.
51. Changhong, D., et al., *The synthesis of ultrafine SiC powder by the microwave heating technique.* Journal of Materials Science, 1997. 32(9): p. 2469-2472.
52. Li, X.M., B.D. Eustergerling, and Y.J. Shi, *Mass spectrometric study of gas-phase chemistry in a hot-wire chemical vapor deposition reactor with tetramethylsilane.* International Journal of Mass Spectrometry, 2007. 263(2-3): p. 233-242.
53. Takao, S., et al., *MOCVD growth of spherical aggregates of SiC nanocrystallites.* Applied Surface Science, 2008. 254(23): p. 7630-7632.
54. Srikanth Vadali, V.S.S., et al., *Nanocrystalline diamond/[beta]-SiC composite interlayers for the deposition of continuous diamond films on W and Mo substrate materials.* Surface and Coatings Technology, 2007. 201(22-23): p. 8981-8985.
55. Berzelius, J., Fort. Physik Wissenshaft Tübingen 1836. 243.

56. Hagen, J., *Industrial catalysis: a practical approach*. 2006: Vch Verlagsgesellschaft Mbh.
57. Rothenberg, G., *Catalysis: concepts and green applications*. 2008: Vch Verlagsgesellschaft Mbh.
58. Richards, R., *Surface and nanomolecular catalysis*. 2006: CRC.
59. Thomas, J.M. and W.J. Thomas, *Principles and practice of heterogeneous catalysis*. 1997: Wiley-VCH.
60. Brunauer, S., P.H. Emmett, and E. Teller, *Adsorption of gases in multimolecular layers, 1938, J.* Amer. Chem. Soc, 1938. 60: p. 309-319.
61. Turns, S.R., *An introduction to combustion*. 1996: McGraw-Hill New York.
62. Mattos, L.V. and F.B. Noronha, *The influence of the nature of the metal on the performance of cerium oxide supported catalysts in the partial oxidation of ethanol.* Journal of Power Sources, 2005. 152(1-2): p. 50-59.
63. Wang, W., et al., *Partial oxidation of ethanol to hydrogen over Ni-Fe catalysts.* Catalysis Letters, 2002. 81(1-2): p. 63-68.
64. Shi, F., et al., *Nano-iron oxide-catalyzed selective oxidations of alcohols and olefins with hydrogen peroxide.* Journal of Molecular Catalysis A: Chemical, 2008. 292(1-2): p. 28-35.
65. Zhang, Z., C. Boxall, and G.H. Kelsall, *Photoelectrophoresis of colloidal iron oxides 1. Hematite (α--Fe_2O_3).* Colloids and Surfaces A: Physicochemical and Engineering Aspects, 1993. 73(C): p. 145-163.
66. Cornell, R.M. and U. Schwertmann, *The iron oxides*. 2003: Wiley-VCH Weinheim.
67. Eggleton, R.A. and R.W. Fitzpatrick, *NEW DATA AND A REVISED STRUCTURAL MODEL FOR FERRIHYDRITE.* Clays and Clay Minerals, 1988. 36(2): p. 111-124.
68. Lamber, R., N. Jaeger, and G. Schulz-Ekloff, *Microstructure Resulting from Metal-Support Interactions on Heterogeneous Catalysts.* Mikrostrukturen aus Metall/Traeger-Wechselwirkungsprozessen an heterogenen Katalysatoren, 1991. 63(7): p. 681-691.
69. Atkins, P.W., *Physical Chemistry. 5th.* Edition (Oxford University Press, Oxford, 1997).
70. Gross, M.L., *Mass spectrometry in the biological sciences: a tutorial*. 1992: Kluwer Academic Pub.
71. Watson, J.T. and O.D. Sparkman, *Introduction to mass spectrometry: instrumentation, applications, and strategies for data interpretation.* 2007.
72. Dawson, P.H., *Quadrupole mass spectrometry and its applications*. 1995: Springer.
73. Miller, P.E. and M.B. Denton, *The quadruple mass filter: Basic operating concepts.* Journal of Chemical Education, 1986. 63(7): p. 617.
74. Davis, R., M. Frearson, and F.E. Prichard, *Mass spectrometry: analytical chemistry by open learning*. 1987: John Wiley & Sons.
75. Fatsikostas, A.N., D.I. Kondarides, and X.E. Verykios, *Production of hydrogen for fuel cells by reformation of biomass-derived ethanol.* Catalysis Today, 2002. 75(1-4): p. 145-155.
76. MarinÌƒo, F., et al., *Hydrogen production from steam reforming of bioethanol using Cu/Ni/K-Al_2O_3 catalysts. Effect of Ni.* International Journal of Hydrogen Energy, 2001. 26(7): p. 665-668.

77. Klouz, V., et al., *Ethanol reforming for hydrogen production in a hybrid electric vehicle: Process optimisation.* Journal of Power Sources, 2002. 105(1): p. 26-34.
78. GarciÌ a, E.Y. and M.A. Laborde, *Hydrogen production by the steam reforming of ethanol: Thermodynamic analysis.* International Journal of Hydrogen Energy, 1991. 16(5): p. 307-312.
79. Vasudeva, K., et al., *Steam reforming of ethanol for hydrogen production: Thermodynamic analysis.* International Journal of Hydrogen Energy, 1996. 21(1): p. 13-18.
80. Fishtik, I., et al., *Thermodynamic analysis of hydrogen production by steam reforming of ethanol via response reactions.* International Journal of Hydrogen Energy, 2000. 25(1): p. 31-45.
81. Haga, F., et al., *Catalytic properties of supported cobalt catalysts for steam reforming of ethanol.* Catalysis Letters, 1997. 48(1-2): p. 223-227.
82. AupreÌ,tre, F., C. Descorme, and D. Duprez, *Bio-ethanol catalytic steam reforming over supported metal catalysts.* Catalysis Communications, 2002. 3(6): p. 263-267.
83. Srisiriwat, N., S. Therdthianwong, and A. Therdthianwong, *Oxidative steam reforming of ethanol over Ni/Al_2O_3 catalysts promoted by CeO_2, ZrO_2 and CeO_2-ZrO_2.* International Journal of Hydrogen Energy, 2009. 34(5): p. 2224-2234.
84. Cai, W., et al., *Hydrogen production from ethanol over Ir/CeO_2 catalysts: A comparative study of steam reforming, partial oxidation and oxidative steam reforming.* Journal of Catalysis, 2008. 257(1): p. 96-107.
85. Silva, A.M., et al., *Partial oxidation and water-gas shift reaction in an integrated system for hydrogen production from ethanol.* Applied Catalysis A: General, 2008. 334(1-2): p. 179-186.
86. Cavallaro, S., N. Mondello, and S. Freni, *Hydrogen produced from ethanol for internal reforming molten carbonate fuel cell.* Journal of Power Sources, 2001. 102(1-2): p. 198-204.
87. Fatsikostas, A.N. and D. Kondarides, *Production of hydrogen for fuel cells by reformation of biomass-derived ethanol.* Catalysis Today, 2002. 75(1-4): p. 145-155.
88. Huang, L., et al., *Iron-promoted nickel-based catalysts for hydrogen generation via auto-thermal reforming of ethanol.* Catalysis Communications, 2009. 10(5): p. 502-508.
89. Liguras, D.K., K. Goundani, and X.E. Verykios, *Production of hydrogen for fuel cells by catalytic partial oxidation of ethanol over structured Ru catalysts.* International Journal of Hydrogen Energy, 2004. 29(4): p. 419-427.
90. MikulovÃ¡, J., et al., *Wet air oxidation of acetic acid over platinum catalysts supported on cerium-based materials: Influence of metal and oxide crystallite size.* Journal of Catalysis, 2007. 251(1): p. 172-181.
91. Sadovskaya, E.M., et al., *Kinetics of oxygen exchange over CeO_2-ZrO_2 fluorite-based catalysts.* Journal of Physical Chemistry A, 2007. 111(20): p. 4498-4505.
92. Silva, A.M., et al., *Partial oxidation of ethanol on Ru/Y_2O_3 and Pd/Y_2O_3 catalysts for hydrogen production.* Catalysis Today, 2007. 129(3-4): p. 297-304.
93. Mattos, L.V. and F.B. Noronha, *Partial oxidation of ethanol on supported Pt catalysts.* Journal of Power Sources, 2005. 145(1): p. 10-15.

94. Santos, A.C.S.F., et al., *The effect of ceria content on the performance of $Pt/CeO_2/Al_2O_3$ catalysts in the partial oxidation of methane.* Applied Catalysis A: General, 2005. 290(1-2): p. 123-132.
95. Bi, J.L., et al., *Low-temperature mild partial oxidation of ethanol over supported platinum catalysts.* Catalysis Today, 2007. 129(3-4): p. 330-335.
96. Bolm, C., et al., *Iron-catalyzed reactions in organic synthesis.* Chem. Rev, 2004. 104(12): p. 6217-6254.
97. Legros, J., *Highly Enantioselective Iron-Catalyzed Sulfide Oxidation with Aqueous Hydrogen Peroxide under Simple Reaction Conditions.* Angewandte Chemie International Edition, 2004. 43(32): p. 4225.
98. Moens, B., et al., *Epoxidation of propylene with nitrous oxide on Rb_2SO_4-modified iron oxide on silica catalysts.* Journal of Catalysis, 2007. 247(1): p. 86-100.
99. Riedel, T., et al., *Fischer-Tropsch on iron with H_2/CO and H_2/CO_2 as synthesis gases: The episodes of formation of the Fischer-Tropsch regime and construction of the catalyst.* Topics in Catalysis, 2003. 26(1-4): p. 41-54.
100. Lu, A.H., E.L. Salabas, and F. Schüth, *Magnetic nanoparticles: synthesis, protection, functionalization, and application.* Angewandte Chemie International Edition, 2007. 46(8): p. 1222-1244.
101. Abu-Reziq, R., et al., *Metal supported on dendronized magnetic nanoparticles: highly selective hydroformylation catalysts.* J. Am. Chem. Soc, 2006. 128(15): p. 5279–5282.
102. Dálaigh, C., et al., *A Magnetic-Nanoparticle-Supported 4-N,N-Dialkyl-aminopyridine Catalyst: Excellent Reactivity Combined with Facile Catalyst Recovery and Recyclability.* Angewandte Chemie, 2007. 119(23): p. 4407-4410.
103. Chang, F.W., et al., *Hydrogen production by partial oxidation of methanol over gold catalysts supported on TiO_2-MO_x (M = Fe, Co, Zn) composite oxides.* Applied Catalysis A: General, 2006. 302(2): p. 157-167.
104. Chang, F.W., L.S. Roselin, and T.C. Ou, *Hydrogen production by partial oxidation of methanol over bimetallic Au-Ru/Fe_2O_3 catalysts.* Applied Catalysis A: General, 2008. 334(1-2): p. 147-155.
105. Pacchioni, G., *Quantum chemistry of oxide surfaces: From CO chemisorption to the identification of the structure and nature of point defects on MgO.* Surface Review and Letters, 2000. 7(3): p. 277-306.
106. Knight, W.D., et al., *Electronic shell structure and abundances of sodium clusters.* Physical Review Letters, 1984. 52(24): p. 2141-2143.
107. Kaldor A., et al.,, Advanced Chemical Physics, 1988. 70: p. 211.
108. Orthner, H.R. and P. Roth, *Formation of iron oxide powder in a hot-wall flow reactor:Effect of process conditions on powder characteristics.* Materials Chemistry and Physics, 2003. 78(2): p. 453-458.
109. Yoon, K.H. and J. Desmaison, *Carbon-excess silicon carbide deposition from pyrolysis of tetramethylsilane.* Surface and Coatings Technology, 1993. 56(3): p. 243-248.
110. Veintemillas, S., et al., *Thermodynamic analysis of metalorganic chemical vapour deposition of SiC using tetramethylsilane as precursor.Identification of the main reactions.* Journal of Crystal Growth, 1995. 148(4): p. 383-389.
111. NIST Chemistry Web Book, O.-D., http://webbook.nist.gov

112. Steele, W.V., *The standard molar enthalpies of formation of organosilicon compounds and related bond-dissociation enthalpies II. Tetramethylsilane.* The Journal of Chemical Thermodynamics, 1983. 15(6): p. 595-601.
113. Siddiqi, M.A. and B. Atakan, *Vapor- Liquid Equilibrium of Ferrocene in Some Organic Solvents Using Spectroscopic Methods.* J. Chem. Eng. Data, 2006. 51(3): p. 1092-1096.
114. Siddiqi, M.A. and B. Atakan, *Combined experiments to measure low sublimation pressures and diffusion coefficients of organometallic compounds.* Thermochimica Acta, 2007. 452(2): p. 128-134.
115. Duminica F., e.a., (EUROCVD-15, Sep. (5-9) 2005, Bochum, Germany), ECS Proceeding Vol. 2005-09,644-651, 2005. .
116. Pflitsch, C., et al., *Growth of thin iron oxide films on Si(100) by MOCVD.* Journal of the Electrochemical Society, 2006. 153(8): p. C546-C550.
117. Hsu, S.N., et al., *Low-temperature partial oxidation of ethanol over supported platinum catalysts for hydrogen production.* International Journal of Hydrogen Energy, 2008. 33(2): p. 693-699.
118. Pecora, R., *Dynamic light scattering measurement of nanometer particles in liquids.* Journal of Nanoparticle Research, 2000. 2(2): p. 123-131.
119. Xu, X., et al., *Sol-gel formation of [gamma]-Fe_2O_3/SiO_2 nanocomposites: Effects of different iron raw material.* Journal of Alloys and Compounds, 2009. 468(1-2): p. 414-420.
120. Scheffe, J.R., et al., *Atomic layer deposition of iron(III) oxide on zirconia nanoparticles in a fluidized bed reactor using ferrocene and oxygen.* Thin Solid Films, 2009. 517(6): p. 1874-1879.
121. Bogatyrev, V.M., et al., *Synthesis and characterization of Fe_2O_3/SiO_2 nanocomposites.* Journal of Colloid and Interface Science, 2009. 338(2): p. 376-388.
122. Noborio, M., J. Suda, and T. Kimoto, *4H-SiC MIS capacitors and MISFETs with deposited SiN_x/ SiO_2 stack-gate structures.* IEEE Transactions on Electron Devices, 2008. 55(8): p. 2054-2060.
123. Förster, J., M. Von Hoesslin, and J. Uhlenbusch, *Temperature measurements in CO_2-laser-induced pyrolysis flames for SiC and ternary SiC/C/B powder synthesis by means of CARS.* Applied Physics B: Lasers and Optics, 1996. 62(6): p. 609-612.
124. Li, Y., et al., *Laser synthesis of ultrafine Si_3N_4SiC powders from hexamethyldisilazane.* Materials Science and Engineering A, 1994. 174(2): p. L23-L26.
125. Beaber, A.R., et al., *Nanostructured SiC by chemical vapor deposition and nanoparticle impaction.* Surface and Coatings Technology, 2007. 202(4-7): p. 871-875.
126. Chu, Z.Y., et al., *A model SiC-based fiber with a low oxygen content prepared from a vinyl-containing polycarbosilane precursor.* Journal of Materials Science Letters, 2001. 20(7): p. 585-587.
127. Zaitseva, N., et al., *Effect of Nitrogen on the Stability of Silicon Nanocrystals Produced by Decomposition of Alkyl Silanes.* 2008.
128. Klein, S., M. Winterer, and H. Hahn, *Reduced-pressure chemical vapor synthesis of nanocrystalline silicon carbide powders.* Chemical Vapor Deposition, 1998. 4(4): p. 143-149.
129. Leroi, P., et al., *Ni/SiC: A stable and active catalyst for catalytic partial oxidation of methane.* Catalysis Today, 2004. 91-92: p. 53-58.

130. Kolar, F., et al., *Structural characterization and thermal oxidation resistance of silicon oxycarbides produced by polysiloxane pyrolysis.* Materials Chemistry and Physics, 2004. 86(1): p. 88-98.
131. Abe, K., et al., *Characterization of polycrystalline SiC films grown by HW-CVD using silicon tetrafluoride.* Thin Solid Films, 2008. 516(5): p. 637-640.
132. Wu, H. and a.D. Ready, *in Silicon Carbide Symposium, Ceramic Transactions 1987.* Am. Serm. Soc. Westerville, OH., 1989: p. 235. .
133. Okabe, Y., J. Hojo, and A. Kato, *formation of fine silicon carbide powders by a vapor phase method.* journal of less-commen metals, 1979. 68: p. 29-41.
134. Shi, Y., et al., *Decomposition of hexamethyldisilane on a hot tungsten filament and gas-phase reactions in a hot-wire chemical vapor deposition reactor.* Physical Chemistry Chemical Physics, 2008. 10(18): p. 2543-2551.
135. Smolik, J. and P. Moravec, *Gas phase synthesis of fine silica particles by oxidation of tetraethylorthosilicate vapour.* Journal of Materials Science Letters, 1995. 14(6): p. 387-389.
136. Schwertmann, U. and R.M. Cornell, *Iron oxides in the laboratory: preparation and characterization*. 2000: Vch Verlagsgesellschaft Mbh.
137. Li, S., et al., *Promoted iron-based catalysts for the Fischer-Tropsch synthesis: Design, synthesis, site densities, and catalytic properties.* Journal of Catalysis, 2002. 206(2): p. 202-217.
138. Li, T., et al., *Effect of manganese on an iron-based Fischer-Tropsch synthesis catalyst prepared from ferrous sulfate.* Fuel, 2007. 86(7-8): p. 921-928.
139. Litt, G. and C. Almquist, *An investigation of CuO/Fe2O3 catalysts for the gas-phase oxidation of ethanol.* Applied Catalysis B: Environmental, 2009. 90(1-2): p. 10-17.
140. Scheffe, J.R., et al., *Atomic layer deposition of iron(III) oxide on zirconia nanoparticles in a fluidized bed reactor using ferrocene and oxygen.* Thin Solid Films, 2009. 517(6): p. 1874-1879.
141. Chavez-Galan, J. and R. Almanza, *Solar filters based on iron oxides used as efficient windows for energy savings.* Solar Energy, 2007. 81(1): p. 13-19.
142. Glasscock, J.A., et al., *Structural, optical and electrical properties of undoped polycrystalline hematite thin films produced using filtered arc deposition.* Thin Solid Films, 2008. 516(8): p. 1716-1724.
143. Mauvernay, B., et al., *Elaboration and characterization of $Fe_{1-x}O$ thin films sputter deposited from magnetite target.* Thin Solid Films, 2007. 515(16 SPEC. ISS.): p. 6532-6536.
144. Meille, V., *Review on methods to deposit catalysts on structured surfaces.* Applied Catalysis A: General, 2006. 315: p. 1-17.
145. Milliken, J., et al., *The Advanced Energy Initiative.* Journal of Power Sources, 2007. 172(1): p. 121-131.
146. Momirlan, M. and T. Veziroglu, *Recent directions of world hydrogen production.* Renewable and Sustainable Energy Reviews, 1999. 3(2): p. 219-231.
147. Pasel, J., et al., *Transition metal oxides supported on active carbons as low temperature catalysts for the selective catalytic reduction (SCR) of NO with NH_3.* Applied Catalysis B: Environmental, 1998. 18(3-4): p. 199-213.
148. Alvarez-Merino, M.A., F. Carrasco-MariÌ n, and C. Moreno-Castilla, *Tungsten catalysts supported on activated carbon II. Skeletal isomerization of 1-butene.* Journal of Catalysis, 2000. 192(2): p. 374-380.

149. Scariot, M., et al., *An investigation of the activation process of high temperature shift catalyst.* Catalysis Today, 2008. 133-135(1-4): p. 174-180.
150. Kulkarni, D. and I.E. Wachs, *Isopropanol oxidation by pure metal oxide catalysts: Number of active surface sites and turnover frequencies.* Applied Catalysis A: General, 2002. 237(1-2): p. 121-137.
151. Nguyen, B.N.T. and C.A. Leclerc, *Metal oxides as combustion catalysts for a stratified, dual bed partial oxidation catalyst.* Journal of Power Sources, 2007. 163(2): p. 623-629.
152. Lide, D.R., *CRC handbook of chemistry and physics: a ready-reference book of chemical and physical data*. 2004: CRC Pr I Llc.
153. Chang, F.W., S.C. Lai, and L.S. Roselin, *Hydrogen production by partial oxidation of methanol over ZnO-promoted Au/Al_2O_3 catalysts.* Journal of Molecular Catalysis A: Chemical, 2008. 282(1-2): p. 129-135.
154. Mars, P. and D.W. Van Keevelen, *Oxidations carried out by means of vanadium oxide catalysts*. Proceedings, May 6th to 8th 1954, 1954: p. 41.
155. Luengnaruemitchai, A., S. Osuwan, and E. Gulari, *Comparative studies of low-temperature water-gas shift reaction over Pt/CeO_2, Au/CeO_2, and Au/Fe_2O_3 catalysts.* Catalysis Communications, 2003. 4(5): p. 215-221.
156. HorvÃ¡th, D., L. Toth, and L. Guczi, *Gold nanoparticles: Effect of treatment on structure and catalytic activity of Au/Fe_2O_3 catalyst prepared by co-precipitation.* Catalysis Letters, 2000. 67(2-4): p. 117-128.
157. Hutchings, G.J., et al., *Role of gold cations in the oxidation of carbon monoxide catalyzed by iron oxide-supported gold.* Journal of Catalysis, 2006. 242(1): p. 71-81.
158. Temesghen, W. and P.M.A. Sherwood, *Analytical utility of valence band X-ray photoelectron spectroscopy of iron and its oxides, with spectral interpretation by cluster and band structure calculations.* Analytical and Bioanalytical Chemistry, 2002. 373(7): p. 601-608.
159. Hawn, D.D. and B.M. DeKoven, *Deconvolution as a correction for photoelectron inelastic energy losses in the core level XPS spectra of iron oxides.* Surface and interface analysis, 2004. 10(2-3): p. 63-74.
160. Briggs, D. and M.P. Seah, *Practical surface analysis by Auger and X-ray photoelectron spectroscopy.* D. Briggs, & M. P. Seah,(Editors), John Wiley & Sons, Chichester 1983, xiv+ 533, 1983.
161. Bogatyrev, V.M., et al., *Synthesis and characterization of Fe_2O_3/SiO_2 nanocomposites.* Journal of Colloid and Interface Science, 2009. 338(2): p. 376-388.
162. Durrant, S.F., et al., *Characterization of Si:O:C:H films fabricated using electron emission enhanced chemical vapour deposition.* Thin Solid Films, 2008. 516(5): p. 803-806.
163. Yang, L., et al., *Formation of β-SiC nanowires by annealing SiC films in hydrogen atmosphere.* Physica E: Low-Dimensional Systems and Nanostructures, 2006. 35(1): p. 146-150.
164. Eck, J., et al., *Behavior of SiC at high temperature under helium with low oxygen partial pressure.* Journal of the European Ceramic Society, 2008. 28(15): p. 2995-3004.
165. Li, B., et al., *Simultaneous growth of SiC nanowires, SiC nanotubes, and SiC/SiO2 core-shell nanocables.* Journal of Alloys and Compounds, 2008. 462(1-2): p. 446-451.

166. Vedrine, J.C., G. Coudurier, and J.M.M. Millet, *Molecular design of active sites in partial oxidation reactions on metallic oxides.* Catalysis Today, 1997. 33(1-3): p. 3-13.

Lebenslauf

Wael Ahmed Abou Taleb Sayed Ahmed

Zur Person

Geburtsdatum, Ort:	26.03.1977, in Daqahlia, Ägypten
Nationalität:	Ägypter
Sozialstatus:	Verheiratet
Muttersprache:	Arabisch
Fremdsprachen:	Englisch (sehr gut in Wort und gut in Schrift)
	Deutsch (gut in Wort und Schrift)

Beruflicher Weg: (MM.JJ – MM.JJ)

11.06 – jetzt	**Doktorant:** Lehrstuhl für Thermodynamik, IVG, Universität Duisburg-Essen, Deutschland
06.00 – 11.06	**Assistant researcher:** Refining department, Egyptian Petroleum Research Institute, Kairo, Ägypten

Erfahrungen mit dem PC:

Microsoft Office: Sehr gut (Word, Excel, Power point, etc.).

ProEngineer: Gut

Hochschulen:

Nov 2006	**Doktorarbeit:** Lehrstuhl für Thermodynamik, IVG, Universität Duisburg-Essen, Deutschland
Jan 2005	**Master Grad:** Physikalische Chemie, Al-Azhar Universität, Kairo, Ägypten
Jun 1998	**Bachelor:** Chemie, Al-Azhar Universität, Kairo, Ägypten

Sprachkurse:

1- Drei Monate von April 06 bis Juni 06 im Zentrum für Deutsch in Kairo.

2- English course in America-Mideast Educational and Training Services (AMIDEAST) April 2006.